Sliding Mode Observer-Based Load Torque Identification for PMSM Drives

Jeppe Borregaard & Mathias G. Fredslund

Department of Energy
Aalborg University
Date 30/05 - 2022

Master Thesis

STUDENT REPORT
AALBORG UNIVERSITY

AALBORG UNIVERSITY
STUDENT REPORT

4th semester of Master Studies

Department of Energy
Pontoppidanstræde 111
9220 Aalborg
www.et.aau.dk/

Title:

Sliding Mode Observer-Based Load Torque Identification for PMSM Drives

Project:

Master's thesis - Spring, 2022

Project Period:

February 2022 - May 2022

Project Group:

MCE4 - 1027

Participants:

Mathias Gramstrup Fredslund
Jeppe Louis Hagsten Borregaard

Supervisor:

Kaiyuan Lu

Total Pages: 118
Blank Pages: 5
Appendix:8
Hand in date: 30th of May, 2022

Abstract:

This project concerns the speed control of a surface-mounted permanent magnet synchronous motor. The goal is to improve the speed response under a load torque by online estimating the load torque disturbance and then using feed-forward compensation to counteract the speed error, reducing recovery time and enabling the PI controllers to work more effectively. Field Oriented Control (FOC) is used to control the drive system, where PI controllers were designed to control the dq reference currents and the electric rotor speed.
The dynamical equations describing a SPMSM were used to construct a non-linear model to simulate the motor. Four different sliding mode observers (SMO) were designed to estimate the load torque. The FOC and SMOs were tested and tuned with the constructed simulation model. The designed SMOs and FOC were then implemented into the physical test setup, where experiments were conducted and analyzed.
From the test at 600 [RPM], it was concluded that the SMO using a saturation function (SMO-Sat) showed the best results regarding RMS errors and recovery time with the values of 1.5 [RPM] and 103 [ms], respectively. Without the load torque compensation, the drive system showed an RMSE of 7.3 [RPM] and a recovery time of 150 [ms], for the test at 1800 [RPM]. The SMO-Sat and a proposed SMO method utilizing the Power-Sigmoid function (SMO-PS) showed the best results. For SMO-Sat, the RMSE was 1.6 [RPM] with 90 [ms] recovery time and for SMO-PS an RMSE of 2 [RPM] and a recovery time of 83 [ms] for 5 [Nm] load at 1800 [RPM].

Summary

In recent years, many studies have been proposed to optimize the control of a PMSM with feed-forward load torque compensation to improve the overall performance, thereby eliminating the undesirable sudden speed change occurring when applying a load torque to the drive system. Therefore, this study aims to control an SPMSM, where the main objective is to obtain fast speed control through load torque compensation. Various methods of estimating load torque have been proposed over the years. Therefore, this study further aims to analyze and compare different sliding mode observer-based methods to estimate the load torque using simulation and experimental results conducted on a physical test setup.

To analyze the performance of the drive system with the designed SMOs, a non-linear mathematical model is made in Simulink to simulate the motor. The non-linear model is constructed based on the dynamical equations described by SPMSM.

Field Oriented Control (FOC) is used to control the drive system. The FOC utilizes a cascade structure with an inner current loop and an outer speed loop. The FOC structure uses PI controllers to control the dq reference currents and the electric rotor speed. The PI current controller is designed based on the linear current system, where the back-EMF terms are decoupled based on a Relative Gain Array (RGA) analysis, which showed a strong coupling effect for high-speed operations. The PI speed controller is designed based on the linear speed system where the load torque is considered a disturbance, leaving the drive system to work well under no-load conditions. However, as previously described, when applying a load torque to the PMSM, an undesirable transient occurs, leaving the overall motor performance will degrade.

Four different sliding mode observers are designed to compensate for the load torque disturbance. First, each method will be mathematically derived to present the principles of the observer structure. Afterward, a stability analysis is carried out for each SMOs, where a Lyapunov candidate function is used to prove stability by having its derivative be Negative Definite. Next, the SMOs are analyzed based on the constructed simulation model, where also the observer gains and parameters are analysed through various tests to understand their impact before determining the SMO parameters. Finally, when each SMOs has obtained good estimation results, the SMOs are implemented into the physical test setup.

The SMOs are tested for low and high speeds at 600 [RPM] and 1800 [RPM] respectively. In addition, a load torque of 1 [Nm] and 5 [Nm] is applied during each test. Lastly, the SMOs are compared based on the experimental performance, where peak-to-peak, recovery time, chatter level, RSME of speed error and RMSE of load torque estimation error is used to aid the comparison before concluding the study.

Preface

The following Master's thesis has been written by the 4th semester Mechatronic Control Engineering group MCE4-1027. Supervised by Kaiyuan Lu.

The software used in the report includes: MATLAB, Simulink, Inkscape and the websites Overleaf.com and Diagrams.net. Furthermore dSPACE is used for controlling the DSP in the experimental setup.

This report uses numbered citations and the references are presented in the end of the report.

Jeppe Borregaard

Mathias G. Fredslund

By accepting the request from the group member who uploads the study group's project report in Digital Exam System, you confirm that all group members have participated in the project work, and thereby all members are collectively liable for contents of the report. Furthermore, all group members confirm that the report does not include plagiarism.

Nomenclature

Symbols		Units
α	Observer Gain for LTID-SMO-PS	[-]
Δ	Observer Gain for LTID-SMO-Sat	[-]
δ	Observer Gain for LTID-SMO-PS	[-]
$\hat{\omega}_e$	Estimated Electrical Speed	[Rad/s]
$\hat{T}_L$	Load Torque Estimation	[Nm]
λ	Stator Flux	[Wb]
λ_{mpm}	Permanent Magnet Flux Linkage	[Wb]
$\omega^*_{r,mech}$	Mechanical Reference Speed	[Rad/s]
ω_e	Electric Rotor Speed	[Rad/s]
$\omega_{r,mech}$	Mechanical Speed	[Rad/s]
ϕ	Delay Between Estimated and Real Load Torque	[Rad]
σ	Sliding Variable	[RPM]
τ	Time Constant for Plant	[s]
τ_{inner}	Time Constant for Inner Loop Approximation	[s]
θ_r	Electric Rotor Angle	[Rad]
$\tilde{\omega}_e$	Electrical Speed Error	[Rad/s]
ζ	Damping Coefficient	[-]
e	back-EMF	[V]
e_{T_L}	Estimated Load Torque Error	[Nm]
f_s	Sampling Frequency	[Hz]
$G(s)$	Transfer Function	[-]
i_d	Direct axis Current	[A]
i_q	Quadrature axis Current	[A]

J	Total Moment of Inertia of the system	[Kg m^2]
k_f	Safety factor for LTID-SMO-Sat	[-]
K_T	Motor Torque Constant	[Nm / A]
K_i	Integral gain	[-]
K_p	Proportional gain	[-]
L	Inductance	[H]
n_{lab}	Measured Speed for laboratory	[RPM]
n_{meas}	Measured Speed for Experiments	[RPM]
N_{pp}	Number of Pole-Pairs	-
n_{rat}	Rated Speed	[RPM]
n_{sim}	Measured Speed for Simulation	[RPM]
p	Pole	[-]
R_s	Stator Resistance	[Ω]
T_d	Time Delay	[s]
T_e	Electric Torque	[Nm]
T_L	Load Torque	[Nm]
T_s	Sampling Time	[s]
T_{delay}	Time Delay	[s]
$T_{L,max}$	Maximum Load Torque	[Nm]
$T_{L,transient}$	Load Torque During Transient Response	[Nm]
T_{rated}	Rated Torque	[Nm]
T_{RT}	Recovery Time	[s]
$T_{settling,c}$	Settling Time for Inner Current Loop	[s]
$T_{settling,s}$	Settling Time for Outer Speed Loop	[s]
V	Lyapunov Candidate	[-]
v_i	Voltage	[V]
V_s	RMS Voltage	[V]
z_{PI}	Zero From PI Controller	[rad/s]

ω_c	Cutoff frequency on LPF	[Rad/s]
ω_{rat}	Rated speed	[Rad/s]
B	Viscous Friction	[Nm s/rad]
C	Coulomb Friction	[N]
K	Sliding Mode Gain	[-]
L	Observer Gain for LTID-SMO-Sat	[-]
s	Laplace operator	[-]

Abbreviations

EMF	Electro-Motive Force
FFT	Fast Fourier Transform
FOC	Field Oriented Control
LPF	Low-Pass Filter
LTID-SMO	Load Torque Identification Sliding Mode Observer
ND	Negative Definite
NSD	Negative Semi Definite
PD	Positive Definite
PI	Proportional Integral controller
PLL	Phase-Locked Loop
PMSM	Permanent Magnet Synchronous Motor
PS	Power-Sigmoid
RGA	Relative Gain Array
RMSE	Root Mean Square Error
RPM	Rounds Per Minute
SMO	Sliding Mode Observer
SPMSM	Surface-mounted Permanent Magnet Synchronous Motor
SVM	Space Vector Modulation
VSI	Voltage Source Inverter

Contents

1 Introduction

Permanent Magnet Synchronous Machine (PMSM) is becoming more widely used in various industrial applications due to nature of the PMSM as it has high efficiency, high power density, fast dynamical response, and high reliability [1]. In recent years, the PMSM has been used to replace the high-power asynchronous machine, since the PMSM offers 2-3 times more power density [2], making it a more attractive choice for many industrial applications, for example, the automobile industry or robot-based industries. Many studies have been proposed to optimize the PMSM performance in various aspects in the past decades. In [3] the authors describe how to optimize the PMSM using sliding mode observers to eliminate the use of sensors by online estimating the rotor position- and speed. In [4] the authors propose a method to optimize the PMSM by estimating the moment of inertia by the use of an improved model-reference adaptive system (IMRAS). Both these studies show that any optimization study has great importance for the technological developments of PMSM drives. Therefore, this thesis will focus on developing a method to online estimate the load torque. The load torque is often an unknown factor in the drive system, and an undesirable transient will occur in the speed response causing the overall system performance to degrade. Furthermore, for robot-based industries which specialises in designing robot arms for storage facilities, the load torque often changes due to the movements of different elements. Therefore, it is highly desirable to estimate the load torque, which can then be used in feed-forward current compensation by converting the estimated torque into an estimated current.

The topic of load torque identification (LTID) has been widely discussed in various papers. In [5] and [6] a Luenberger observer and a Kalman filter are proposed to estimate the load torque. However, sliding mode observers often plays a more significant part in developing load torque estimation methods due to its robustness against parameter variations, uncertainties, and disturbance rejection[1]. In [7] a conventional SMO uses a sign function as the switching term. This causes issues regarding chattering/buffering in the system and therefore heavy Low-pass filtering is needed [7]. LPF are known to cause undesirable phase delay, therefore, some proposed methods have been discussed in recent years to overcome the chattering issue instead by replacing the sign function with other functions as the switching term. In [1] an improved LTID-SMO is proposed using Saturation function where some parts of the signal is filtered through an LPF while the rest is directly feed back. The benefit of this method is as concluded in the paper both fast estimation and low chatter in steady-state [1]. In [8] the authors investigate the possibility of using a Sigmoid function as the switching term, which has the advantages of effectively reducing chatter and obtaining less phase delay as the need for an LPF is not required.

Therefore, this study proposes a new SMO method that utilizes a modified version of the Sigmoid function to reduce chattering even further and obtain good estimation results. This method will, throughout the project, be referred to as the *Power-Sigmoid method*.

The project analyzes and compares four different load torque identification (LTID) SMO methods. The first method is the conventional sliding mode observer using a sign function. The second is the boundary layer method, which uses a saturation function as the switching term. The third is the Power-Sigmoid method. The final method, is the Power-Sigmoid method combined with a PI controller.

When analyzing the three LTID-SMO methods, a simulation model is created based on the provided experimental setup described in the next section.

1.1 System Description

To compare the performance of the designed controllers and SMO's during the project, a physical test-setup is provided. The provided test-setup can be described by two main parts, the drive system and the load system. Both systems uses a surface-mounted permanent magnet synchronous machine (SPMSM) and is connected with a mechanical coupling between them. The drive and load system can be seen in Figure 1.1, where the load-SPMSM are solely used to generates a load torque to the other SPMSM.

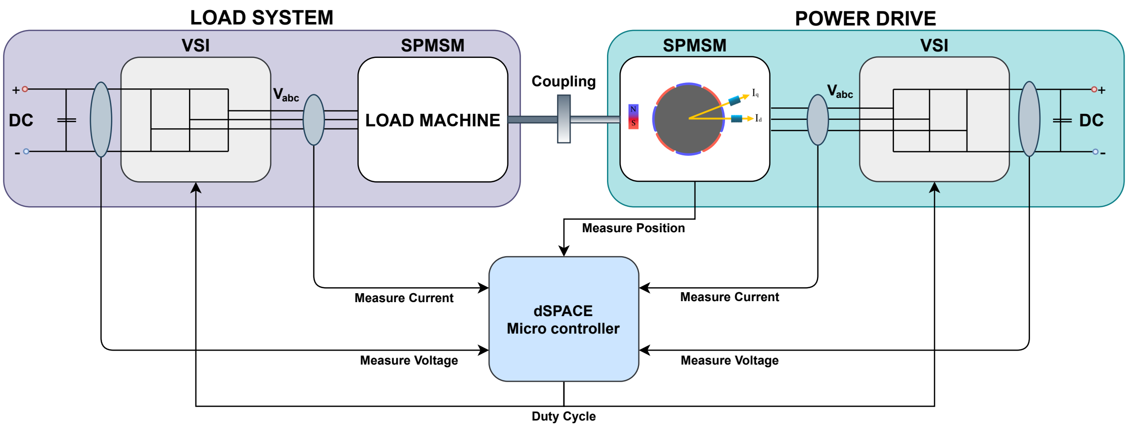

Figure 1.1. Schematic of the experimental test setup.

Two DC sources are used to supply the voltage source inverter (VSI) used for both SPMSM's. The VSI is controlled by a duty cycle calculated by space vector modulation (SVM) in dSPACE. dSPACE is a micro controller, with a software program that utilizes the MATLAB program Simulink. In addition, the test-setup uses different sensor to measure the system states. The sensors used are current sensors for measuring the 3-phase *abc* currents in the drive system, voltage sensors for measuring the voltage signals across the VSI and lastly an encoder to measure the rotor position and speed.

Problem Statement 2

This study aims to control a SPMSM, where the main objective is to obtain a precise and fast control through load torque compensation. As described in the introduction, various methods of estimating a load torque have been proposed over the years. Therefore, the purpose of this study is to analyze and compare different sliding mode observer-based methods to estimate the load torque using simulation and experimental results conducted for each methods, which leads up to the following problem statement:

"How can sliding mode observer-based load torque identification methods be designed to estimate a load torque to improve the speed control of a PMSM?"

2.1 Objectives

To answer the problem statement, the following objectives are formulated as:

1. Construct a non-linear model described by the dynamical differential equations of the SPMSM.
2. To control the speed and current in the drive system, field oriented control (FOC) is designed, having a cascade control structure with an inner current loop and outer speed loop.
3. Validate the non-linear model with experimental test.
4. Describe the load torque dynamic given from the load machine and construct a mathematical approach to obtain the actual load torque.
5. Describe and analyze methods for estimating the load torque disturbance using sliding mode control theory.
6. Compare the results of the different sliding mode observer-based load torque identification methods.

2.2 Project Limitations

To limit the scope of this project, some assumptions is made throughout the project, defined as:

- The PMSM is symmetric and balanced and the zero component in the *dq* reference frame is neglected.

- The magnetic flux in the PMSM is constant, and thereby will not reach its saturation limits.
- The air gap between the rotor and stator is uniformly distributed and the q and d axis inductance's is equal.
- Eddy losses and hysteresis losses are neglected.
- The motor parameters will not change due to increased temperatures.
- The VSI is assumed ideal and will not take part of the modeling.

2.3 Performance Evaluation of the Sliding Mode Observers

As described in the problem statement, the goal is to improve the speed control of the PMSM using LTID-SMO. Therefore, to improve the speed control the settling/recovery time and overshoot for the speed response must be improved when running the drive system with the designed LTID-SMO. The recovery time throughout the project is determined as:

For 600 [RPM]:

- The recovery time, T_{RT}, is determined within ± 1 [RPM].

For 1800 [RPM]:

- The recovery time is determined within ± 3 [RPM].

The overshoot in the speed response are for this project presented with its peak-to-peak value, calculated as: peak-to-peak $= \max(speed) - \min(speed)$.

PMSM Modeling 3

The described system from Section 1.1 is to be modeled. This is the foundation for the simulation and making of the control structure. In this chapter, the motor parameters are presented, the motor voltage equation in the dq reference frame and the mechanical equation of motion are described.

3.1 SPMSM Model Equations

The motor used is a Surface-mounted Permanent Magnet Synchronous Machine (SPMSM). Having the magnets mounted on the surface makes the motor non-salient due to the uniform reluctance, where the Permanent Magnets can be seen as an air gap due to the low permeability of the magnet being close to that of air [9]. The inductance in all directions is, therefore, the same [10], leaving that:

$$L_d = L_q \tag{3.1}$$

The parameters for the drive system are presented in Table 3.2, which will be used in the non-linear model.

Symbol	Description	Value	Unit
B	Viscous friction coefficient	$1.6655\,10^{-3}$	$[\frac{\mathrm{Nm\,s}}{\mathrm{rad}}]$
C	Coulomb friction	0.42	[Nm]
J	Total inertia	0.0125	$[\mathrm{kg\,m^2}]$
L_d	Inductance direct axis	$5.5\,10^{-3}$	[H]
L_q	Inductance quadrature axis	$5.5\,10^{-3}$	[H]
N_{pp}	Pole Pairs	4	[-]
n_{rat}	Rated speed	4500	[RPM]
R_s	Stator resistance	1.2	[Ω]
T_{rated}	Rated torque	5.8	[Nm]
V	Rated voltage	400	[V]
λ_{mpm}	Permanent magnet flux linkage	0.1213	[Wb]

Table 3.2. Parameters used to model the drive system.

The SPMSM is shown in Figure 3.1, where the stator is presented with the winding on the q and d axis space vectors.

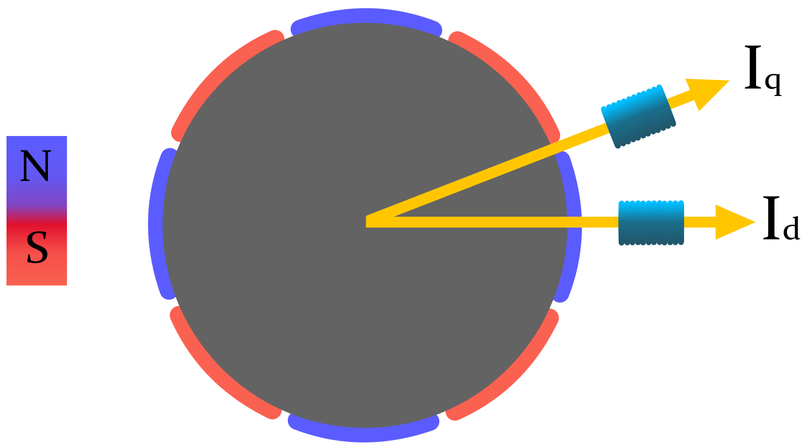

Figure 3.1. The surface-mounted permanent magnet synchronous machine, with the stator represented by the winding in the q and d space vectors.

The SPMSM is a 3-phase AC motor having eight poles. As seen in picture 3.1, each phase is shifted 120 electrical degrees from each other therefore applying a sinusoidal current to the windings will produce a rotating magnetic field. The equation describing the sinusoidal currents applied can be seen in 3.2 to 3.4. As the input to these three phases is sinusoidal, controlling them can be problematic as the phase is not constant [10]. Making vector projection can convert the stationary reference frame to a rotating dq reference frame that will follow the resultant space vector created. The dq reference frame is not fixed to the mechanical structure but rotates, as it sees the space vector as a signal with a constant phase. This allows for easier control as it becomes a DC signal from the perspective of the dq frame, and classical control theory can be used, such as PI controllers. Park-Clarke matrix transformation can be used to make the vector projection from the stationary abc frame to the rotating dq frame [9]. This can be seen in Equation 3.5.

$$i_a = I_m cos(\omega t) \tag{3.2}$$

$$i_b = I_m cos(\omega t - 120°) \tag{3.3}$$

$$i_c = I_m cos(\omega t + 120°) \tag{3.4}$$

$$\vec{f}_{dq0} = \frac{2}{3} \begin{bmatrix} \cos(\theta) & \cos\left(\theta - \frac{2}{3}\pi\right) & \cos\left(\theta + \frac{2}{3}\pi\right) \\ -\sin(\theta) & -\sin\left(\theta - \frac{2}{3}\pi\right) & -\sin\left(\theta + \frac{2}{3}\pi\right) \\ \frac{1}{2} & \frac{1}{2} & \frac{1}{2} \end{bmatrix} \cdot \vec{f}_{abc} \tag{3.5}$$

Stator voltage equations

After the Park-Clarke transformation, the stator voltage equations in the dq reference frame is described by Equations 3.6 and 3.7 with the zero component $v_0 = 0$.

$$v_d = R_s i_d + \frac{d}{dt}\lambda_d - \omega_e \lambda_q \tag{3.6}$$

$$v_q = R_s i_q + \frac{d}{dt}\lambda_q + \omega_e \lambda_d \tag{3.7}$$

where flux linkage λ_d and λ_q can be written as:

$$\lambda_d = L_d i_d + \lambda_{mpm} \tag{3.8}$$

$$\lambda_q = L_q i_q \tag{3.9}$$

As the q-axis is perpendicular to the magnets and only the flux linking the stator and rotor is affecting λ_q and as d-axis is parallel to the magnets, λ_d is affected both by flux linking stator to rotor and the flux produced by the magnets.

Combining Equation 3.6 and 3.7 with 3.8 and 3.9 yields:

$$v_d = R_s i_d + \frac{d}{dt}(L_d i_d + \lambda_{mpm}) - \omega_e L_q i_q \tag{3.10}$$

$$v_q = R_s i_q + \frac{d}{dt}L_q i_q + \omega_e(L_d i_d + \lambda_{mpm}) \tag{3.11}$$

Mechanical equation

The equation of motion is described using Newton's 2nd law:

$$\frac{d}{dt}(\omega_r)J = T_e - T_L - B\omega_r \tag{3.12}$$

J is the motors total inertia, ω_r is the speed of the rotor, T_e is the electric torque produced by the motor, B is the viscous friction and T_L is the load torque applied from the load machine.

The electric torque produced, T_e, can be derived as [10]:

$$T_e = \frac{3}{2}N_{pp}(\lambda_d i_q - \lambda_q i_d) \tag{3.13}$$

If substituting Equation 3.8 and 3.9 into Equation 3.13, the following is obtained:

$$T_e = \frac{3}{2}N_{pp}(\lambda_{mpm} i_q + (L_d - L_q) i_q i_d) \tag{3.14}$$

As previously mentioned in Equation 3.1 the inductance for L_d and L_q are equal for a SPMSM, leaving the torque equation can be simplified to:

$$T_e = \frac{3}{2} N_{pp} \lambda_{mpm} i_q \tag{3.15}$$

The torque is therefore proportional to the current i_q and the term $\frac{3}{2} N_{pp} \lambda_{mpm}$ is defined as the torque constant K_T.

3.2 Load Torque Dynamic

As the load torque step does not occur instantaneously and is associated with some amount of transient dynamic from the load machine, the actual load torque from lab is implemented into the Simulink model instead of an ideal load step. Thereby, a more representative simulation model of the physical system is made, ensuring that the simulation model considers all load torque dynamics. As a result, this will give a much more precise indication of how the physical system behaves when analyzing the Sliding Mode Observers in Chapter 5.

As the applied load torque can not be measured directly, the load torque is calculated using Equation 3.12 and 3.14 and repeated here:

$$T_L = T_e - B\omega_r - J\dot{\omega}_r \quad where \quad T_e = \frac{3}{2} N_{pp} \lambda_{mpm} i_q \tag{3.16}$$

To calculate the load torque, the mechanical rotor speed and the three-phase *abc* currents are measured, where the *abc* currents are transformed into its corresponding quadrature current, i_q. The measured speed and quadrature current are implemented into the Simulink model, where the calculation is made. To determine the angular acceleration of the rotor, a phase-locked loop (PLL) is used to acquire the acceleration. Utilizing a PLL also can suppress the high frequencies in the speed measurements [11], which means the unfiltered speed measurement can be used in the calculation of load torque, resulting in less phase lag. In Figure 3.2 a block diagram is made to illustrate the process of calculating the load torque with the proposed PLL structure.

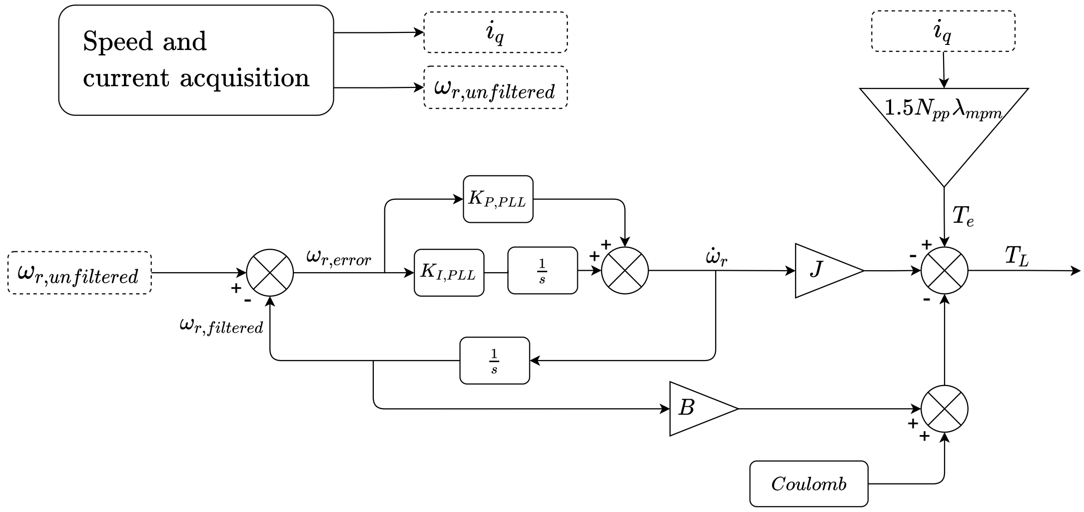

Figure 3.2. A block diagram of the load torque acquisition given from the load machine with a PLL structure.

From the above block diagram, the PI gains in the PLL have been tuned iteratively to obtain satisfactory results for the speed measurements. In addition, the Coulomb friction has been added to eliminate the static offset in the load torque.

Further, to describe the dynamical response of the load torque, a linear approximation is be made by determining the transfer function of the load torque. To estimate the transfer function, a test is conducted by applying a load step of $T_L = 5\,[\mathrm{Nm}]$ to the SPMSM with the motor is running at a constant reference speed of $n_{ref} = 1200\,[\mathrm{RPM}]$. The measured rotor speed and i_q current are implemented into the Simulink model to obtain the load torque. The results are presented in Figure 3.3.

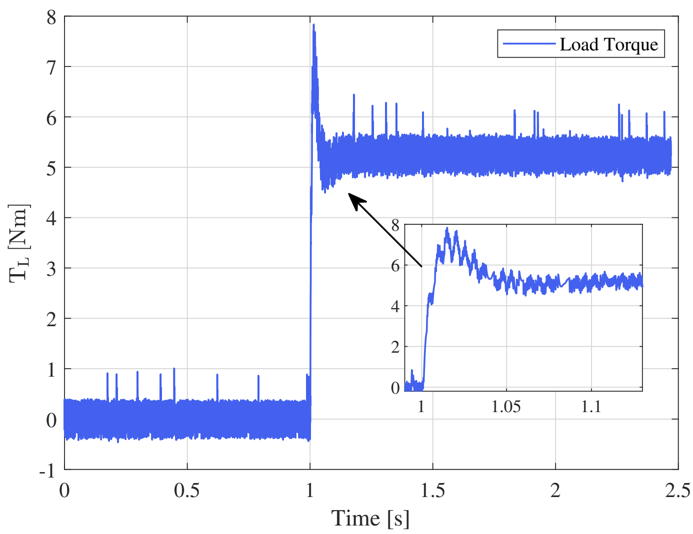

Figure 3.3. The simulation results for the load torque of $5\,[\mathrm{Nm}]$.

By analyzing the dynamical response of Figure 3.3, it is seen that the load torque resembles a second-order system due to the increased overshoot, entailing the system is underdamped and has complex poles. The linear approximation is made with the MATLAB program *System Identification* [12], by inputting the above-described information and the simulation results, given from Figure 3.3, the transfer function is determined to be:

$$G_{load}(s) = \frac{135.8s + 9813}{s^2 + 109s + 9743} \tag{3.17}$$

Finally, a comparison of the actual load torque and the linear approximation is made and seen in Figure 3.4. This approximation is also valid for different loads and speeds.

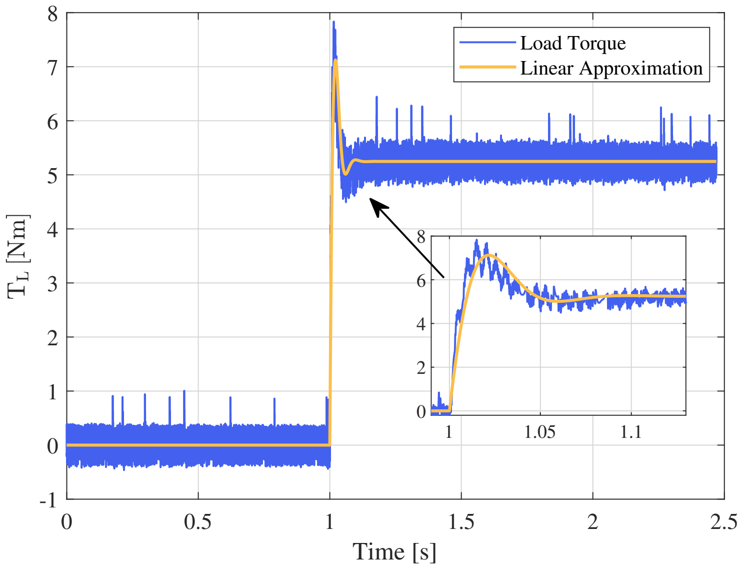

Figure 3.4. The simulation results for the load torque of 5 [Nm] with its corresponding linear approximation obtained through the MATLAB program *System Identification*.

Control of the SPMSM 4

This chapter presents the control strategy of the SPMSM utilized with Field Oriented Control, where an inner current loop and an outer speed loop are designed. PI controllers are designed to control the d and q axis currents separately for the inner current loop. Afterward, a PI speed controller is designed to control the electric rotor speed. Finally, the non-linear model is validated with the designed PI controllers.

4.1 Field Oriented Control

The control structure of the SPMSM is given by the Field Oriented Control (FOC). The FOC is a widely used vector control technique that utilizes the rotating dq frame by applying Clark/Park transformations which synchronously rotates with rotor. The FOC structure is a method used to control the electric torque and flux linkage by transforming the abc currents into their corresponding dq current components. The dq components make up the stator field vector, where the d-axis is aligned with the rotor flux axis. Maximum torque occurs when the stator field vector is shifted 90° electrical from the rotor flux axis. Therefore, by regulating the amplitude of the d-axis current vector to zero ($i_d = 0$), the entire stator field vector will be aligned with the q-axis current vector ($i_s = i_q$) and maximum torque is obtained. This is further seen in Figure 4.1, where it may also be noted the rotor position ($\theta_{r,el}$) is needed to perform the coordinate transformation from the stationary abc frame to the rotating dq frame.

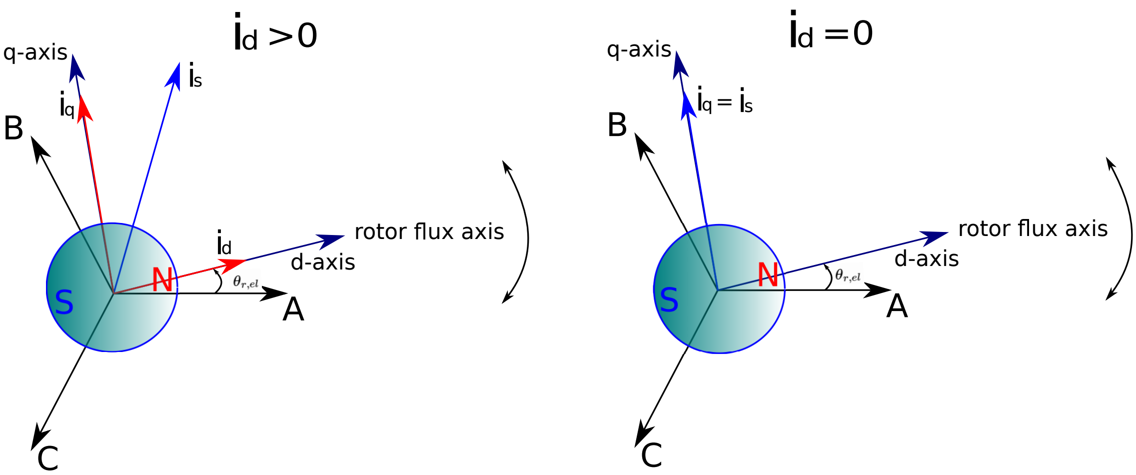

Figure 4.1. The stator field vector is decomposed into its d and q components. In addition two illustrations is shown, one for $i_d > 0$ and one for $i_d = 0$.

The FOC structure of the PMSM is presented with Figure 4.2. The FOC control scheme is based on a cascade structure with a speed controller placed in the outer loop and two current controllers in the inner loop. The speed and current loop are utilized by applying PI controllers to control the desired torque and flux. In addition, for the cascade structure to be successfully, the inner loop has to be faster than the outer loop, which should be taking into consideration when designing the PI controllers.

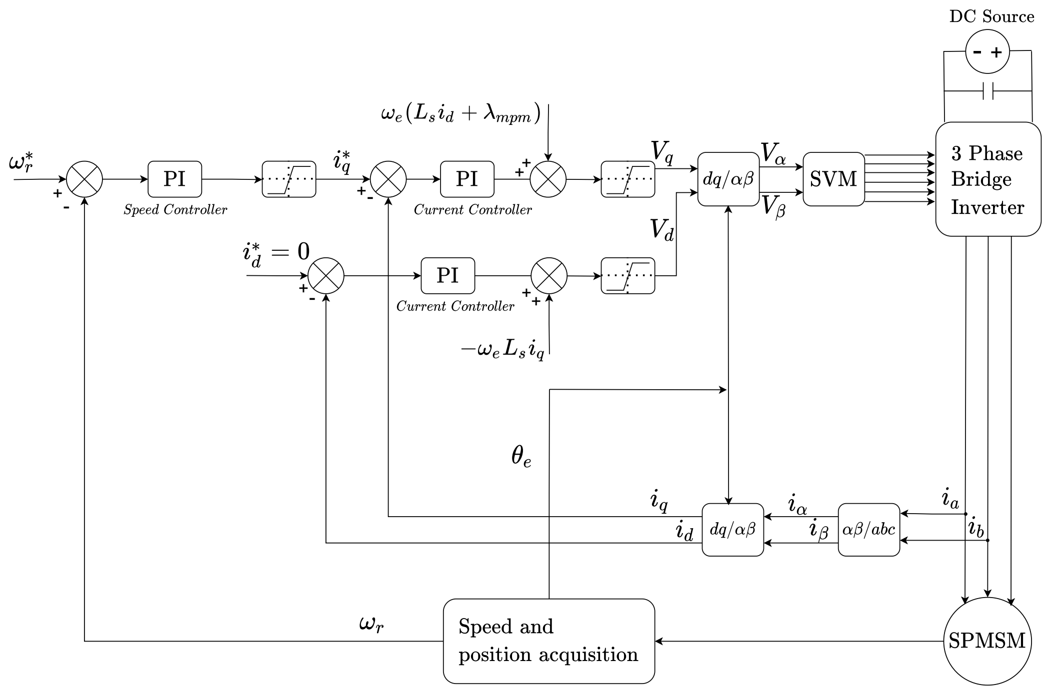

Figure 4.2. Schematic of the Field Oriented Control structure.

As illustrated in the above figure, the PI speed controller outputs the reference current, i_q^* based on the speed error $(\omega_r^* - \omega_r)$. Therefore, the input for the PI current controllers are given as $(i_q^* - i_q)$ and $(i_d^* - i_d)$, which then outputs the desired voltage for the VSI. In total, three PI controllers are needed in the FOC, where the coefficients (K_P and K_I) for the PI controllers will be derived based on classical control theory. However, to design the PI controllers, it is evident that the transfer function for the current and speed plants is derived.

4.1.1 Design of Current Control

An overview of the inner current loop containing the current plant, time delay, PI controller, and decoupling of the back-EMF terms is displayed in a block diagram of the linear system in Figure 4.3.

The coupling effect of the back-EMF terms is investigated with an RGA analysis in Appendix A, where it was found that the system is fully decoupled at $\omega_e = 0$. However, as the speed increases, the coupling effect becomes stronger. As aforementioned, the d and q axis are controlled separately, where a strong coupling effect may cause the overall dynamical performance of the PMSM to degrade [13]. Therefore, to overcome this issue, the back-EMF terms are decoupled with the method shown in Figure 4.3.

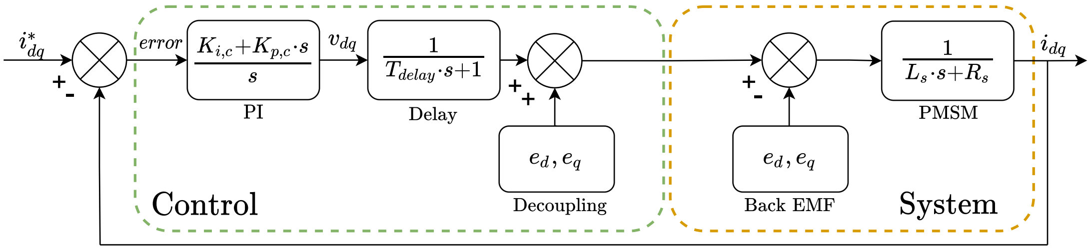

Figure 4.3. Block diagram of current loop.

When deriving the transfer function of the linear model for the two current plants, Equation 3.10 and 3.11 is rearranged and brought to the s-domain by applying a Laplace transformation. In addition, the transfer function is derived according to the current plant's output/input relationship.

$$i_d = \frac{v_d + e_d}{L_d s + R_s} \tag{4.1}$$

$$i_q = \frac{v_q + e_q}{L_q s + R_s} \tag{4.2}$$

Where the back-EMF terms are given as:

$$e_d = -\omega_e L_q i_q \quad and \quad e_q = \omega_e (L_d i_d + \lambda_{mpm}) \tag{4.3}$$

As seen in Equation 4.1 and 4.2, two inputs is shown, namely the voltage and back-EMF and one output given as the current. However, with the decoupling of two back-EMF terms the two current transfer functions is defined as:

$$G_d(s) = \frac{i_d}{v_d} = \frac{1}{L_d s + R_s} \tag{4.4}$$

$$G_q(s) = \frac{i_q}{v_q} = \frac{1}{L_q s + R_s} \tag{4.5}$$

Further, as the dealing with a surface-mounted PMSM, the inductance is the same in all directions ($L_q = L_d = L_s$). Therefore the two current plants for the d and q-axis currents are further reduced to a single plant given by Equation 4.6 enabling the control engineer to design only one PI controller to control both the d and q-axis currents.

$$G_{dq}(s) = \frac{1}{L_s s + R_s} \tag{4.6}$$

Time delay

When implementing the controllers into the experimental setup, time delays will occur. As the system is running on a digital platform, the sensor measurements for the rotor position, current, and voltage measurements will not be updated instantaneously and will imply adding a phase to the system and potentially make the system unstable. Therefore this has to be accounted for when designing controllers. The time delay is implemented into the control system and is inserted between the PI controllers and the current plant, and is estimated as a first-order transfer function given as:

$$G_{delay}(s) = \frac{1}{T_{delay}s + 1} \quad , \quad T_s = \frac{1}{f_s} \tag{4.7}$$

Here the time constant is defined as $T_{delay} = 1.5T_s$ and the sampling time T_s is calculated with the sampling frequency of $f_s = 5000\,\text{Hz}$.

Design of PI current controller

When designing the PI controller, a fast response and a low overshoot is preferred, as the inner current loop must be faster than the outer speed loop. The standard PI controller may be formulated as:

$$G_{PI} = \frac{K_{i,c} + K_{p,c}s}{s} \quad \textit{with the zero placed at} \quad z_{PI} = \frac{K_{i,c}}{K_{p,c}} \tag{4.8}$$

The PI controller consist of a pole placed at the origin given from the free integrator and a zero placed on the real axis. Having integrator action results in no steady-state error from a step input, whereas the placement of the zero contribute to how much overshoot, settling time, rise time etc. the control system experience [14]. Therefore, when tuning the PI controller, the placement of the zero will be investigated.

$$p_{current\,plant} = -\frac{R_s}{L_s} = -218 \quad \textit{and} \quad p_{time\,delay} = -\frac{1}{T_{delay}} = -3333 \tag{4.9}$$

If placing the zero from the PI controller to the left of the system pole from the current transfer function, faster dynamical response can be obtained. This is due to the closed-loop poles becoming complex-conjugated, which will lessen the damping in the system and thereby making the system transient faster. In addition, the zero should have a large enough safety margin from the system pole, such that the control system does not change any significantly dynamic if the system pole should increase and shift further into the LHP, due to parameter variations.

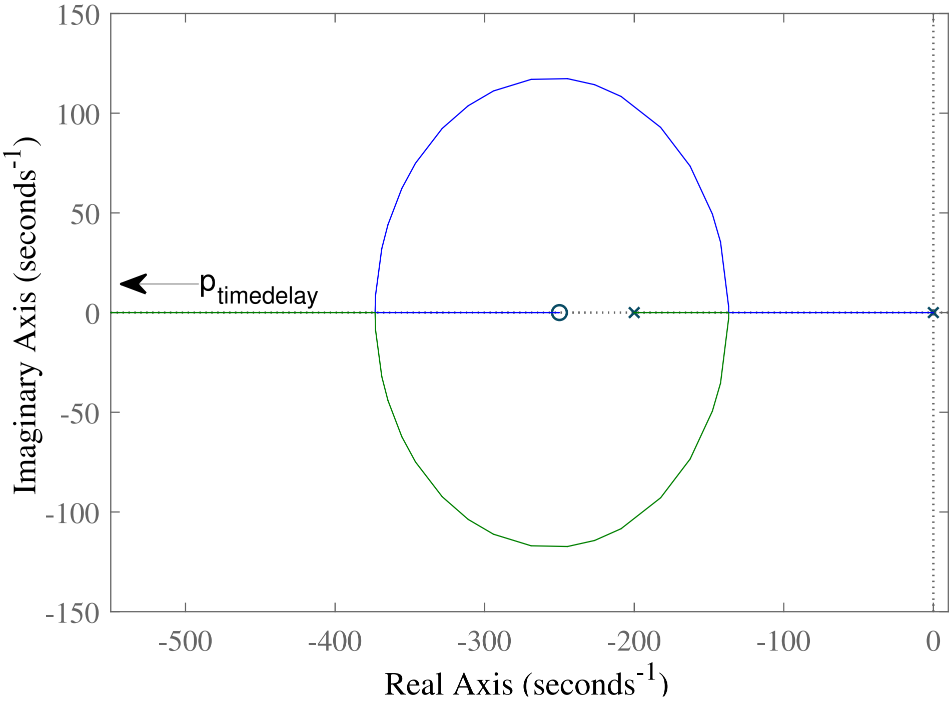

Figure 4.4. Root locus of the current loop

To ensure a fast dynamical response and minimize the overshoot, the placement of the zero is chosen to be at $z_{PI} = -250$ ensuring the prescribed requirements are obtained. This is further illustrated in Figure 4.4, where the PI controller has been implemented to the current loop. From the figure it is seen that the zero is placed to the left of current plant pole. Thereby, obtaining the desired transient response.

From the above analysis the closed-loop step response is presented in Figure 4.5, where the final results for the PI gains and settling time are displayed in Table below the figure.

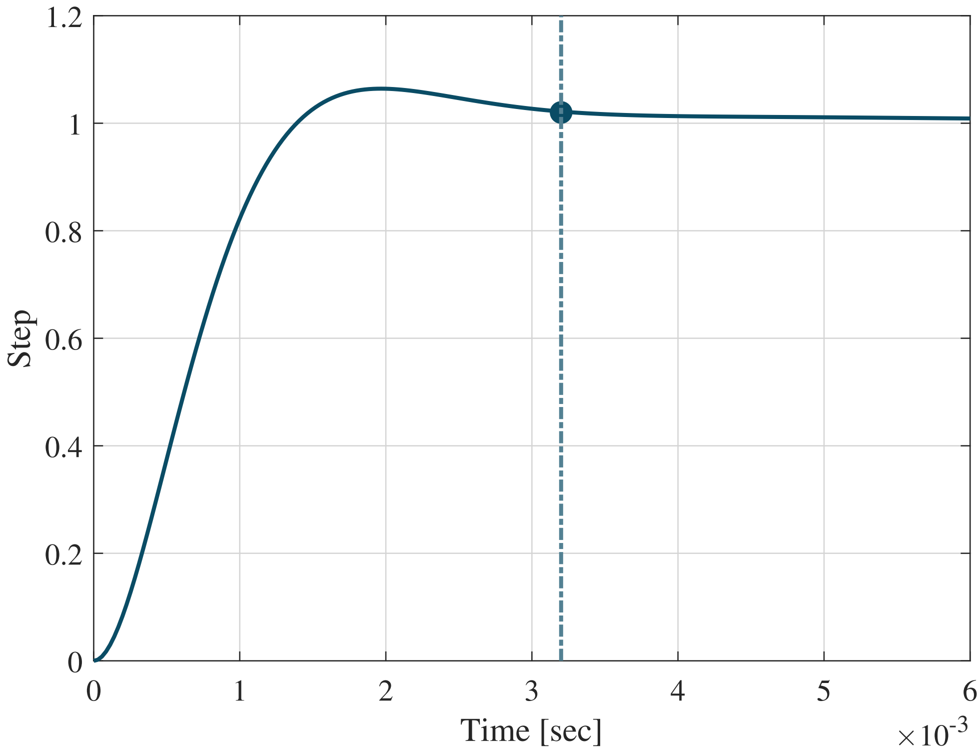

Figure 4.5. Step response of current plant with the designed PI controller.

Settling time	PI gains
$t_s = 0.0032$ [s]	$K_{P,c} = 8$ and $K_{I,c} = 2000$

4.1.2 Design of the Speed Control

When designing the PI controller for the outer speed loop, the same procedure is applied by first deriving the linear system as for the inner current loop. The entire outer speed loop consisting of the PI controller, the inner current loop, the speed plant, and load torque compensation is illustrated in Figure 4.6. The load torque compensation will be discussed in Chapter 5.

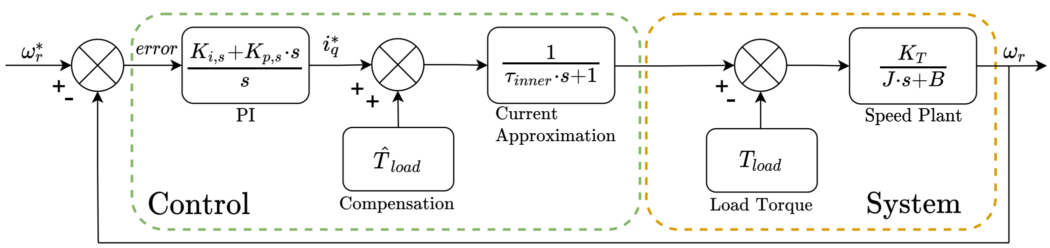

Figure 4.6. Block diagram of the speed loop.

Deriving the speed plant

The equation of motion from Equation 3.12 is brought to the s-domain by applying Laplace transformation and rearranged to:

$$\omega_r = \frac{T_e - T_L}{Js + B} \tag{4.10}$$

$$T_e = \frac{3}{2} \cdot \lambda_{mpm} \cdot N_{pp} \cdot i_q \tag{4.11}$$

From Equation 4.10, the load torque, T_L, is decoupled by considering it as a disturbance. Then by substituting Equation 4.11 into Equation 4.10, it is possible to find the transfer function for the system as:

$$G_{speed}(s) = \frac{\omega_r}{i_q} = \frac{\frac{3}{2} \cdot \lambda_{mpm} \cdot N_{pp}}{Js + B} = \frac{K_T}{Js + B} \tag{4.12}$$

where K_T is the torque constant.

Inner current loop approximation

The closed-loop transfer function for the inner current loop can be approximated as a first-order transfer function, given that the inner loop is much faster than the outer loop. The inner current loop, given by Equation 4.13, consist of the PI current controller, current plant, and a time delay.

$$G_{current} = \frac{K_{i,c} + K_{p,c}\, s}{s} \frac{1}{L_q s + R_s} \frac{1}{T_{delay} s + 1} \tag{4.13}$$

The inner loops first-order time constant, is estimated to be around 1/7 of the current loop settling time $T_{settling,c}$, and may yield the following calculation of the time constant to be:

$$\tau_{inner} = T_{settling,c} \cdot \frac{1}{7} \tag{4.14}$$

The first-order transfer function for the inner loop will be as following:

$$G_{in} = \frac{1}{\tau_{inner} s + 1} \tag{4.15}$$

A Bode plot is shown in Figure 4.7 of the inner and current transfer function where it is seen that the bandwidth is approximately the same.

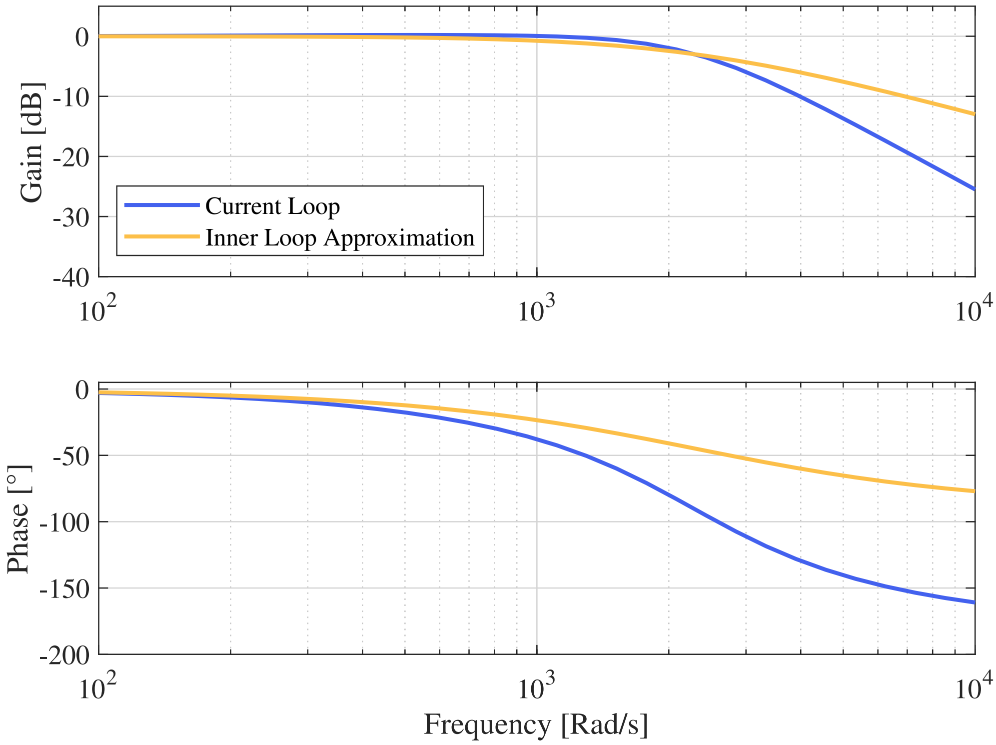

Figure 4.7. Bode plot of the current loop and inner loop approximation.

Design of PI speed controller

Having defined the transfer function for the speed plant and an approximation for the inner current loop, the PI controller is designed. As previously described the FOC control scheme is utilized by a cascade structure, thus the inner current loop should be 5-10 times faster than the outer speed loop. This also make sense from a physical standpoint, as the outer loop is describing the mechanical part of the system, which is inherently slower than the inner loop describing the electrical part of the system. In Figure 4.8 the root locus plot for the outer loop is showing, with the designed PI controller. In addition, by examine the transfer function for the speed plant and inner loop transfer functions, the system poles are located at:

$$p_{speed\,plant} = -\frac{B}{J} = -0.13 \quad and \quad p_{inner\,current} = -\frac{1}{\tau_{inner}} = -1250 \tag{4.16}$$

The PI zero is placed to the left of the pole from the speed plant at $z_{PI} = -2.5$, resulting in the root locus seen in Figure 4.8. The fast pole from the inner loop is not shown in the root locus, as it is located far to the left from the rest of the poles and zero. The closed-loop step response is presented with Figure 4.9, where the final results from the analysis is given in the Table below Figure 4.9.

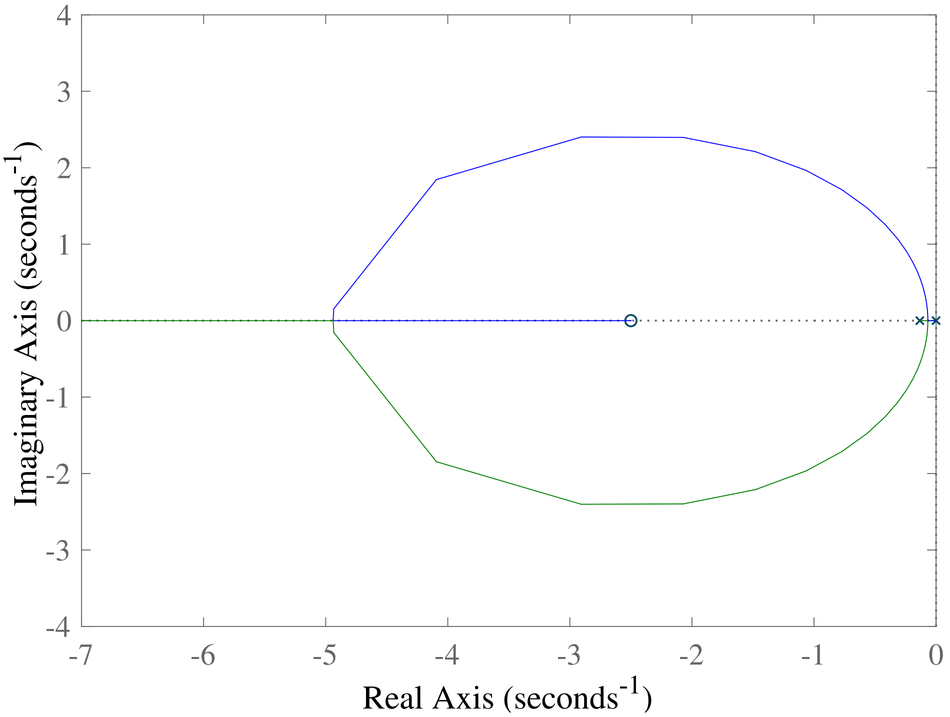

Figure 4.8. Root locus for the speed loop.

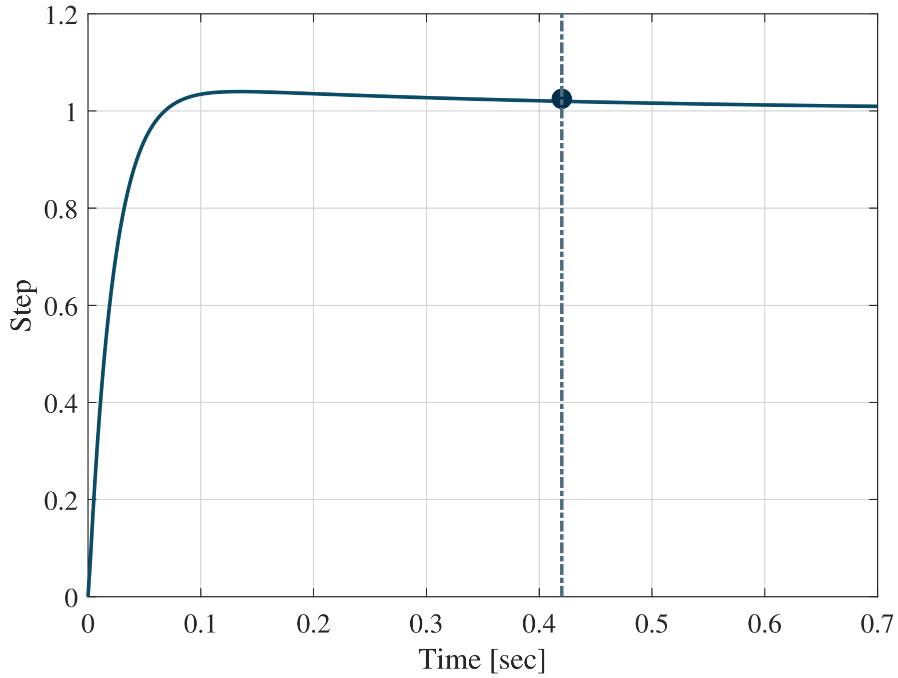

Figure 4.9. Step response of closed loop speed plant with speed PI control.

Settling time	PI gains
$T_{settling,s} = 0.41$ [s]	$K_{p,s} = 0.8$ and $K_{i,s} = 2$

To verify the requirement of having the inner loop to be 5-10 times faster than the outer loop, a bode diagram is made for the the closed loop current control and close loop speed control and is shown on Figure 4.10.

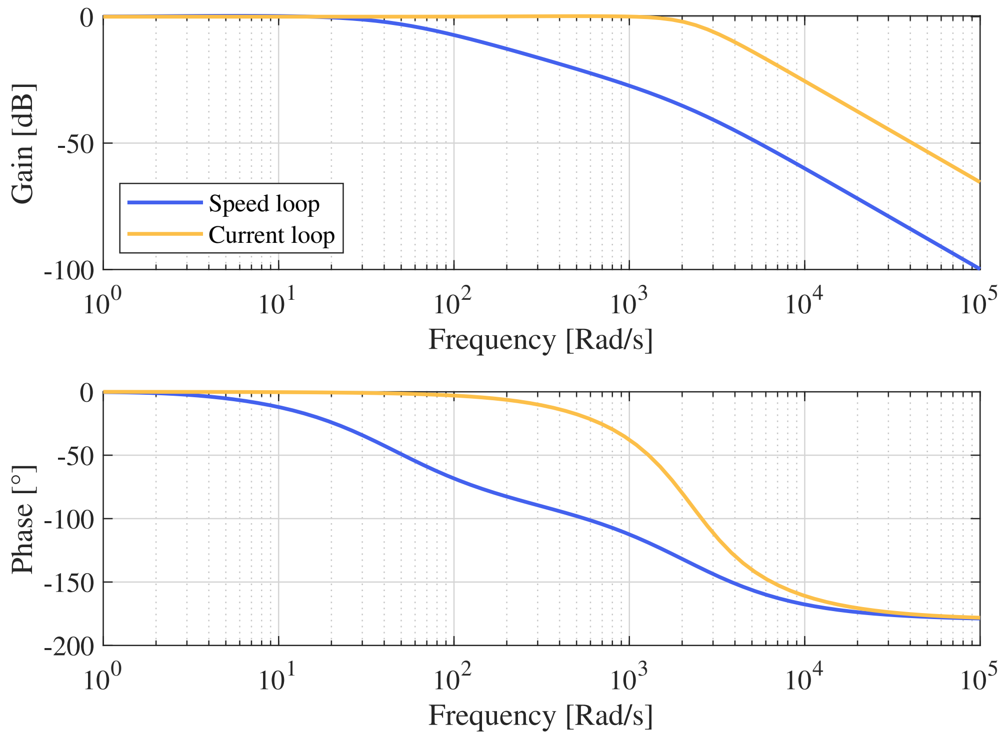

Figure 4.10. Bode plot of closed loop current and speed plants.

As seen on the bode diagram it is clear the bandwidth of the inner current loop is at least 10 times faster than the outer speed loop, and the requirement is therefore satisfied.

4.2 Validation of the Non-Linear Model

In this section, the non-linear mathematical model derived in Chapter 3 is validated based on an experimental test conducted on the physical setup. To validate the non-linear model in Simulink, the speed n_{meas} and current i_q are compared. In addition, a reference trajectory is made for the speed to fully compare the Simulink model with the experimental test data, which is then given as input to the Simulink model. The reference trajectory is presented in Figure 4.11.

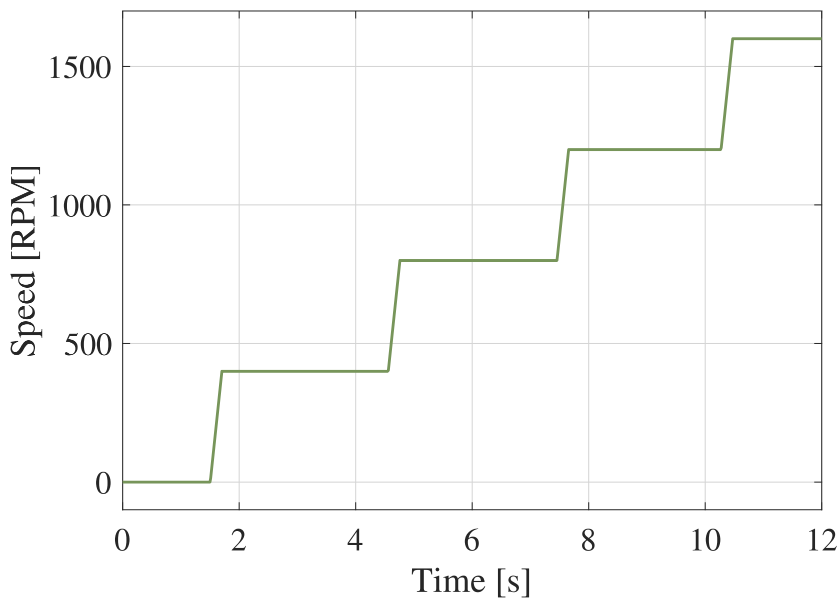

Figure 4.11. Trajectory for the speed reference, used to compare the simulation and experimental test results.

The validation results for the speed and currents are presented in Figure 4.12 and 4.13. The speed PI controller gains had to be retuned to the nonlinear model. The current PI controller worked as intended and needed no additional tuning for simulation and experimental test.

Retuned Speed PI	Current PI
$K_{p,s} = 0.1$	$K_{p,c} = 8$
$K_{i,s} = 2$	$K_{i,c} = 2000$

If comparing the non-linear model and experimental test from Figure 4.12 and 4.13, the non-linear model manages to closely follow the experimental test for both the speed and currents.

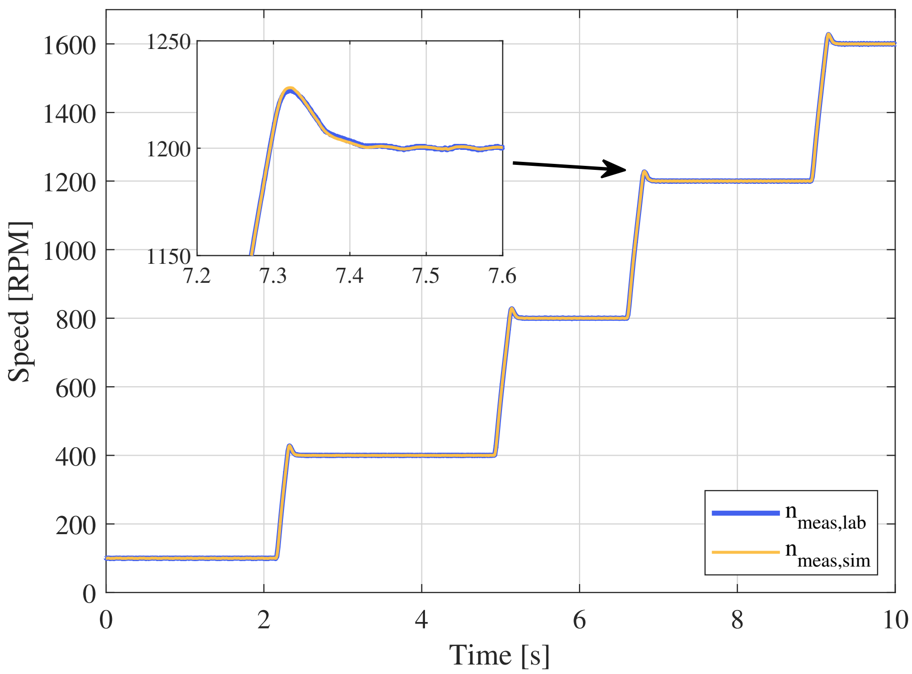

Figure 4.12. Validation results for the speed, where the simulation is compared to the experimental test results.

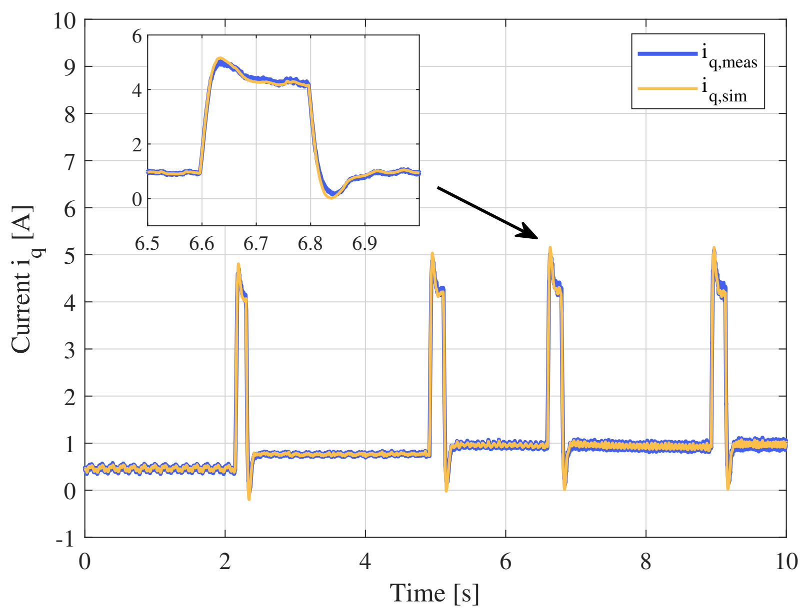

Figure 4.13. Validation results for the current and i_q, where the simulation is compared to the experimental test results.

The speed response is further analyzed when applying a load torque of 4 [Nm] to the Simulink model and the physical setup. The validation results are presented with Figures 4.14 and 4.15.

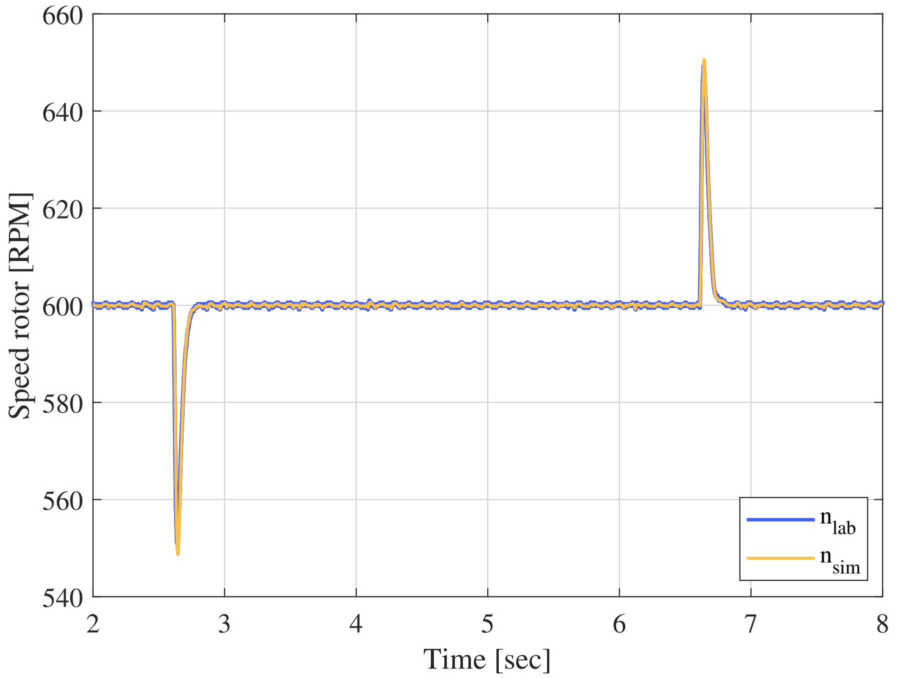

Figure 4.14. Validation results for the speed with a load torque step of 4 [Nm], where the simulation is compared to the experimental test results.

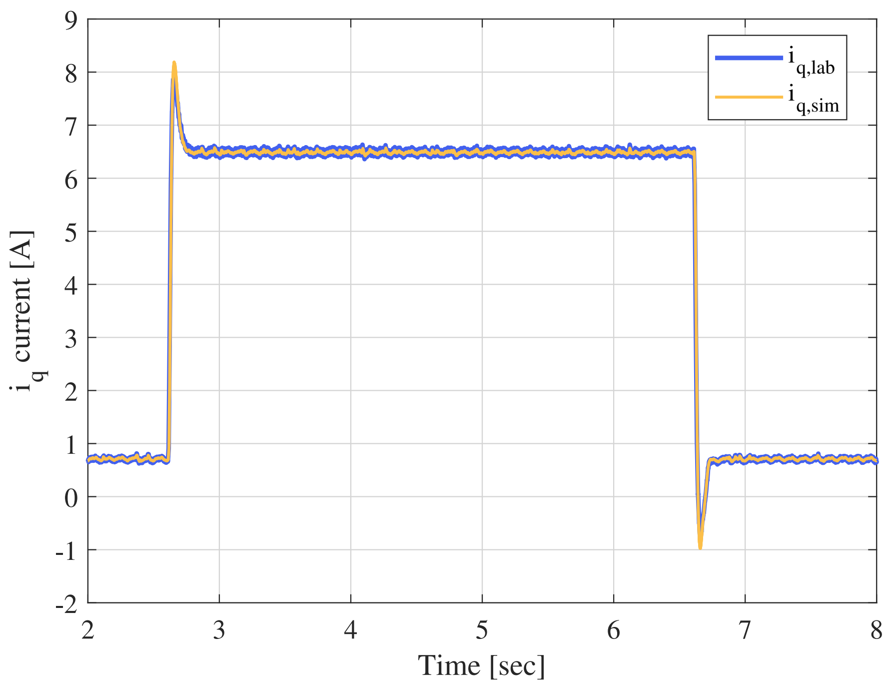

Figure 4.15. Iq current during a load step. Load torque vector in simulation is based on lab data.

When comparing the speed results and its corresponding i_q current, it is noted that the experimental results have slightly higher peak values than the simulation. The PI gains given from the Subsection 4.1.2 were used in both the experimental setup and in the simulation, however, due to parameter uncertainties, such as inertia and friction, there will be a slight difference from the real system to the simulation.

To conclude this section the Simulink model manages to closely follow the experimental test results for the currents and the speed with and without a load torque and is therefore considered representative.

Load Torque Identification Sliding Mode Observer 5

In Chapter 4 the control strategy was described, which included PI controllers for the speed and current loop based on the linear system. To derive the linear speed plant, the load torque was considered a disturbance, which would entail the drive system working well under no-load conditions. However, if a load torque is applied, the overall motor performance will be degraded. Therefore, this chapter concerns the load torque disturbance. Different LTID-SMO methods are designed and implemented into the FOC control structure to compensate for the load torque disturbance.

5.1 Strategy

The main objective of the LTID-SMO is to improve the transient part of the speed response when a load torque is applied to the SPMSM. To minimize the transient part of the speed response, the control scheme of the LTID-SMO is implemented into the FOC structure by feeding forward a load torque estimation. In practice, the SMO is used to estimate the actual load torque given from the load machine. The estimated load torque can then be transformed into an estimated current, which then is added to the reference current provided by the PI speed controller ($i_q^* + \hat{i}_q^*$).

The general idea of adding an extra current component is to enable the PI current controller to work more effectively when a load torque is applied to the drive system. When a load torque is applied, the PI current controller will have to increase its current amplitude to counteract the sudden error in the speed response. Therefore, adding the estimated current will increase the amplitude to a more suitable level for handling the change in speed when a load torque is applied.

The implementation of the LTID-SMO in the FOC structure is presented in Figure 5.1, where it may be noted the LTID-SMO uses the i_q and i_d currents and the electrical angular speed as inputs.

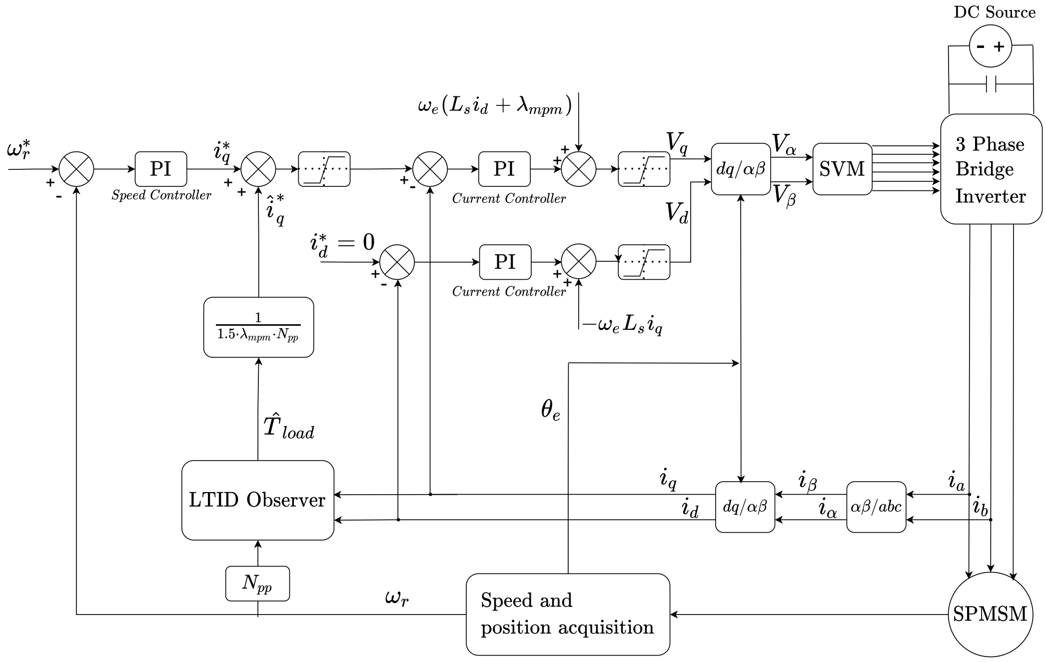

Figure 5.1. The FOC structure with implemented load torque identification sliding mode observer.

The chapter presents four different SMO-based methods to estimate load torque, where the first two methods taking basis in [1]. The objective is to analyze each method and compare their performance based on how well each technique improves the transient part of the speed response when a load torque is applied.

The first method presented in Section 5.2, is a *conventional SMO* using a signum switching function with the controller output given as:

$$u(\sigma, t) = -K \cdot \text{sign}(\sigma(t)) \tag{5.1}$$

where $K \in \mathbb{R}^+$.

The conventional SMO can be used to effectively estimate the load torque. However, the main drawback of using the conventional SMO is the chattering phenomenon. It produces a high-frequency switching signal around the sliding surface due to the discontinuous nature of the sign function. The chattering phenomenon can cause the physical system to decrease in efficiency over time, resulting from faster wear of the moving mechanical parts [15]. Therefore an additional LTID-SMO control schemes are proposed to overcome the chattering issue.

The second method presented in Section 5.3, is the *boundary layer method* that replaced the discontinuous sign function with a saturation function. This will inherently reduce the chattering in the drive system as the saturation function can be seen as a linear approximation of the sign function and the problem with discontinuity will be solved. This is further illustrated in Figure 5.2, where $\Delta = 0$ would entail the same response as the Signum function. The boundary layer method has the controller output given as:

$$u(\sigma, t) = -K \cdot \text{sat}\left(\frac{\sigma(t)}{\Delta}\right) \tag{5.2}$$

where $K \in \mathbb{R}^+$ and Δ determines the limit of the boundary around the switching surface. In addition, further improvement of the LTID-SMO using a saturation function is made by implementing an extra feedback loop in the load torque observer to improve the estimation accuracy.

The third method presented in Section 5.4, is the Power-Sigmoid method, a proposed method based on the characteristic response of an odd-power function[16] and a Sigmoid function. If combining the odd-power function with a Sigmoid function, by raising the sliding variable, σ, to the power of α the controller output is defined by Equation 5.3. An example of the profile of the Power-Sigmoid function can be seen in Figure 5.2.

$$u(\sigma, t) = -K \cdot \frac{\sigma(t)^\alpha}{|\sigma(t)|^\alpha + \delta} \tag{5.3}$$

with $\alpha \cup \{2n - 1 \,|\, n \in \mathbb{N}\}$ and $\delta > 0$.
Using this controller have the advantages of suppressing chattering in areas for low σ values. For high σ values the controller can be tuned to have similarly effect as the boundary layer method, by tuning the α and δ value.

The fourth method presented in Section 5.4, are taking basis in the third method where the sliding mode gain, K, is replaced with PI controller, which gives the following controller output:

$$u(\sigma, t) = -\left(K_P + \frac{K_I}{s}\right) \cdot \frac{\sigma(t)^\alpha}{|\sigma(t)|^\alpha + \delta} \tag{5.4}$$

with $\alpha \cup \{2n - 1 \,|\, n \in \mathbb{N}\}$ and $\delta > 0$.
The advantages by using this method is to further reduce the chattering by controlling the sliding variable towards zero, where the Switching Function Output is very low.

Each method will be mathematically derived to present the principles of the observer structure, where a stability analysis will be carried out for each of the methods. Finally, the sliding mode gains will be determined based on the stability analysis.

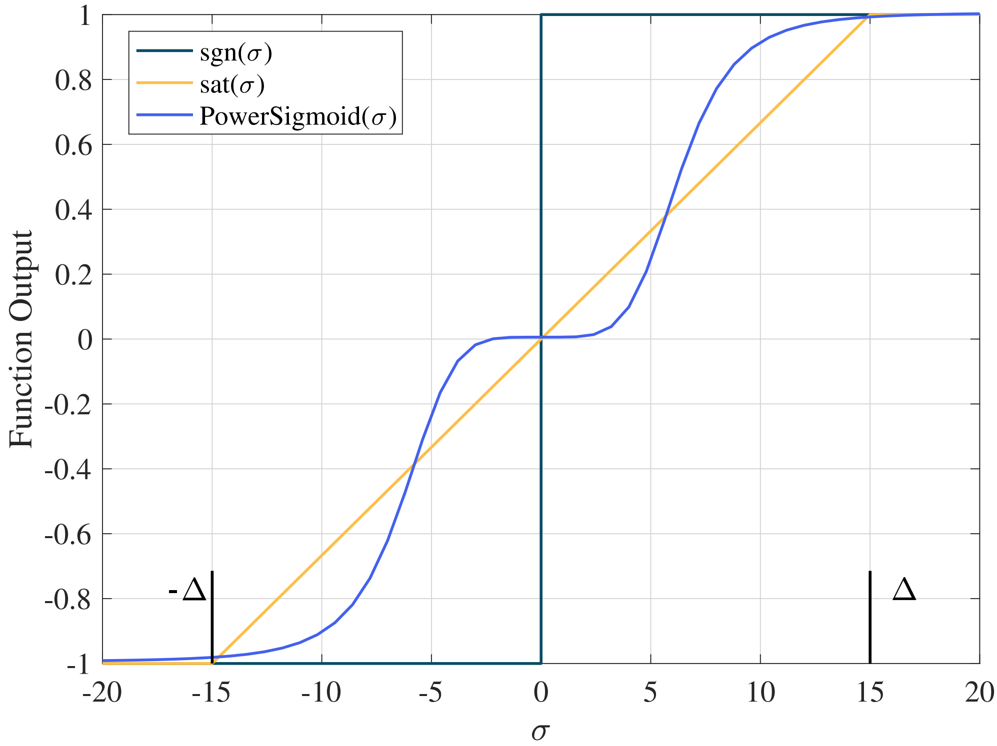

Figure 5.2. A comparison of the profiles for the sign function, saturation function and power-sigmoid functions.

5.2 LTID-SMO using Signum Switching Function

To derive the LTID-SMO using Signum Switching Function (LTID-SMO-Sign), Equation 3.12 and 3.15 is utilized, and is given by the motion equation and the torque equation respectively. The LTID-SMO takes basis in the acceleration ($\dot{\omega}_e$) of the SPMSM and can be found by substituting Equation 3.15 into 3.12 and isolating for the acceleration, yielding:

$$\frac{d\omega_e}{dt} = \frac{K_T N_{pp}}{J} i_q - \frac{B}{J}\omega_e - \frac{N_{pp}}{J} T_L \quad where \quad K_T = \frac{3}{2}\lambda_{mpm} N_{pp} \tag{5.5}$$

Taking the electrical angular speed and load torque as the observer object, the LTID-SMO can be obtained and shown with Equation 5.6. The load torque indication signal, Z_s, is determined by the Sign function, depended on the speed error ($\tilde{\omega}_e = \hat{\omega}_e - \omega_e$), multiplied by the sliding mode gain K_{sign}.

$$\frac{d\hat{\omega}_e}{dt} = \frac{K_T N_{pp}}{J} i_q - \frac{B}{J}\hat{\omega}_e - Z_s \quad where \quad Z_s = K_{sign} \cdot sign(\hat{\omega}_e - \omega_e) \tag{5.6}$$

Defining the sliding surface as the speed error the following is obtained:

$$\sigma(t) = \tilde{\omega}_e = \hat{\omega}_e - \omega_e \tag{5.7}$$

In accordance with [17], when $\dot{\sigma}(t) = 0$ the system state variable has reached the sliding surface and by that having achieved steady-state conditions. Utilizing the steady-state condition, the load torque can be obtained by subtracting Equation 5.6 from 5.5 and isolate for T_L:

$$\frac{d\tilde{\omega}_e}{dt} = \frac{N_{pp}}{J}T_L - \frac{B}{J}\tilde{\omega}_e - Z_s = 0 \tag{5.8}$$

$$\Rightarrow T_L = \frac{J}{N_{pp}}Z_s + \frac{B}{N_{pp}}\tilde{\omega}_e \tag{5.9}$$

where $\frac{B}{N_{pp}}\tilde{\omega}_e \ll \frac{J}{N_{pp}}Z_s$, leaving that the term $\frac{B}{N_{pp}}\tilde{\omega}_e$ can be neglected.

In addition, as previously described, the sign function in the LTID-SMO can lead to high-frequency noise and increased chattering. Therefore to effectively reduce the chattering in the estimated load torque, an LPF is implemented. Thus the estimated load torque may be formulated as:

$$\hat{T}_L = \frac{J}{N_{pp}}Z_s \cdot \frac{\omega_c}{s+\omega_c} \tag{5.10}$$

To gain an enhanced overview, a block diagram is presented in Figure 5.3 showing the above described principles of the LTID-SMO using a signum function.

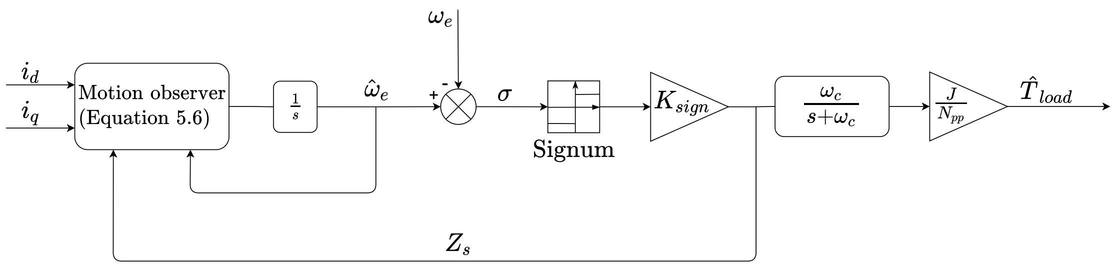

Figure 5.3. A block diagram showing the principles of the LTID-SMO using a signum function.

5.2.1 Stability analysis

The Lyapunov function is used to prove the stability of the observer and define the observer gain. The Lyapunov candidate function is defined as:

$$V = \frac{1}{2}\sigma^2 \tag{5.11}$$

The Lyapunov function given by Equation 5.11 is chosen since it is positive definite (P.D). If taking the derivative of the Lyapunov function, a stability analysis can be made. Providing the correct values for the tunable observer parameters will ensure that the state does not tend to infinity but goes to zero. For the observer to be stable, $\dot{V}$ needs to be at least negative semi-definite (N.S.D) and most optimal if $\dot{V}$ is negative definite (N.D), meaning the equilibrium is asymptotically stable and tends to zero in a finite time [18].

$$\dot{V} = \sigma \cdot \dot{\sigma} < 0 \tag{5.12}$$

Utilizing that $\dot{\sigma} = \dfrac{d\tilde{\omega}_e}{dt}$, the derivative of the Lyapunov candidate may be defined as:

$$\dot{V} = \sigma \cdot \dot{\sigma} = \left(\frac{N_{pp}}{J} T_L - \frac{B}{J}\sigma - Z_s \right) \sigma \tag{5.13}$$

As the switching function for the SMO-LTID uses a sign function the following conditions must be applied:

$$\dot{V} = \begin{cases} -\frac{B}{J}\sigma^2 + \left(\frac{N_{pp}}{J} T_L - K_{sign} \right) \sigma & , \quad \sigma \geq 0 \\ -\frac{B}{J}\sigma^2 + \left(\frac{N_{pp}}{J} T_L + K_{sign} \right) \sigma & , \quad \sigma < 0 \end{cases} \tag{5.14}$$

According to the Lyapunov stability criteria, $\dot{V}$ is negative definite if all terms in Equation 5.14 are negative. The term $-\frac{B}{J}\sigma^2$ will always be negative as σ^2, B, and J always will be positive values. Therefore to have all terms negative, the sliding mode gain is defined as:

$$K_{sign} > \frac{N_{pp} T_L}{J} \tag{5.15}$$

To ensure a stable observer, the above-described condition must be satisfied. Therefore a sanity check is made by investigating the stability of the observer when applying a load torque of $T_L = 5.8\,[\mathrm{Nm}]$ which leaves Equation 5.15 to become:

$$K_{sign} > 1856 \quad \text{Threshold value for :} \quad T_L = 5.8\,[\mathrm{Nm}] \tag{5.16}$$

Therefore if K_{sign} is chosen to be above the threshold value, the observer is stable for all cases of $T_L \leq 5.8\,[\mathrm{Nm}]$. To further elaborate on this, the Simulink model are given a load step from $T_L = 0\,[\mathrm{Nm}]$ to $T_L = 7\,[\mathrm{Nm}]$, where it is expected the observer becomes unstable and not able to estimate the load torque when reaching a load step of $T_L = 5.8\,[\mathrm{Nm}]$. The analysis is presented in Figure 5.4.

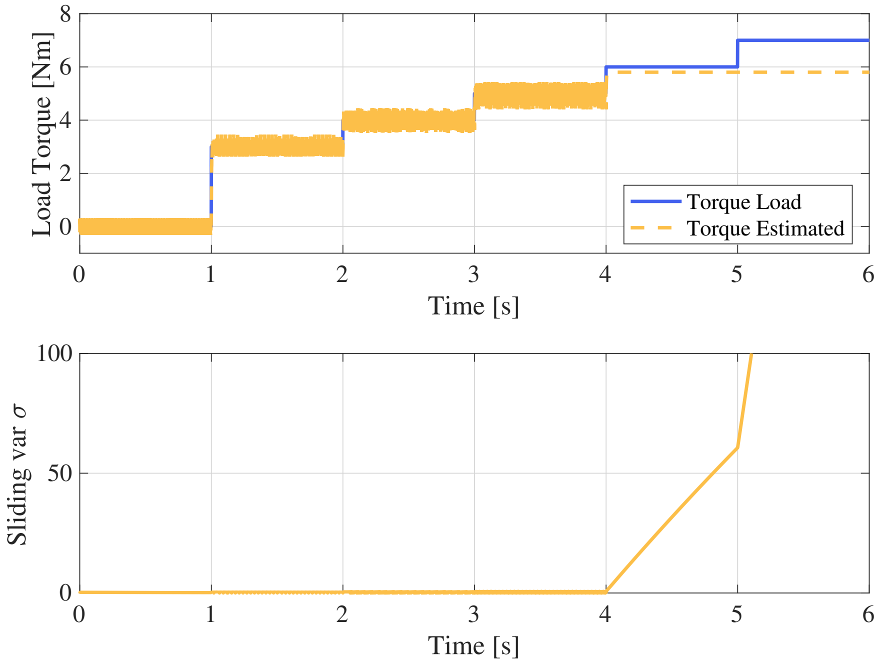

Figure 5.4. Sanity check of Equation 5.15, where the sliding variable σ have be analyzed when above the threshold value set by K_{sign}. Throughout the analysis the low-pass filter cutoff frequency remains the same at $\omega_c = 500\,[\text{rad/s}]$.

As seen in Figure 5.4 the SMO is stable for $T_L \leq 5.8\,[\text{Nm}]$ and becomes unstable for $T_L > 5.8\,[\text{Nm}]$ and is thereby unable to estimate the load torque for the given sliding mode gain of $K_{sign} = 1856$. From the sanity check, it can be concluded that the condition given by Equation 5.15 must remain satisfied at all times, to ensure a stable operation of the SMO.

5.2.2 Impact of parameters of the LTID-SMO using a signum function

The Simulink model is used to analyze the sliding mode gain and the LPF's cutoff frequency. To choose the sliding mode gain and cutoff frequency, three performance criteria are used as guidelines to determine the most suitable values. The performance criteria are given as follows:

1. Ensure the SMO can handle all cases of $T_L \leq T_{L,max}$.
2. Improve the transient response for the estimated load torque.
3. Chattering should remain as low as possible.

The first criteria are mainly used when determining the sliding mode gain and are considered the only hard requirement of the performance criteria. After that, criteria 2 and 3 are used to define the sliding mode gain and the cutoff frequency.

Stipulation of the Sliding Mode Gain

The first part of the analysis is carried out by investigating the impact of the sliding mode gain. The SMO is disconnected from the FOC, and the LPF are bypassed when analyzing the sliding mode gain. The sliding mode gain contributes to how large the chattering is. Therefore, if the sliding mode gain is reduced, less chatter will be present and vice versa for an increase in K_{sign}. This is further illustrated in Figure 5.5.

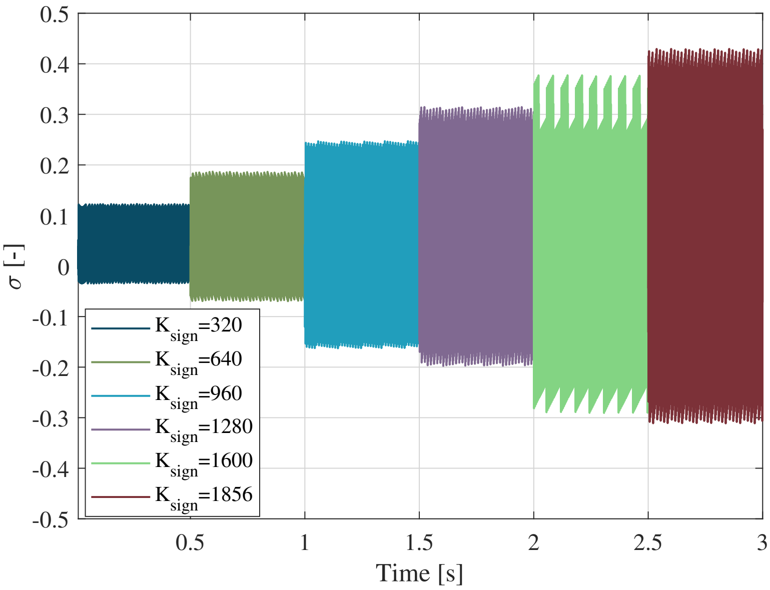

Figure 5.5. Increased chattering in the SMO without any load step. The K_{sign} values was calculated by using Equation 5.15 to determine benchmark values from $T_L = 1\,[\text{Nm}]$ to $T_{L,max} = 5.8\,[\text{Nm}]$.

To ensure the SMO can operate under all load conditions, the load torque dynamics are investigated by applying $T_{L,max}$ to the SPMSM model, where the load torque dynamic described in Section 3.2 has been included. The investigation of the load torque is carried out by applying a step response of $T_{L,max} = 5.8$ to the Simulink model. The result is seen in Figure 5.6.

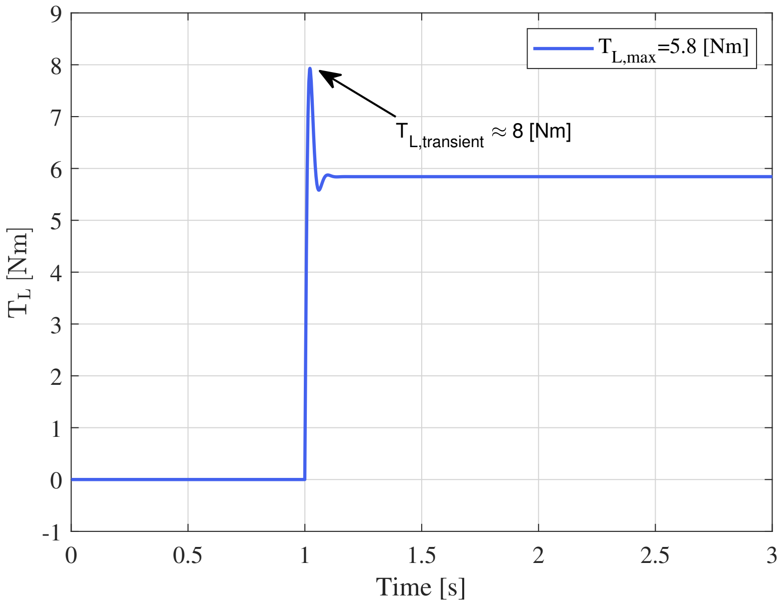

Figure 5.6. Analysis of the load dynamic, with a step input of $T_{L,max} = 5.8\,[\text{Nm}]$.

As seen in the figure, when including the load dynamic, the maximum load torque during the transient part of the step response is increased to $T_{L,transient} \approx 8\,[\text{Nm}]$. Therefore if the transient part is taken into account, the sliding mode gain should at least be above $K_{sign} > 2560$ ensuring a stable SMO during operation for all load torque cases. However, the disadvantage of determining K_{sign} above $T_{L,transient}$, resulting in the K_{sign} value, will be over-dimension in cases of $T_L < T_{L,max}$ and further filtering is needed to compensate for the increased chattering.

Next, the transient response for the estimated load torque is analyzed when increasing the sliding mode gain. To analyze the transient response of $\hat{T}_L$, the transfer function for the LTID - SMO is derived. Thereby classical control theory can be used to analyze the dynamical response of $\hat{T}_L$ when a load is applied. To derive the linear model of the SMO with the output/input relation of $\frac{\hat{T}_L}{T_L}$, Equation 5.8 and 5.10 is used.

Equation 5.8 and 5.10 is brought to the Laplace domain and rearranged to obtain the following transfer functions:

$$G_{\tilde{\omega}_e}(s) = \frac{\tilde{\omega}_e}{T_L} = \frac{\frac{N_{pp}}{JB}}{s + \frac{K_{sign}}{B}} \tag{5.17}$$

$$G_{\hat{T}_{L,sign}}(s) = \frac{\hat{T}_L}{\tilde{\omega}_e} = \frac{\frac{JK_{sign}\omega_c}{N_{pp}}}{s + \omega_c} \tag{5.18}$$

The linear model described by the relationship of $\frac{\hat{T}_L}{T_L}$ is obtained by multiplying Equation 5.17 with 5.18:

$$G_{SMO,sign}(s) = \frac{\hat{T}_L}{T_L} = \frac{\frac{K_{sign}\omega_c}{B}}{(s + \frac{K_{sign}}{B})(s + \omega_c)} \tag{5.19}$$

To verify the linear model can represented by the non-linear model, the transfer function given by Equation 5.19 is implemented into the Simulink model with the load dynamic described by Equation 3.17. Then, a step input of $T_{L,max}$ is applied to both the linear and non-linear model. Finally, the validation results are presented in Figure 5.7.

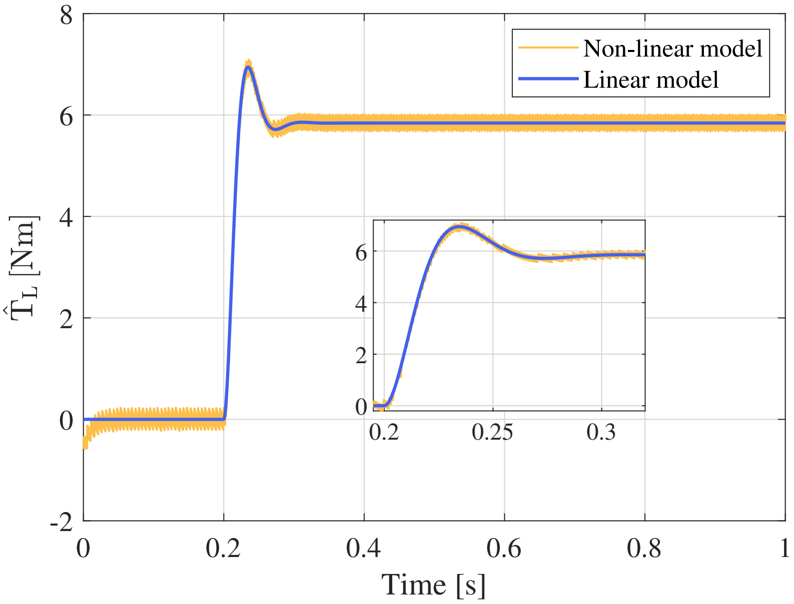

Figure 5.7. Validation results for the linear model of the estimated load torque with the transfer function: $G(s) = G_{SMO,sign}(s) \cdot G_{Load}(s)$.

The figure shows that the linear model can follow the non-linear model with high precision. Therefore, the linear model can be further used to investigate the dynamical response of the estimated load torque.

The transfer function given by Equation 5.19 consist of two first-order transfer functions, with two real poles given from $G_{\tilde{\omega}_e}(s)$ and $G_{\hat{T}_{L,sign}}(s)$, where $\omega_c \ll \frac{K_{sign}}{B}$ which entails only the pole located at $s = -\omega_c$ will influence the dynamical response of $\hat{T}_L$ when being varied. Therefore it is concluded that the sliding mode gain can not improve the transient response of $\hat{T}_L$ when K_{sign} is increased. The sliding mode gain should be chosen to remain as low as possible to decrease the chattering in the system while still being large enough to ensure the SMO is stable. As previously described, the sliding mode gain should at least be above $K_{sign} > 2560$ to ensure a SMO stability. However, as this requirement is determined based on the calculated load torque without LTID-SMO connected to the FOC and with a motor speed at 600 [RPM]. An extra 50% safety margin is added to ensure stability for higher speeds and with the LTID-SMO connected to the FOC, leaving the sliding mode gain is determined as:

$$K_{sign} = 3840$$

Stipulation of the LPF Cutoff Frequency

The next part of the analysis is carried out by investigating how the LPF impacts the estimated load torque and the speed response. Therefore, the SMO is connected to the FOC by feeding forward the current, $\hat{i}_q^*$, given from the estimated load torque, making it possible to investigate how the speed response is affected by a change in ω_c.

In general, adding an LPF into the observer structure will contribute to some amount of phase delay to the estimated load torque. This will affect the estimation accuracy, which then leads to the error between the real and estimated load torque being greater than zero ($e_{T_L} = T_L - \hat{T}_L > 0$). When $e_{T_L} > 0$ it will impact the performance of the drive system negatively as the PI controllers in the FOC will have to take this offset into account, resulting in a larger overshoot in the speed response when a load step is applied. To grasp this idea, an illustration is made in Figure 5.8 and 5.9 for $e_{T_L} \approx 0$ and $e_{T_L} > 0$.

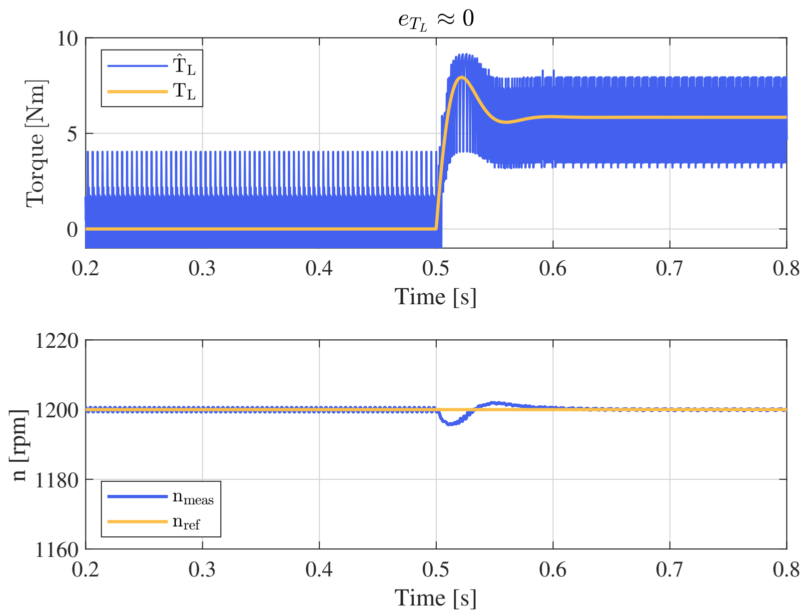

Figure 5.8. Top Figure showing the error between the estimated and real load torque with $\omega_c = 300\,[\mathrm{Hz}]$. Bottom Figure showing the corresponding speed response.

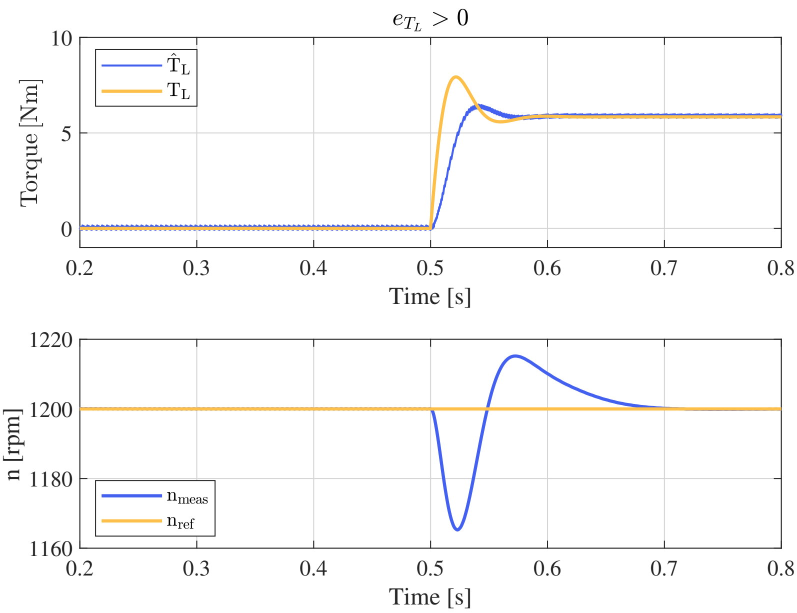

Figure 5.9. Top Figure showing the error between the estimated and real load torque with $\omega_c = 10\,[\text{Hz}]$. Bottom Figure showing the corresponding speed response.

Figure 5.8 and 5.9 showing two cases with a high and low value of ω_c, which only serve the purpose of illustrating how the speed response is affected. It is, however, clear the transient part of the speed response is improved when driving the error between the real and estimated load torque close to zero. To drive e_{T_L} close to zero, the cutoff frequency will have to be increased significantly to minimize the phase delay from the LPF. However, the disadvantages of choosing a high cutoff frequency will result in large chattering, as seen in Figure 5.8, which may cause the system to become unstable. Therefore when choosing ω_c, it is decided the cutoff frequency should not exceed a value of $45\,[\text{Hz}]$ ensuring the chattering is kept to an acceptable level.

For the determination of the cutoff frequency, an analysis is made with Equation 5.19 in combination with the load dynamic, leaving the transfer function for the estimated load torque to be defined as:

$$G(s) = \frac{\hat{T}_L}{T_L} = \frac{\frac{K\omega_c}{B}}{(s+\frac{K}{B})(s+\omega_c)} \cdot \frac{135.8s + 9813}{s^2 + 109s + 9743} \tag{5.20}$$

For analyzing the cutoff frequency, a step response is made with a sweep for different values of ω_c from $10\,[\text{Hz}]$ to $45\,[\text{Hz}]$. The objective is to choose ω_c without compromising the dynamical response of $\hat{T}_L$ too much while still reducing e_{T_L}. The analysis is presented in Figure 5.10 and 5.11.

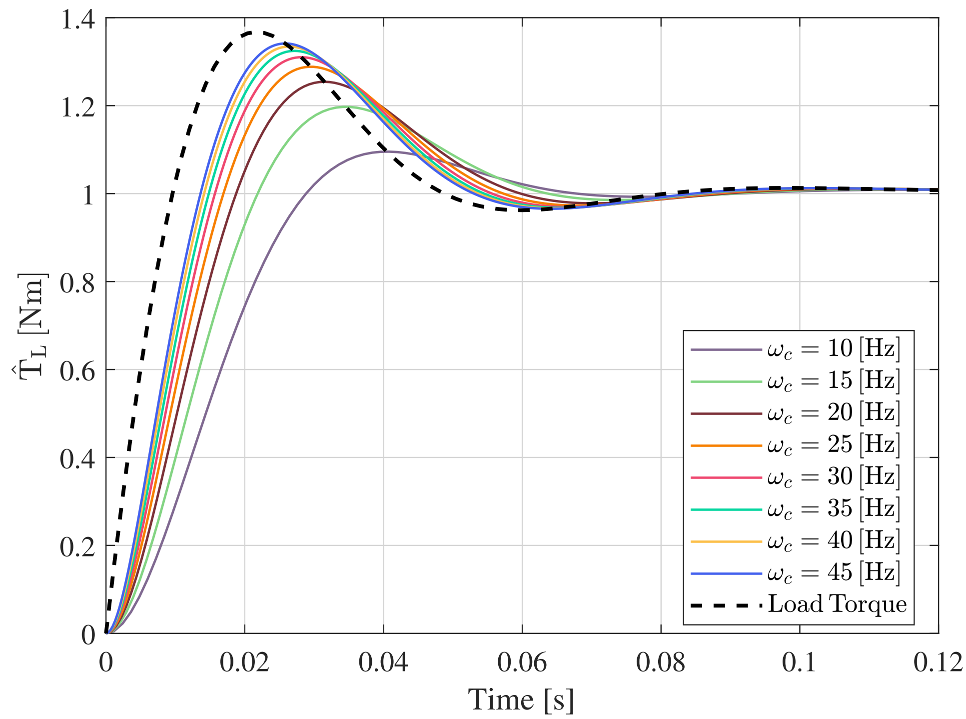

Figure 5.10. Analysis of the cutoff frequency with a sweep from $\omega_c = 10\,[\text{Hz}]$ to $\omega_c = 45\,[\text{Hz}]$ for G(s). The load torque are given by Equation 3.17.

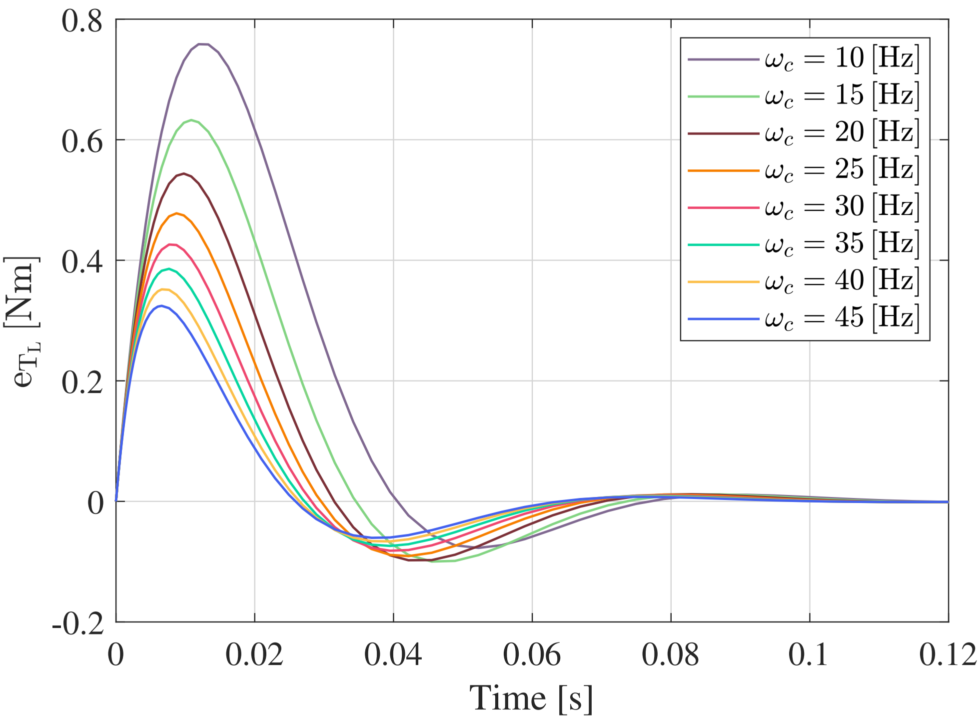

Figure 5.11. The error e_{T_L} between the real and estimated load torque, shown for its corresponding linear models. The error was calculated based on Figure 5.10, with the sweep of the cutoff frequency from $\omega_c = 10\,[\text{Hz}]$ to $\omega_c = 45\,[\text{Hz}]$.

As seen in Figure 5.10 and 5.11, the dynamical response of $\hat{T}_L$ and the error e_{T_L} does not change significantly for values above 35 [Hz]. Based on this observation, the cutoff frequency is determined to be:

$$\omega_c = 35\,[\mathrm{Hz}] \approx 220\,[\mathrm{rad/s}]$$

Using the above determined observer gains for the LTID-SMO-Sign, the simulation results for the estimated load torque and the corresponding speed response are shown in Figures 5.12 and 5.13 where the actual load torque is used. The speed response shows a small reduction in recovery time and a large improvement on the peak to peak speed error compared to with no SMO. The estimated load torque shows a lot of chatter however still managing to estimate the actual load well.

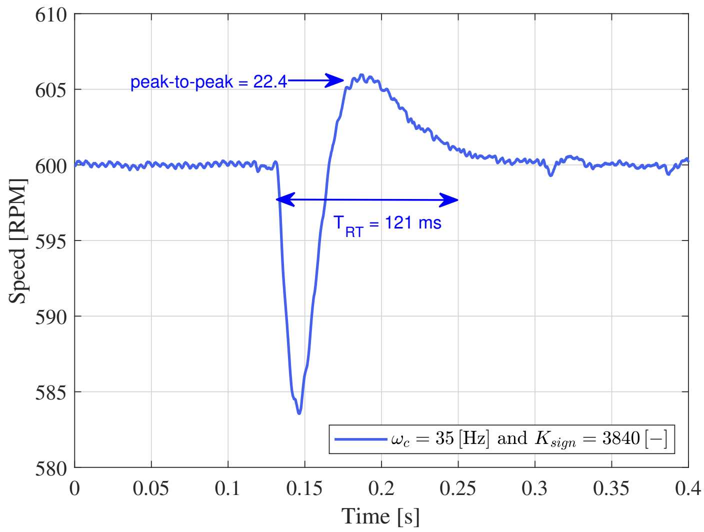

Figure 5.12. Simulation result for the speed response where the actual load torque are used. The speed response are made with the predetermined parameters for the sliding mode gain and cutoff frequency.

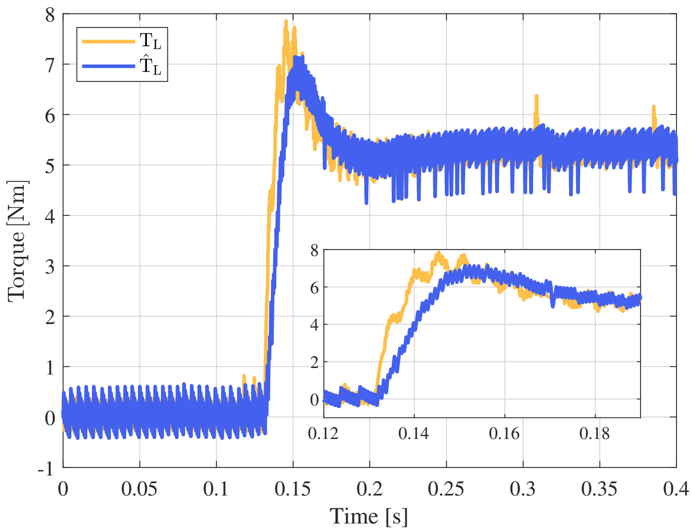

Figure 5.13. Simulation result for the estimated load torque compared to the actual load torque.

5.3 LTID-SMO using Saturation Switching Function

When deriving the LTID-SMO with the saturation function (LTID-SMO-Sat), the same procedure is applied as described with the conventional SMO using a Sign function, by substituting Equation 3.15 into 3.12, leaving the motion equation to be defined as:

$$\frac{d\omega_e}{dt} = \frac{K_T N_{pp}}{J} i_q - \frac{B}{J}\omega_e - \frac{N_{pp}}{J} T_L \quad where \quad K_T = \frac{3}{2}\lambda_{mpm} N_{pp} \tag{5.21}$$

The LTID-SMO can be determined by taking the angular speed and load torque as observer objects and is therefore formulated as:

$$\frac{d\hat{\omega}_e}{dt} = \frac{N_{pp} K_T}{J} i_q - \frac{B}{J}\hat{\omega}_e - Z_s - LZ_{es} \tag{5.22}$$

By defining the sliding surface as the speed error as $\sigma(t) = \tilde{\omega}_e = \hat{\omega}_e - \omega_e$, and subtracting the motion Equation 5.21 from Equation 5.22 the derivative of the speed error is obtained:

$$\frac{d\tilde{\omega}_e}{dt} = \frac{T_L N_{pp}}{J} - \frac{B\tilde{\omega}_e}{J} - Z_s - LZ_{es} \tag{5.23}$$

If utilizing the steady-state condition when $\dot{\sigma}(t) = 0$ the estimated load torque can be defined as:

$$\hat{T}_L = (Z_s + LZ_{es})\frac{J}{N_{pp}} + \frac{B}{N_{pp}}\tilde{\omega}_e \tag{5.24}$$

Where the term $\frac{B}{N_{pp}}\tilde{\omega}_e$ is neglected, as $\frac{B}{N_{pp}}\tilde{\omega}_e \ll (Z_s + LZ_{es})\frac{J}{N_{pp}}$, leaving that:

$$\hat{T}_L = (Z_s + LZ_{es})\frac{J}{N_{pp}} \tag{5.25}$$

The estimated load torque contains the motor inertia, viscous friction, feedback gain, L, and the two components Z_s and Z_{es} defined as [19]:

$$Z_s = K_{sat} \cdot \text{sat}\left(\frac{\tilde{\omega}_e}{\Delta}\right) \quad and \quad Z_{es} = Z_s \frac{\omega_c}{s + \omega_c} \tag{5.26}$$

Here the term Z_s is the output signal from the saturation function. The term Z_{es} is the filtered Z_s through a LPF, and contains mostly the lower frequency components of Z_s.

In addition, from Equation 5.23, it should be clear the main difference from the LTID-SMO with a sign function is the use of a saturation function and added feedback term LZ_{es}, to represent the average estimated load torque. The added term will introduce an extra component to increase the damping in the SMO and the overall system state, making it possible to further improve the estimation accuracy.

Figure 5.14 presenting a schematic shown with a block diagram for the above-described principles of the LTID-SMO using a saturation function.

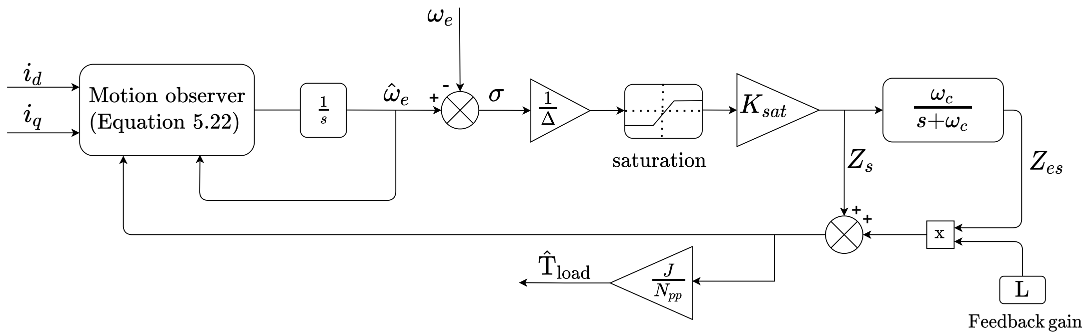

Figure 5.14. A block diagram showing the principles of the LTID-SMO using a saturation function.

5.3.1 Stability analysis

To prove stability of the observer and to determine the observer gains, the Lyapunov candidate function and its derivative, defined in Section 5.2.1, is again used and repeated here:

$$V = \frac{1}{2}\sigma^2 \quad and \quad \dot{V} = \sigma \cdot \dot{\sigma} < 0 \tag{5.27}$$

During the stability analysis, the load torque is assumed to be constant, and the system has reached steady-state, leaving $Z_s = Z_{es}$ if the cutoff frequency of the LPF is high enough. This means: When $\sigma \geq \Delta$, the output from the saturation function is constant and $Z_s = Z_{es} = K_{sat}$. For the case when $\sigma \leq -\Delta$ it becomes $Z_s = Z_{es} = -K_{sat}$. When the SMO is sliding around the sliding surface $-\Delta < \sigma < \Delta$ it can be approximated that $Z_s = Z_{es} = K_{sat}\frac{\sigma}{\Delta}$.

It was defined that $\dot{\sigma} = \dfrac{d\tilde{\omega}_e}{dt}$. If Equation 5.23 is inserted into the Lyapunov function derivative, given by Equation 5.27, the following 3 cases of switching operation is obtained in Equation 5.28:

$$\sigma \cdot \dot{\sigma} = \begin{cases} -\frac{B\sigma^2}{J} + \left[\frac{N_{pp}T_L}{J} - (1+L)K_{sat}\right]\sigma & , \sigma > \Delta \\ -\frac{B\sigma^2}{J} + \left[\frac{N_{pp}T_L}{J} - (1+L)K_{sat}\frac{\sigma}{\Delta}\right]\sigma & , -\Delta < \sigma < \Delta \\ -\frac{B\sigma^2}{J} + \left[\frac{N_{pp}T_L}{J} + (1+L)K_{sat}\right]\sigma & , \sigma < -\Delta \end{cases} \tag{5.28}$$

Analyzing Equations 5.28, the stability can be proved based on the choice of the parameters. The Lyapunov theory states that $\dot{V}(\sigma) < 0 \;\; \forall \;\; \sigma \neq 0$ (N.D.) and $V(\sigma) \rightarrow \infty$ for $|\sigma| \rightarrow \infty$ (P.D.), to be globally asymptotically stable [18]. This is true if all the terms in $\dot{V}$ add together to be negative. The term $-\frac{B\sigma^2}{J} < 0$ is valid as B and J are positive parameters, σ^2 will always be positive, and $-(1+L)K_{sat}\frac{\sigma^2}{\Delta} < 0$ is also true.

For Equation 5.27 to be fulfilled, the following has to be true:

$$\left[\frac{N_{pp}T_L}{J} - (1+L)K_{sat}\right]\sigma < 0 \tag{5.29}$$

Isolating each part yields:

$$\frac{N_{pp}T_L}{J} < (1+L)K_{sat} \tag{5.30}$$

K and L can be chosen together to satisfy Equation 5.30. The load torque will be assumed to be the maximum possible torque the motor will experience. If isolating for the feedback gain L, the relation between K_{sat} and L becomes:

$$L > \frac{N_{pp}T_{L,max}}{J\,K_{sat}} - 1 \tag{5.31}$$

The observer can then perform sliding mode motion as this will satisfy the stability criteria for Equation 5.27. Figure 5.15 demonstrates the load steps being increased and the correlated estimated load torque to show a situation where the relationship is not satisfied. The maximum load torque is $T_{L,max} = 5.8\,[\text{Nm}]$. Thereby, if the load torque exceeds this, the relation 5.31 is no longer true, and the SMO cannot estimate the correct load torque

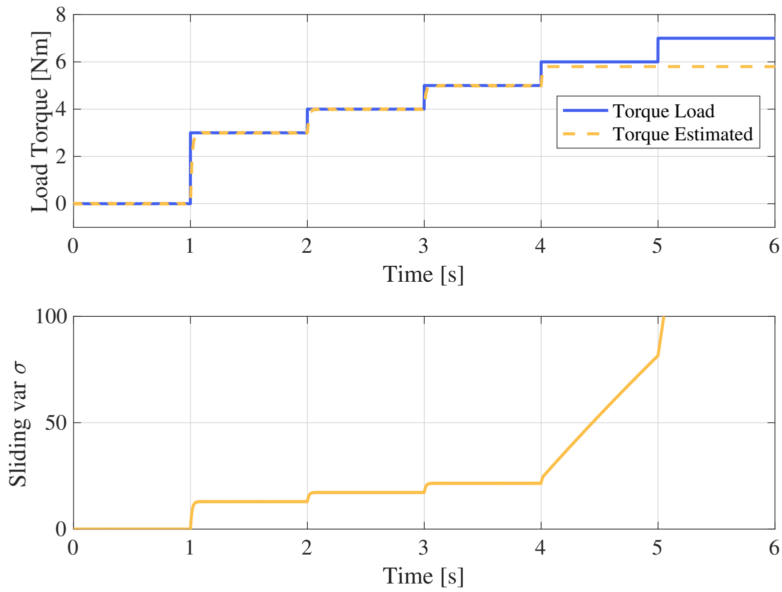

Figure 5.15. Load torque steps to demonstrate that feedback gain L will cause the observer to be unstable, thereby not estimating correctly, if the load torque is higher than the maximum expected load torque of $T_{L,max}$.

Therefore, to ensure Equation 5.31 is always true, a factor of $k_f = 2$ is multiplied onto parts of the equation to give some extra safety margin. Ensuring the feedback gain, L, always will be appropriately large and the system always fulfills the stability criteria. However, when tuning the observer gains, the factor, k_f, may be changed if it can improve the estimation performance.

$$L = k_f \cdot \frac{N_{pp}T_{L,max}}{J\,K_{sat}} - 1 \tag{5.32}$$

5.3.2 Impact of parameters of the LTID-SMO using a saturation function

As stated earlier, $Z_s = Z_{es} = K_{sat}\frac{\sigma}{\Delta}$ when operating around sliding surface, and as there due to the switching function will be some chattering in the estimated output, the LPF is used to suppress this. The signal through the LPFs primary function, is to suppress the chatter in the estimated torque during steady state, where the load torque doesn't change. As a LPF also adds a phase lag, a feedback that is directly fed back without filtering is used to estimate the torque in the transient part of the load changes to have fast response.

The error Equation 5.23 defining the sliding surface is converted to the Laplace domain:

$$s\tilde{\omega}_e = -\frac{B}{J}\tilde{\omega}_e + \frac{N_{pp}}{J}T_L - \frac{K_{sat}}{\Delta}\tilde{\omega}_e\Big(1 + L\frac{\omega_c}{s+\omega_c}\Big) \tag{5.33}$$

$(s+\omega_c)$ is multiplied on all terms gives:

$$(s+\omega_c)s\tilde{\omega}_e = -(s+\omega_c)\frac{B}{J}\tilde{\omega}_e + (s+\omega_c)\frac{N_{pp}}{J}T_L - \frac{K_{sat}}{\Delta}\tilde{\omega}_e\Big((s+\omega_c) + L\omega_c\Big) \tag{5.34}$$

By rearranging the terms in order of the Laplace operator yields:

$$s^2\tilde{\omega}_e + \Big(\frac{B}{J} + \frac{K_{sat}}{\Delta} + \omega_c\Big)s\tilde{\omega}_e + \Big(\frac{B}{J} + \frac{K_{sat}}{\Delta}(1+L)\Big)\omega_c\tilde{\omega}_e = \frac{N_{pp}}{J}\Big(T_L s + \omega_c T_L\Big) \tag{5.35}$$

Collecting everything on the right side of the equation by diving through with the left side, then isolating $\frac{\tilde{\omega}_e}{T_L}$ gives the transfer function:

$$\frac{\tilde{\omega}_e}{T_L} = \frac{N_{pp}(s+\omega_c)}{J\Big(s^2 + \big(\frac{B}{J} + \frac{K_{sat}}{\Delta} + \omega_c\big)s + \big(\frac{B}{J} + \frac{K_{sat}(1+L)}{\Delta}\big)\omega_c\Big)} \tag{5.36}$$

From this it can be seen the system is stable, based on the Routh-Hurwitz criteria [14], if: $\big(\frac{B}{J} + \frac{K_{sat}}{\Delta} + \omega_c\big) > 0$ and $\big(\frac{B}{J} + \frac{K_{sat}(1+L)}{\Delta}\big)\omega_c > 0$, which is always true if the values are positive and follows the criteria from Equation 5.31.

The damping factor for the transfer function can be written as:

$$\zeta = \frac{\big(\frac{B}{J} + \frac{K_{sat}}{\Delta} + \omega_c\big)}{2\sqrt{\Big(\frac{B}{J} + \frac{k_f N_{pp} T_L}{J\Delta}\Big)\omega_c}} \tag{5.37}$$

A sweep of Δ shows the change of the damping ratio seen in Figure 5.16. This shows that besides at very low Δ, increasing Δ should provide more damping to the speed error estimation.

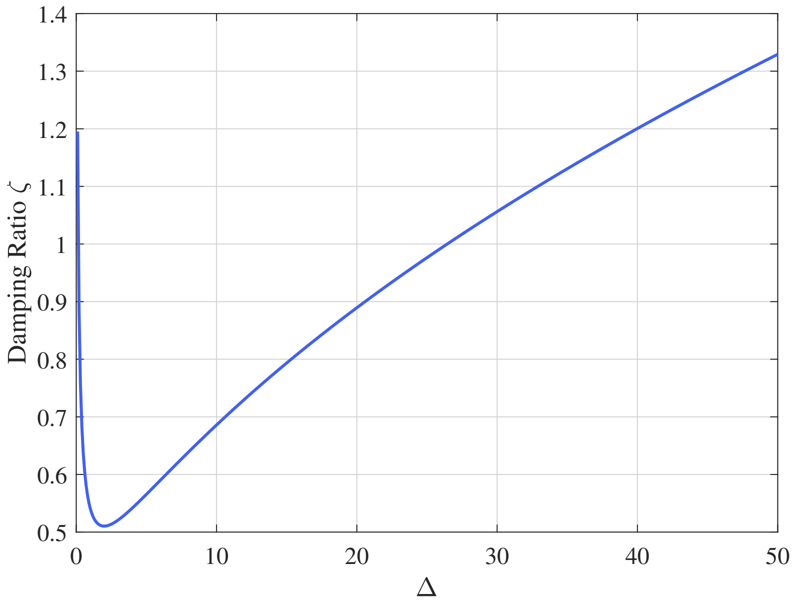

Figure 5.16. Damping ratio with a sweep of different Δ values. In addition, the damping ration is calculated based on Equation 5.37.

Load Torque Dynamics

The real load torque is as described in Section 3.2. As the perfect step in load torque is not possible in reality, to more accurately understand the behavior of the observer when a load torque is applied in lab, this load dynamic will be included in the analysis when understanding the effect of the parameters. By multiplying the transfer function from Equation 5.36 with the load dynamic transfer function from Equation 3.17 the following is obtained:

$$\frac{\tilde{\omega}_c}{T_L} = \frac{N_{pp}(s+\omega_c)}{J\Big(s^2 + \big(\frac{B}{J} + \frac{K_{sat}}{\Delta} + \omega_c\big)s + \big(\frac{B}{J} + \frac{K_{sat}(1+L)}{\Delta}\big)\omega_c\Big)} \cdot \frac{135.8s + 9813}{s^2 + 109s + 9743} \tag{5.38}$$

The parameters should be tuned to give low chattering and good estimation of the sliding variable when a load torque is applied. However, due to the influences of the dynamics of a load torque, the parameters is also considered in relation to the actual load torque. By looking at the poles of the observer and the load torque transfer function it should be possible to learn some insides into the system behavior.

5.3.3 Tuning in simulation

The load step used for the simulation is based on the measurement from the lab setup, as described in Chapter 4 Section 3.2. The simulation runs at 600 RPM and are given a load step from $0 - 5$ [Nm]. However, it should be noted in the analysis that the estimated load torque reaches a steady-state value above the 5 [Nm] and is primarily caused by a static offset from the Coulomb friction.

Stipulation of the sliding mode gain K_{sat}

The three graphs below, Figure 5.17, 5.18 and 5.19 is showing the simulation running with three different sliding mode gains K_{sat}. The additional parameters are kept constant at $\Delta = 25$, $k_f = 2$ and a cutoff frequency of $\omega_c = 250$ [rad/s].

From Figure 5.17 the estimated load torque are presented. Here, for $K_{sat} = 800$, the estimated load torque is close to the actual load torque in amplitude but does not manage to closely follow the actual load torque during the transient part of the step response. For $K_{sat} = 11000$, the estimated load torque is slightly closer to the actual load torque during the transient part and is, therefore, better to estimate the actual load torque. This is also seen Figure 5.18, where a $K_{sat} = 11000$ is resulting in the smallest speed error. From Figure 5.19 a pole-zero map is shown, where it is noted that the poles for higher K_{sat} values will result in the complex conjugated poles only consisting of a real part, where one of the poles will move further into the LHP and the other towards zero. Suppose K_{sat} is increased to values above 11000. In that case, one pole will move toward the right half plane and become more dominating where the other will move further to the left. Faster poles will result in a faster dynamical response, which should give a better estimation of the actual load torque. Where as slower poles will in the lab test result in dominating behavior from the observer, potentially causing a bad response. The gain should therefor not be too high as to not influence the actual load torque dynamic too much by having a slow observer pole. Based on these considerations, the sliding mode gain is chosen to be $K_{sat} = 11000$.

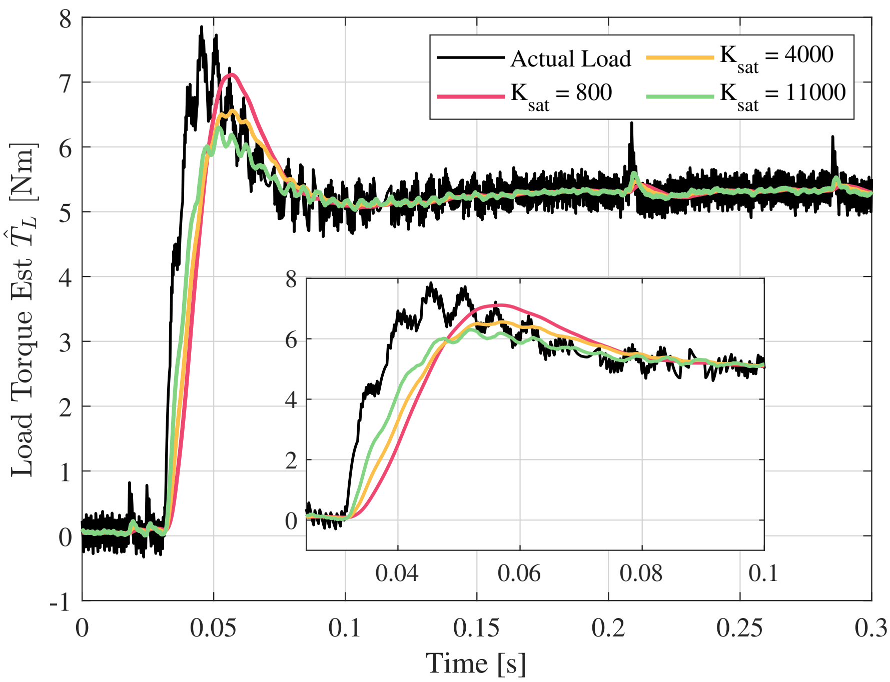

Figure 5.17. A comparison of estimated load torques for different sliding mode gains with the actual applied load torque.

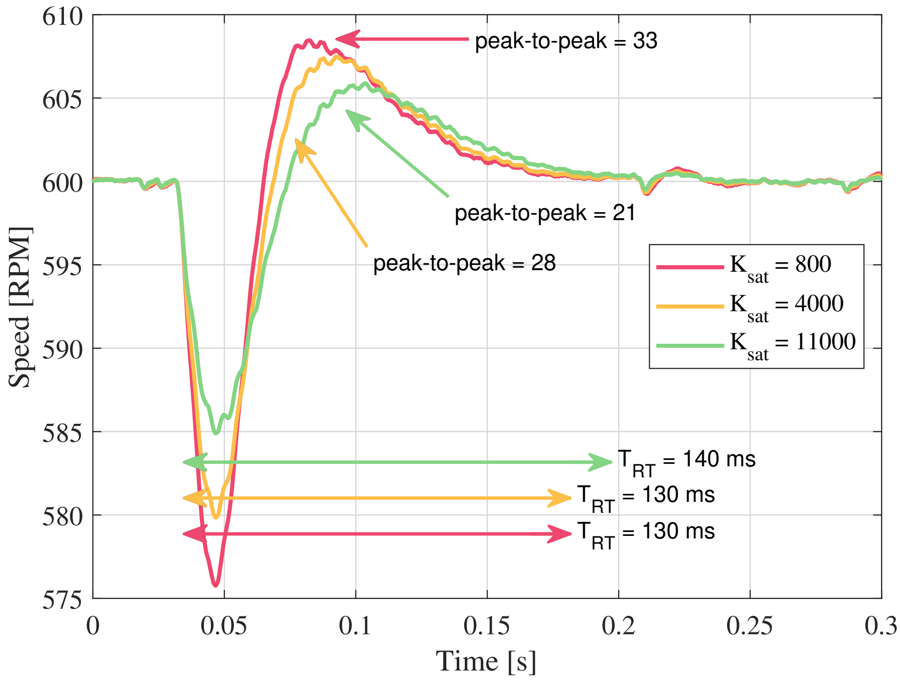

Figure 5.18. A comparison of the speed response for different sliding mode gains, where the recovery time and peak-to-peak values are made to better compare each sweep.

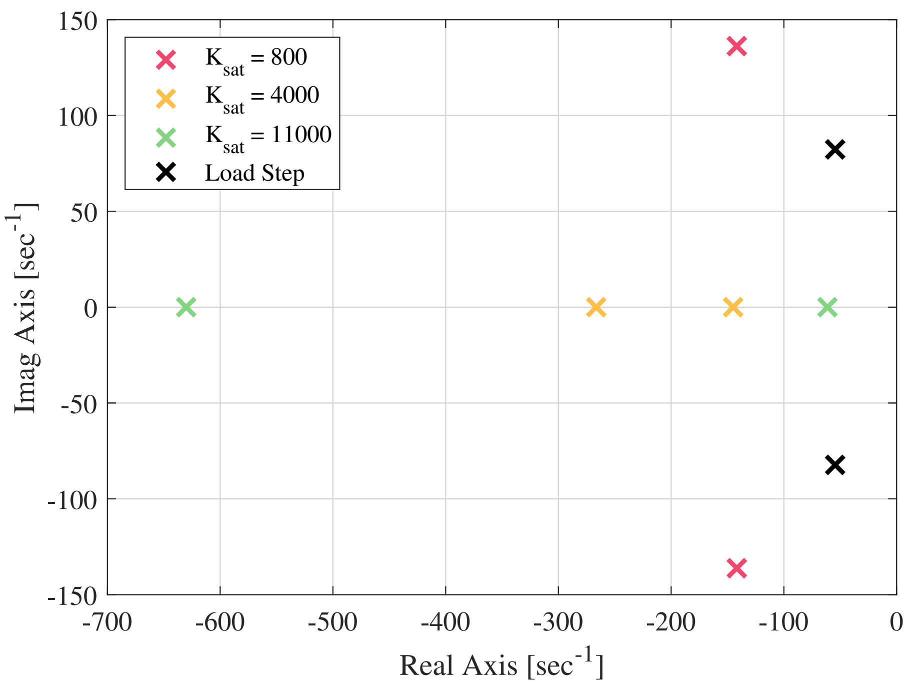

Figure 5.19. Pole-zero map, showing the corresponding placement of the pole for each sweep of the sliding mode gain.

Stipulation of Δ

The three graphs below, Figure 5.20, 5.21 and 5.22 is showing the simulation results for three different values of Δ, with $K_{sat} = 4000$ and $L = 2$. The LPF has a cutoff frequency of $\omega_c = 250$ [rad/s].

From Figure 5.20, it is clearly seen how an increase in Δ also increased the damping in the system. This behavior is also expected from the theory, as Figure 5.16 shows the same characteristic. Therefore, to obtain a closer estimation of the actual load torque, the damping should be decreased by lowering the Δ value. As a result, the speed response becomes significantly improved, which is further seen in Figure 5.21. However, the issue with lowering Δ, will also entail the SMO being much more susceptible to chatter, which can pose serious issues in physical lab setup. In Figure 5.22 a pole-zero map is shown to describe how the poles are located when Δ is being varied. Here it should be noted, that no complex conjugated poles are shown, due to the chosen parameters for K_{sat} and L results in the system being over-damped and thereby only real poles are shown. By increasing Δ the poles move further toward the RHP and becomes more dominating. As a result, the damping increases and the bandwidth decreases. Based on these considerations, the Δ value is chosen to be $\Delta = 25$.

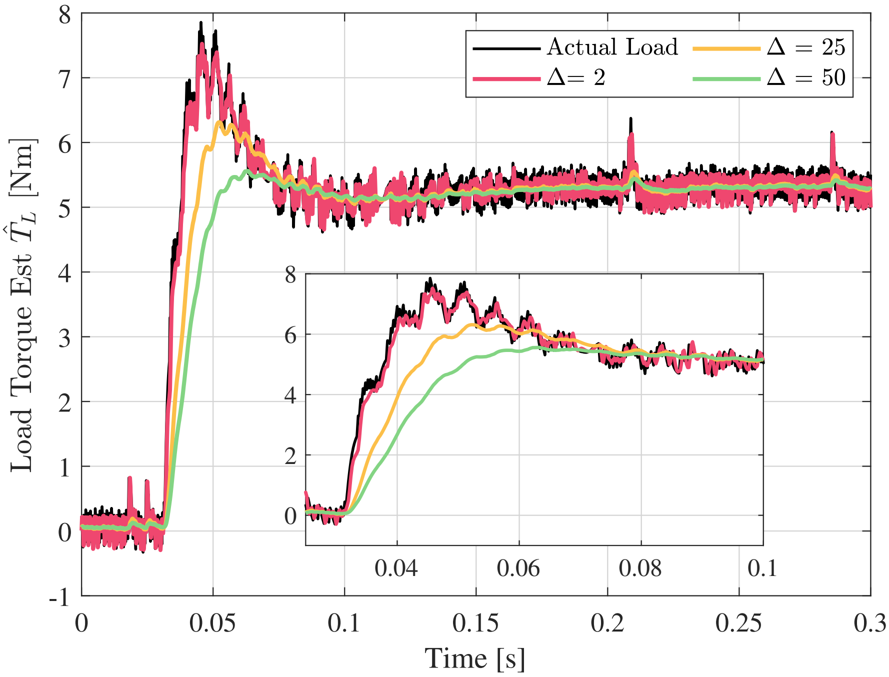

Figure 5.20. The estimated load torques for different Δ values compared with the actual load torque.

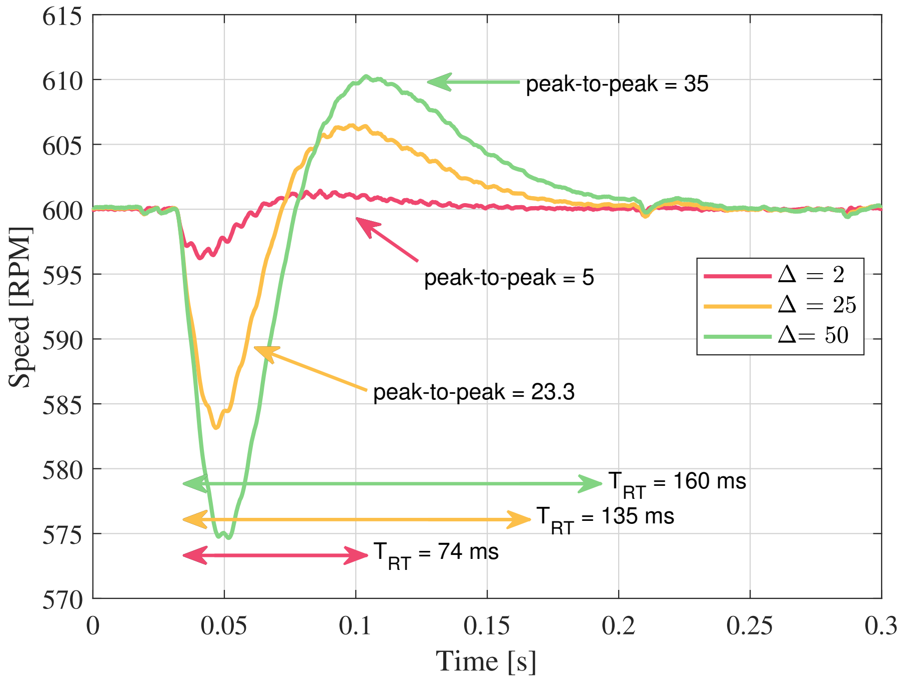

Figure 5.21. A comparison of the speed response for different Δ values, where the recovery time and peak-to-peak values are shown to better compare each sweep.

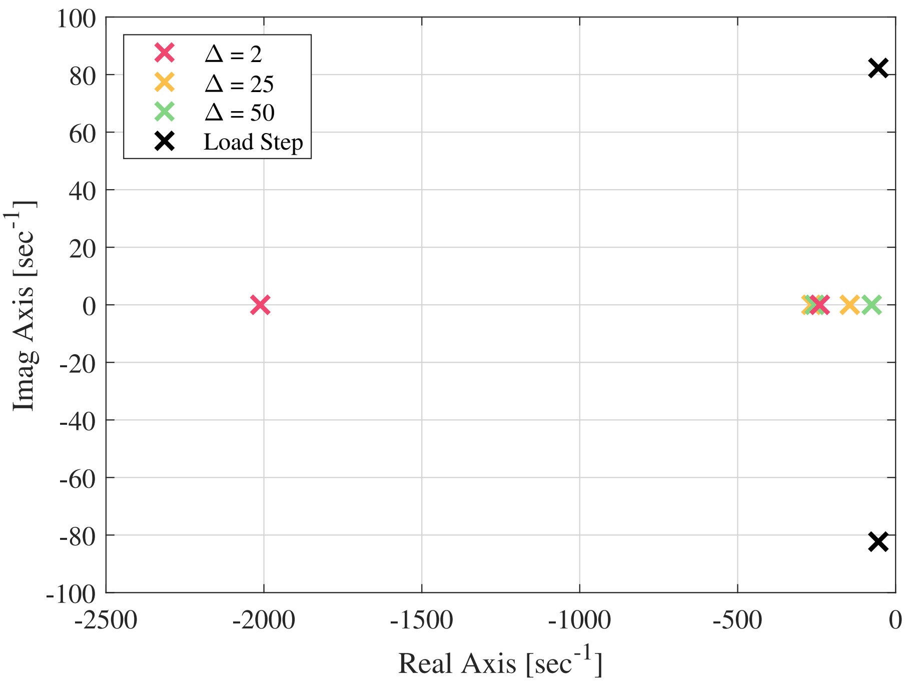

Figure 5.22. Pole-zero map, showing the corresponding placement of the pole for each sweep of Δ.

Stipulation of k_f

The three graphs below, Figure 5.23 to 5.25 is showing the simulation running with three different factors on L, with $K_{sat} = 4000$ and $\Delta = 25$. The LPF has a cutoff frequency of

$\omega_c = 250\,[\text{rad/s}]$. The idea from the extra feedback is to improve steady state performance. L is calculated based on Equation 5.32, this means the gain K_{sat} affects the size of L, however the factor k_f allows to tune L independently as well. The factor k_f can minimum be 1 as to not fail the criteria from Equation 5.31. It can be notices that a larger k_f gives better approximation of the load torque which improves the speed response. From the pole plot it can be seen that increasing k_f, makes the poles complex conjugate, which can improve transient response of the estimation. A fast response with some under damping seems to improve the overall estimation speed and accuracy. Based on these considerations, the k_f value is chosen to be $k_f = 2.5$.

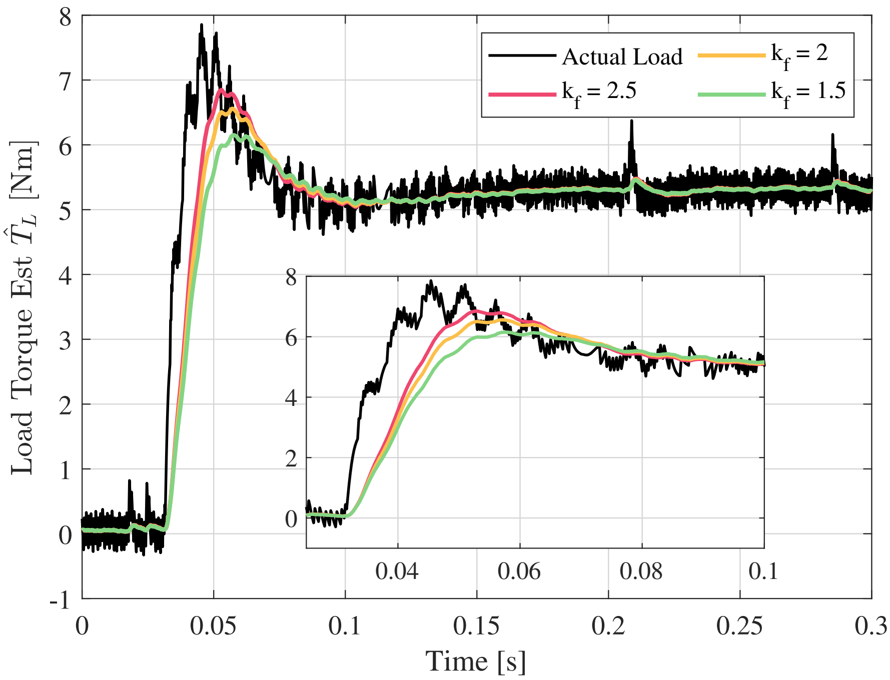

Figure 5.23. The estimated load torques for different k_f values compared with the actual load torque.

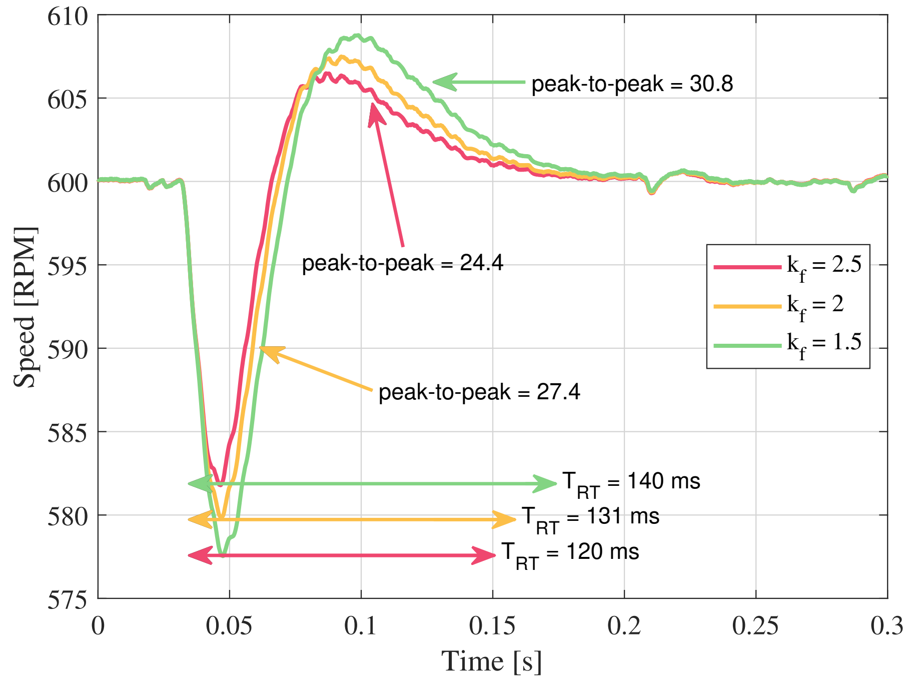

Figure 5.24. A comparison of the speed response for different k_f values, where the recovery time and peak-to-peak values are shown to better compare each sweep.

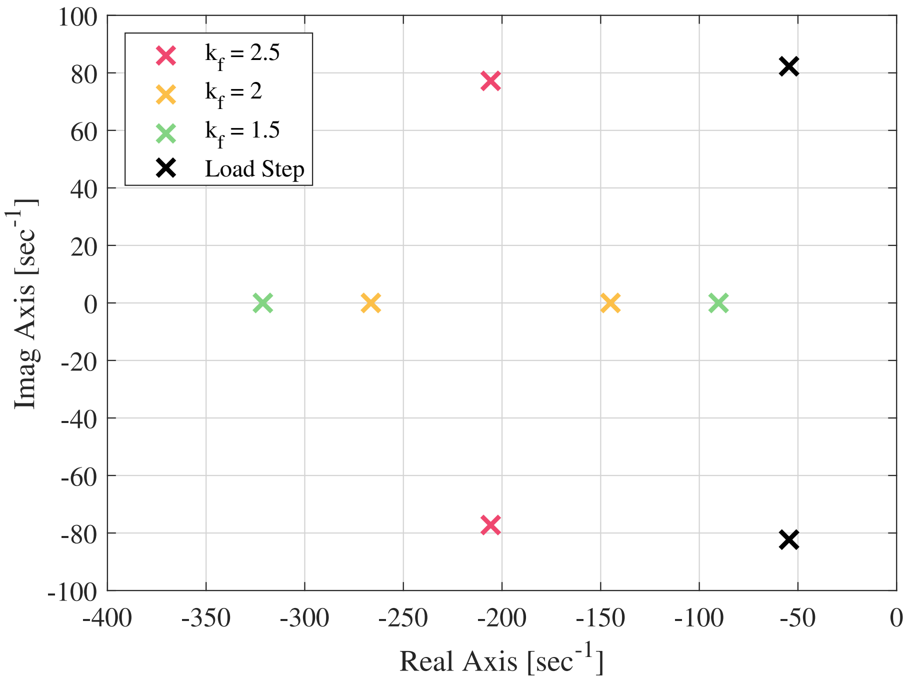

Figure 5.25. Pole-zero map, showing the corresponding placement of the pole for each sweep of k_f.

5.4 LTID-SMO using Power-Sigmoid Function

The LTID-SMO using Power-Sigmoid function (LTID-SMO-PS) are derived based on the aforementioned process given by LTID-SMO-Sat-and Sign, where the torque Equation 3.15 is substituted into the Newtons second law, Equation 3.12, which yields the following equation as:

$$\frac{d\omega_e}{dt} = \frac{K_T N_{pp}}{J} i_q - \frac{B}{J}\omega_e - \frac{N_{pp}}{J} T_L \quad where \quad K_T = \frac{3}{2}\lambda_{mpm} N_{pp} \tag{5.39}$$

By defining the sliding surface as the speed error, $\sigma(t) = \tilde{\omega}_e = \hat{\omega}_e - \omega_e$, the LTID-SMO is obtained and defined as:

$$\frac{d\hat{\omega}_e}{dt} = \frac{K_T N_{pp}}{J} i_q - \frac{B}{J}\hat{\omega}_e - Z_s \quad where \quad Z_s = K_{PS} \cdot \frac{\sigma(t)^\alpha}{|\sigma(t)|^\alpha + \delta} \tag{5.40}$$

The derivative of the speed error is derived by subtracting Equation 5.39 from 5.40, which leaves the derivative of the speed error to be defined as:

$$\frac{d\tilde{\omega}_e}{dt} = \frac{T_L N_{pp}}{J} - \frac{B\tilde{\omega}_e}{J} - Z_s \tag{5.41}$$

Utilizing the steady-state condition, when $\dot{\sigma} = 0$, the estimated load torque is derived from Equation 5.41, and formulated as:

$$\hat{T}_L = \frac{J}{N_{pp}} K_{PS} \cdot \frac{\sigma(t)^\alpha}{|\sigma(t)|^\alpha + \delta} + \frac{B}{N_{pp}}\tilde{\omega}_e \tag{5.42}$$

Where $\frac{B}{N_{pp}}\tilde{\omega}_e \ll \frac{J}{N_{pp}} Z_s$, leaving that the term $\frac{B}{N_{pp}}\tilde{\omega}_e$ is neglected and the estimated load torque may therefore be formulated as:

$$\hat{T}_L = \frac{J}{N_{pp}} K_{PS} \cdot \frac{\sigma(t)^\alpha}{|\sigma(t)|^\alpha + \delta} \tag{5.43}$$

From previously described, the SMO with a signum and saturation function uses a LPF in the estimate the load torque, as $\hat{T}_L$ contains high frequency ripples chatter. The idea behind implementing a Power-Sigmoid function (PS-function) is to obtain an estimated load torque with low chatter without utilizing an LPF. Thereby, from a theoretically point of view, minimizing the phase delay and improve the accuracy of the estimated load torque. Figure 5.26 is showing the observer structure of the above-described LTID-SMO-PS.

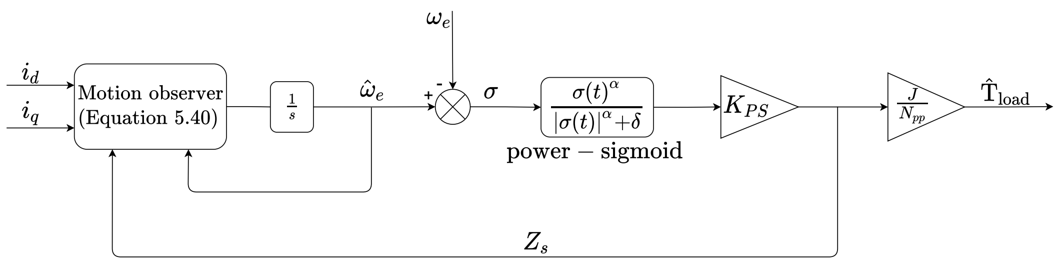

Figure 5.26. A block diagram showing the principles of the LTID-SMO using a PS-function.

5.4.1 Stability analysis

According to Lyapunov stability, the Lyapunov function and its derivative is defined as:

$$V = \frac{1}{2}\sigma^2 \quad and \quad \dot{V} = \sigma \cdot \dot{\sigma} < 0 \tag{5.44}$$

Utilizing that $\dot{\sigma} = \frac{d\tilde{\omega}_e}{dt}$, the derivative of the Lyapunov candidate function may be formulated as:

$$\dot{V} = \sigma \cdot \dot{\sigma} = \left(\frac{N_{pp}}{J}T_L - \frac{B}{J}\sigma - Z_s\right)\sigma \tag{5.45}$$

From Equation 5.45 the following conditions must be applied:

$$\dot{V} = \begin{cases} -\frac{B}{J}\sigma^2 + \left(\frac{N_{pp}}{J}T_L - K_{PS}\cdot\frac{\sigma^\alpha}{|\sigma|^\alpha+\delta}\right)\sigma & , \quad \sigma \geq 0 \\ -\frac{B}{J}\sigma^2 + \left(\frac{N_{pp}}{J}T_L + K_{PS}\cdot\frac{\sigma^\alpha}{|\sigma|^\alpha+\delta}\right)\sigma & , \quad \sigma < 0 \end{cases} \tag{5.46}$$

The output of the Power Sigmoid function is $u_{ps} = \frac{\sigma^\alpha}{|\sigma|^\alpha+\delta}$. Since the characteristic response of the PS-function never reaches an output values of $u_{ps} = \pm 1$, an approximating is made, by defining the output of the PS function to be $u_{ps,max} = 1$ and $u_{ps,min} = -1$, and Equation 5.46 can then be simplified to:

$$\dot{V} = \begin{cases} -\frac{B}{J}\sigma^2 + \left(\frac{N_{pp}}{J}T_L - K_{PS}\right)\sigma & , \quad \sigma \geq 0 \\ -\frac{B}{J}\sigma^2 + \left(\frac{N_{pp}}{J}T_L + K_{PS}\right)\sigma & , \quad \sigma < 0 \end{cases} \tag{5.47}$$

To satisfy the stability condition of Lyapunov function, $\dot{V} < 0$, the sliding mode gain of the LTID-SMO-PS is determined by Equation 5.48.

$$K_{PS} > \frac{N_{pp}T_L}{J} \tag{5.48}$$

To ensure the LTID-SMO-PS is stable with the presented stability condition of Equation 5.48, the threshold value for K_{PS} at $T_{L,max} = 5.8\,[\mathrm{Nm}]$ is calculated, leaving that:

$$K_{PS} > 1856 \quad \text{Threshold value for :} \quad T_{L,max} = 5.8\,[\mathrm{Nm}] \tag{5.49}$$

If chosen the sliding mode gain to be greater than the threshold value, the observer is stable for all cases of $T_L \leq T_{L,max}$. This is further illustrated in Figure 5.27.

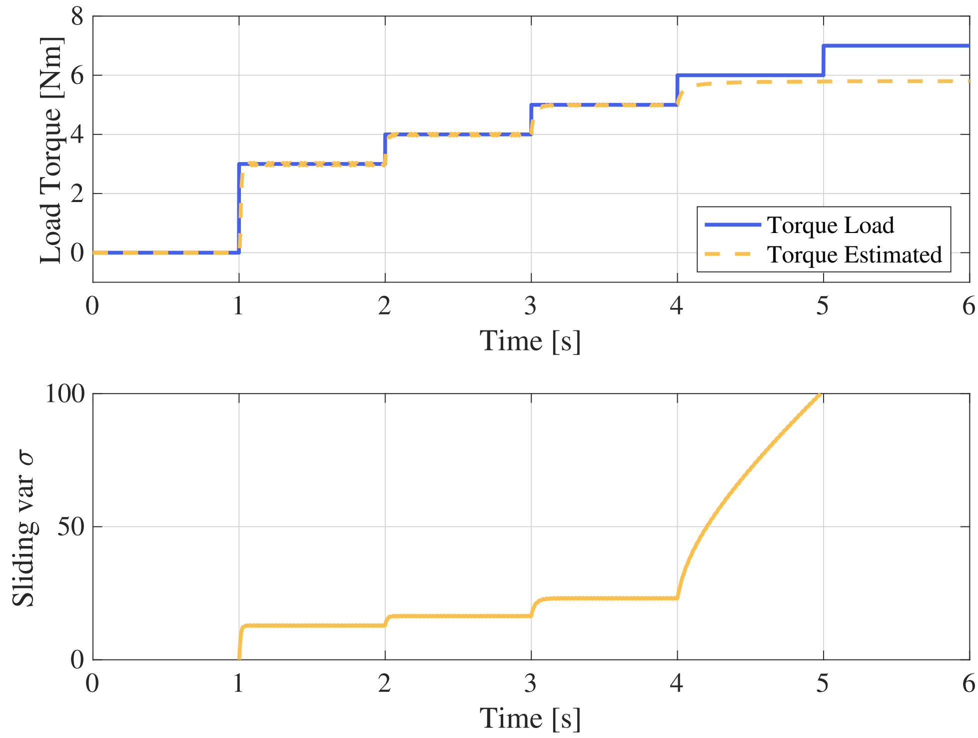

Figure 5.27. Power Sigmoid with $K_{PS} = 1856$, making the system unstable from 5.8 Nm load torque

5.4.2 Impact of parameters of the LTID-SMO using a Power-Sigmoid function

To analyze the impact of the observer gains for the LTID-SMO-PS, a linear model is derived with the output/input of $\frac{\hat{T}_L}{T_L}$. A linear model of the system enables one to describe how the system behaves when each parameter is being varied by investigating the placement of the poles and zeros as previously described.

To derive the linear model, Equation 5.41 and 5.43 are used. Here it should be noted the PS-function is a non-linear function, leaving that Equation 5.41 and 5.43 are firstly linearisared using a first-order Taylor approximation, which yields the following:

$$\Delta\dot{\tilde{\omega}}_e = K_{\dot{\tilde{\omega}}_e\tilde{\omega}_e}\Delta\tilde{\omega}_e + K_{\dot{\tilde{\omega}}_e T_L}\Delta T_L \tag{5.50}$$

$$\Delta\hat{T}_L = K_{\hat{T}_L\tilde{\omega}_e}\Delta\tilde{\omega}_e \tag{5.51}$$

In Equation 5.50 and 5.51 Δ is denoted as the change variable of the systems states. The linearization coefficients is the partial derivative of the state equations and are given as:

$$\begin{aligned}
K_{\dot{\tilde{\omega}}_e\tilde{\omega}_e} &= -\frac{d}{d\,\tilde{\omega}_e}(\dot{\tilde{\omega}}_e) \;= \frac{B}{J} + K_0\,\alpha_0 \cdot \left(\frac{\tilde{\omega}_{e0}^{(\alpha_0-1)}}{\tilde{\omega}_{e0}^{\alpha_0} + \delta_0} - \frac{\tilde{\omega}_{e0}^{(2\alpha_0-1)}}{(\tilde{\omega}_{e0}^{\alpha_0} + \delta_0)^2} \right) \\
K_{\dot{\tilde{\omega}}_e T_L} &= \frac{d}{d\,T_L}(\dot{\tilde{\omega}}_e) = \frac{N_{pp}}{J} \\
K_{\hat{T}_L\tilde{\omega}_e} &= \frac{d}{d\,\tilde{\omega}_e}(\hat{T}_L) \;= K_0\,\alpha_0 \cdot \frac{J}{N_{pp}} \cdot \frac{\tilde{\omega}_{e0}^{(\alpha_0-1)}\delta_0}{(\tilde{\omega}_{e0}^{\alpha_0} + \delta_0)^2}
\end{aligned}$$

If Equation 5.51 is substituted into Equation 5.50 and brought to the Laplace domain, the linear model can be obtained, which yields the following transfer function:

$$G_{sigmoid}(s) = \frac{\hat{T}_L}{T_L} = \frac{K_{\dot{\tilde{\omega}}_e T_L} \cdot K_{\hat{T}_L\tilde{\omega}_e}}{s + K_{\dot{\tilde{\omega}}_e\tilde{\omega}_e}} \tag{5.52}$$

The linearization points, K_0, δ_0 and α_0 is chosen based on the corresponding values for K_{PS}, δ and α used in the non-linear model. $\tilde{\omega}_{e0}$ is the only unknown linearization point and can be solved for in Equation 5.41 by utilizing steady-state condition, with: $\dot{\tilde{\omega}}_e = 0$. Next, the linear model is validated, where the actual load torque of $T_L = 5\,[\text{Nm}]$ from experimental data is used as input to both the linear and non-linear model. For this particular case the non-linear control parameters and the linearization points are given as:

$$\begin{aligned}
&K_{PS} = 3000 \quad , \quad \delta = 1000 \quad , \quad \alpha = 5 \\
&K_0 = 3000 \quad , \quad \delta_0 = 1000 \quad , \quad \alpha_0 = 5 \quad \textit{and} \quad \tilde{\omega}_{e,0} = 12.4
\end{aligned}$$

The validation results are presented in Figure 5.28.

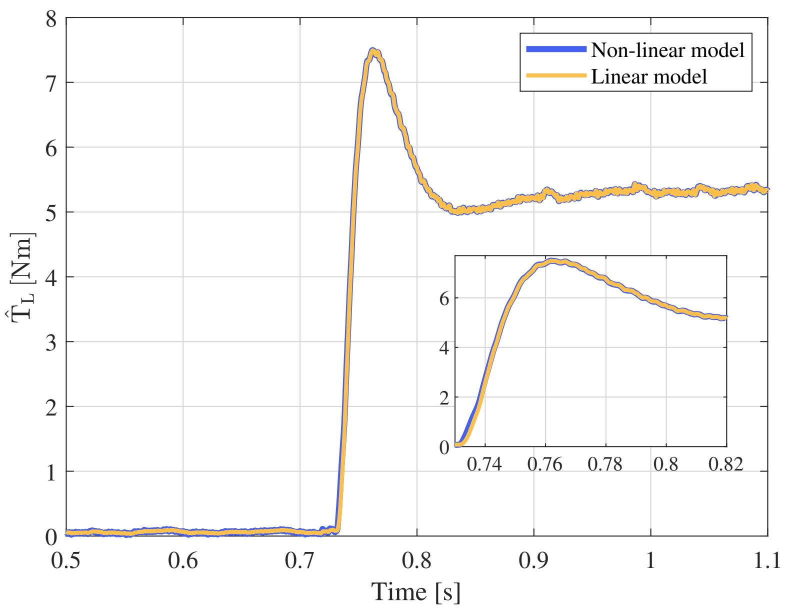

Figure 5.28. Validation results for the linear model of the estimated load torque with the transfer function: $G_{sigmoid}(s)$. In addition, the real load torque, obtained through experiments, are used as input.

From Figure 5.28, it should again be noted that the estimated load torque reaches a steady-state value above the 5 [Nm], caused by a static offset from the Coulomb friction. However, by inspecting the figure it is seen that the linear model resembles the non-linear model and can capture all of the dynamics from the non-linear system. Therefore, the linear model can be further used to analyze the observer gains.

To analyze the impact of the observer gains, the Simulink model is used, as done in Section 5.3.3, where one parameter will be varied. In contrast, the additional parameters are kept constant. When analyzing the dynamical behavior of the parameters, the estimated load torque is investigated in combination with the corresponding speed response, pole-zero map, and the characteristic response of the Power-Sigmoid function (PS-function).

Stipulation of the power constant α

The power constant α is analyzed with $\alpha = 3$, $\alpha = 5$ and $\alpha = 7$. The analysis are presented with Figure 5.29, 5.30 and 5.31. The additional parameters are kept at:

$$\delta = 1500 \quad , \quad K_{PS} = 3000 \tag{5.53}$$

Before analyzing the load torque estimation and the corresponding speed response, the PS-function's characteristic response will be analyzed to understand the behavior of the estimated load torque and speed response for different α values. Figure 5.29 is used to analyze the characteristic response of the PS-function, which shows the correlation between the convergence rate and the placement of the poles.

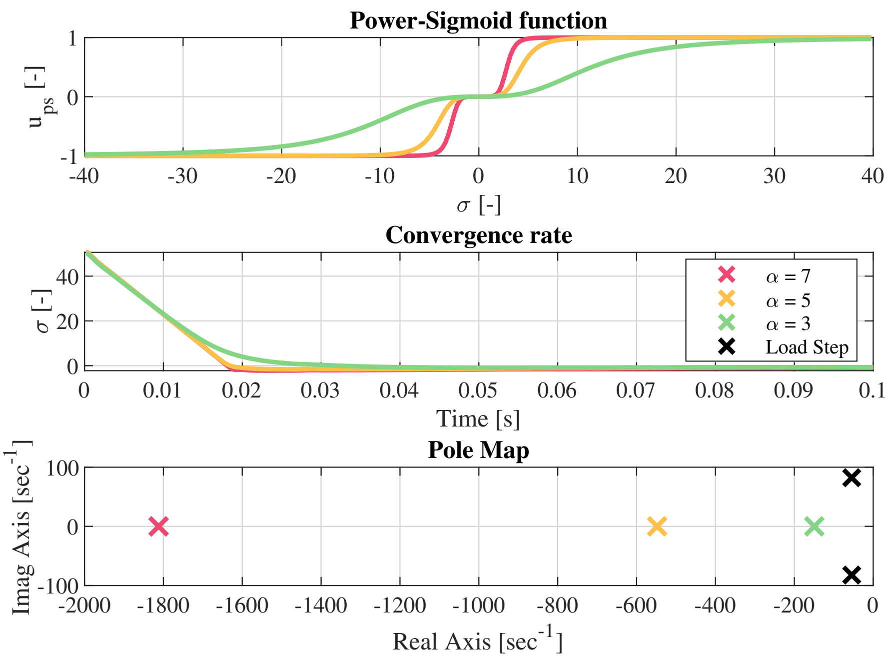

Figure 5.29. The Power-Sigmoid function for a sweep of α and its the corresponding convergence rate and pole-zero map.

Characteristic response of the PS-function

- From the top plot in Figure 5.29, the characteristic response of the PS-function is shown. By investigating the characteristic response for each α value, it should be noted, that having a high α value, will entail a steeper slope, resulting in a faster dynamical response and higher output values, u_{ps}. Having a low α value, will result in the opposite, with a slower dynamical response and lower output values. In addition, by having a low output value, u_{ps}, it would be beneficial to increase the sliding mode gain, K_{PS}, as this will contribute to a faster dynamical response.

Convergence rate to the sliding manifold

- From the middle plot in Figure 5.29, the convergence rate is shown for each α value. The convergence rate illustrates how fast the sliding variable reaches the sliding surface. Here an initial value of $\sigma(0) = 50$ is used to illustrate the convergence rate. The plot can be further used to understand the correlation between the characteristic response of the PS-function and the convergence rate. Where a high α value will results in a faster convergence rate. Therefore if the PS-function has a steeper slope, a faster convergence rate occurs.

Pole-Zero Map for the LTID-SMO

- From the bottom plot in Figure 5.29, the pole-zero map is shown for each α value. The pole-zero map is shown to understand how a faster convergence rate can be achieved when increasing the α value. Here it is seen that when α is increased, the poles move further into the LHP, which indicates the dynamics of the observer become faster.

The main idea for this short analysis of the PS-function is to give an intuitive understanding of how the PS function can be used to design a proper observer regarding convergence rate, placement of the poles, and overall dynamical response of the observer.

Figure 5.30 presents the load torque estimation for the presented α values. Here the effect of a steeper slope in the PS-function is clearly seen. By noticing how an α value of $\alpha = 5$ and $\alpha = 7$ showing the best tracking ability of the actual load torque. However, having a high α value also make the observer more susceptible to chatter. For $\alpha = 3$ the slope gradient in the PS-function is significantly lower, which entail the load torque estimation having a slower dynamical response. This is also be seen in the figure, where the estimation accuracy of the estimated load torque is low and not able to capture all the actual load torque dynamics. Despite the slower tracking ability for $\alpha = 3$, it reduces the chatter notably.

In Figure 5.31 the speed response is shown, where it is clear seen that $\alpha = 5$ and $\alpha = 7$ shows a less *peak-to-peak* value and the fastest recovery time. For $\alpha = 3$ the highest *peak-to-peak* value is shown, which is expected, since the load torque estimation is less accurate for this α value. On top of this, the recovery time is also significantly slower for low α

values than for the higher ones.

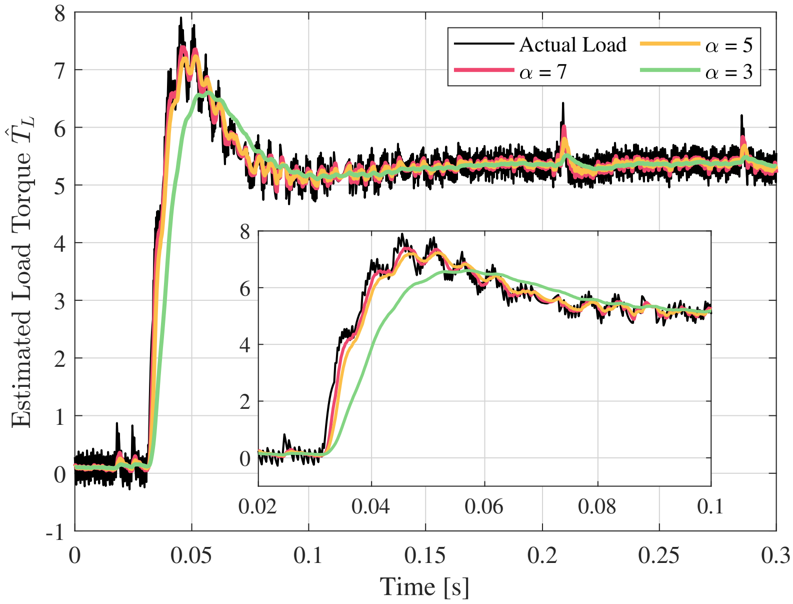

Figure 5.30. The estimated load torques for different α values compared with the actual load torque.

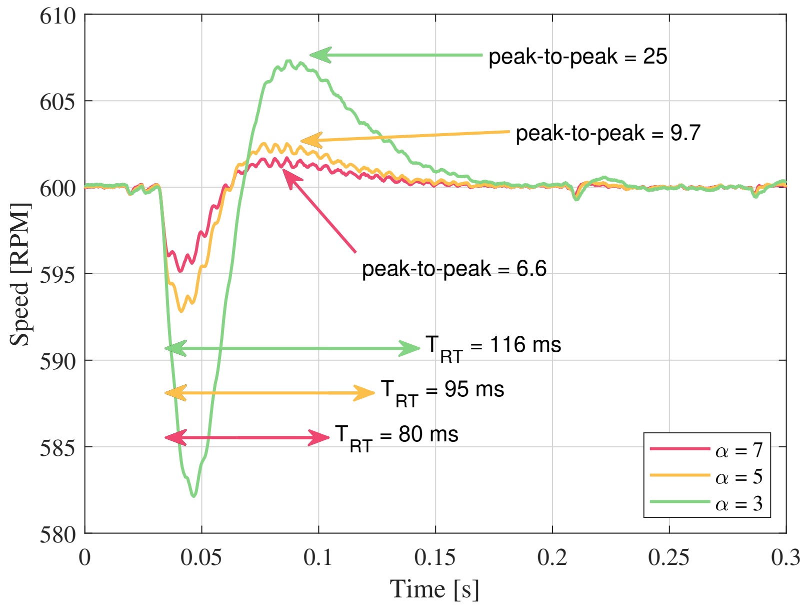

Figure 5.31. A comparison of the speed response for different α values, where the recovery time and peak-to-peak values are shown to better compare each sweep.

Stipulation of δ

When analysing δ, the values of $\delta = 1000$, $\delta = 1500$ and $\delta = 2000$ are used and compared. From the preciously analysis, the value of $\delta = 1000$ in combination with $\alpha = 3$ showed good results regarding chattering reduction. Therefore, the additional parameters are kept constant at:

$$\alpha = 3 \quad , \quad K_{PS} = 3000 \tag{5.54}$$

The characteristic response of the PS-function in combination with a pole-zero map is shown in Figure 5.32. The convergence rate has been omitted for this analysis, as the pole-zero map may show the same conclusion.

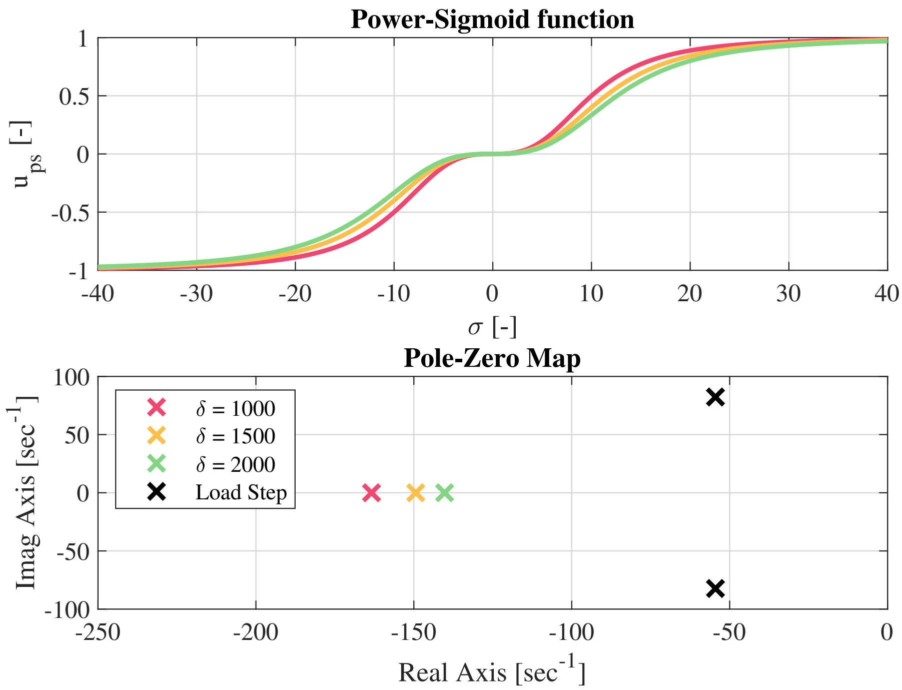

Figure 5.32. The Power-Sigmoid function for a sweep of δ and its the corresponding pole-zero map.

From Figure 5.32, the effect of δ is seen, where it is noted how larger values for δ extend the surface area around the $\sigma \approx 0$, which will entail the SMO is more robust against chattering in areas of low σ values. However, when applying a load step, the sliding variable will increase above $-5 < \sigma_{\delta=2000} \leq 5$, meaning the SMO will be more susceptible to chatter. This may also be seen in the load torque estimation figures, where all figures start with only slightly chattering. In the time after the load step, the chattering increases, due to the sliding variable increases. To better understand this, an analysis is made in Section 5.4.3, showing how the chattering increases when the sliding variable increases. In addition, it may also be noted that higher values for δ will decrease the slope gradient of the PS-function, as can be explained by the poles moving further towards the RHP, entailing a slower dynamical response.

Figure 5.33 presents the load torque estimation for the presented δ values. As seen in the figure, all values of δ almost has same tracking ability and chatter level, however, the trend can conclude that increasing δ, decreases the accuracy of tracking but improves the chatter reduction.

In Figure 5.34 the corresponding speed response is shown. Here it is seen that $\delta = 1000$ shows the smallest *peak-to-peak* value. This is also expected, as this δ value showed slightly better tracking of the actual load torque. For $\delta = 2000$ the highest *peak-to-peak* value occur. From the analysis, it can be concluded that if δ is kept around 1000 to 2000, it does not contribute to any significantly changes for the chosen α.

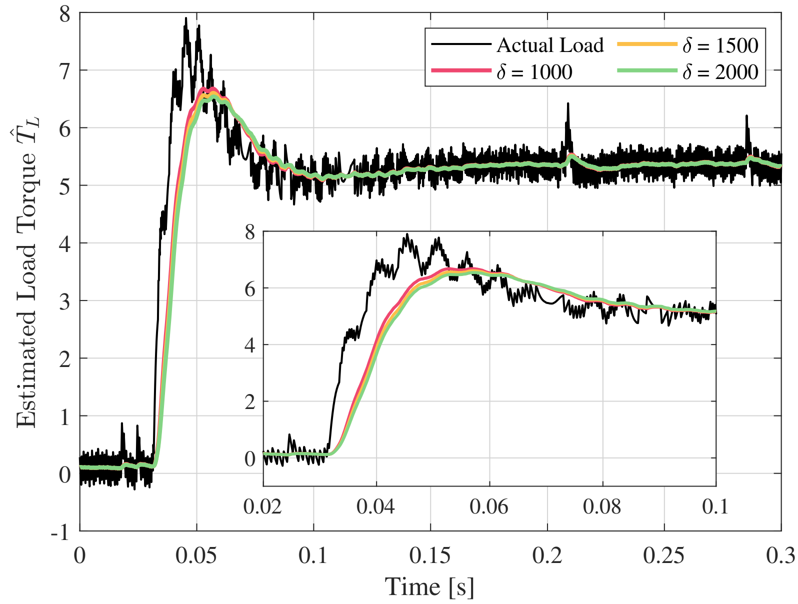

Figure 5.33. The estimated load torques for different δ values compared with the actual load torque.

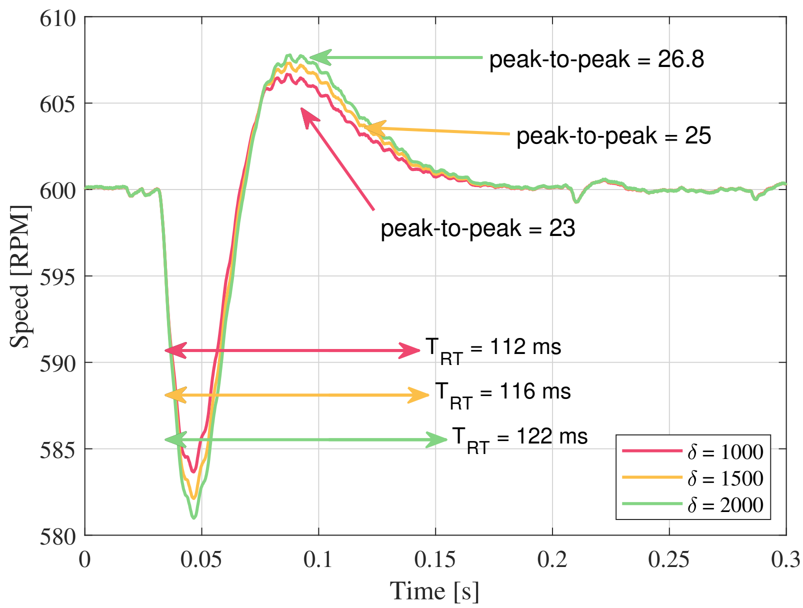

Figure 5.34. A comparison of the speed response for different δ values, where the recovery time and peak-to-peak values are shown to better compare each sweep.

Stipulation of the sliding mode gain K_{PS}

To analyse the impact of the sliding mode gain K_{PS}, the analysis is made with $K_{PS} = 2000$, $K_{PS} = 2560$ and $K_{PS} = 3000$. The additional parameters are kept constant at:

$$\alpha = 3 \quad , \quad \delta = 1500 \tag{5.55}$$

The characteristic response of the PS-function in combination with a pole-zero map is shown in Figure 5.35. The sliding mode gain acts purely on the output of the PS-function and can therefore not alter the characteristic response. Therefore only one PS-function is shown with the parameters given by Equation 5.55.

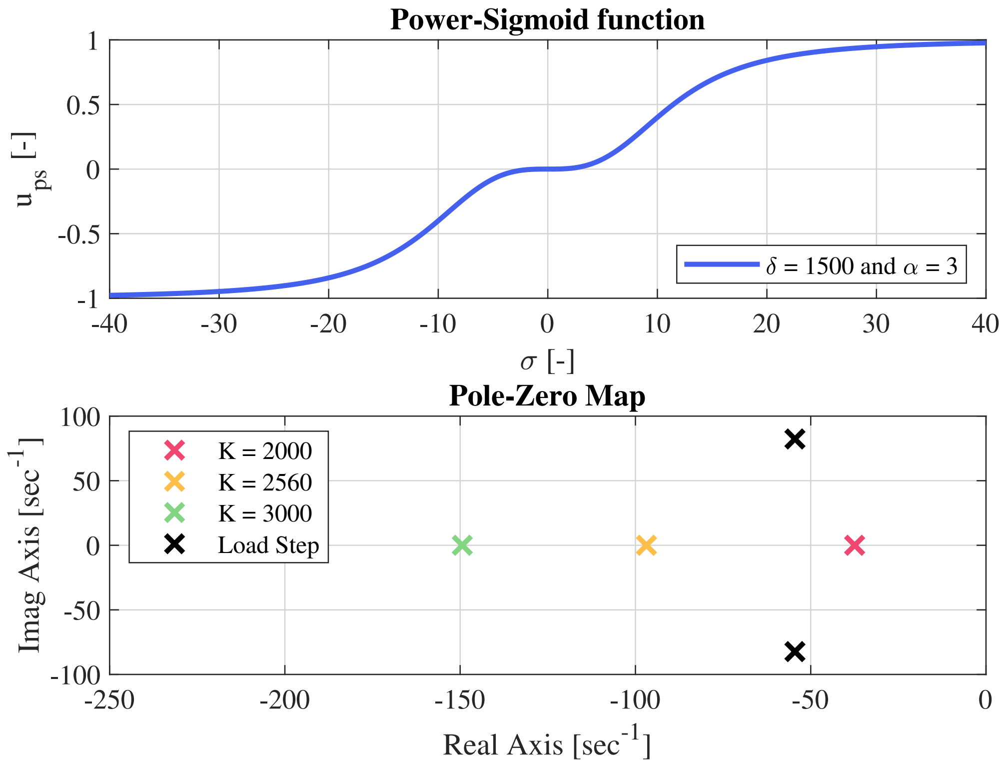

Figure 5.35. The PS-function shown for the parameters given by Equation 5.55 and its corresponding pole-zero map.

If increasing the sliding mode gain, the accuracy of load torque estimation can be improved. The reason for the improved estimation accuracy should be found by investigating the pole-zero map in Figure 5.35, where it is seen that a high sliding mode gain will cause the poles to move further into the LHP, which in return makes the SMO's dynamical response faster. However, if decreasing the sliding mode gain the pole will move towards to imaginary axis and eventually become the dominating pole, which will leave the dynamical response of the LTID-SMO being too damped, and not able to estimate the actual load torque.

Further, the sliding mode gain should not be chosen to be below $K_{PS} = 2560$ as this will cause the SMO to become unstable due to the transient part of the load torque, reaching a maximum value of $T_{L,transient} \approx 8\,[\text{Nm}]$. In Figure 5.36, the load torque estimation is shown. It shows as described, that having a K_{PS} of 2000 will limit the torque estimation to be lower than the actual torque input. A gain K_{PS} of 2560 and 3000, both gives better tracking performance, but the latter is the best. This is also seen in the speed response from Figure 5.37, where $K_{PS} = 3000$ shows the lowest *peak-to-peak* value. However, as chattering causes the SMO to decrease in performance, a very high sliding mode gain K_{PS} can make the observer to become unstable due to chatter issues. In this case a sliding mode gain of $K_{PS} = 3000$ is performing well.

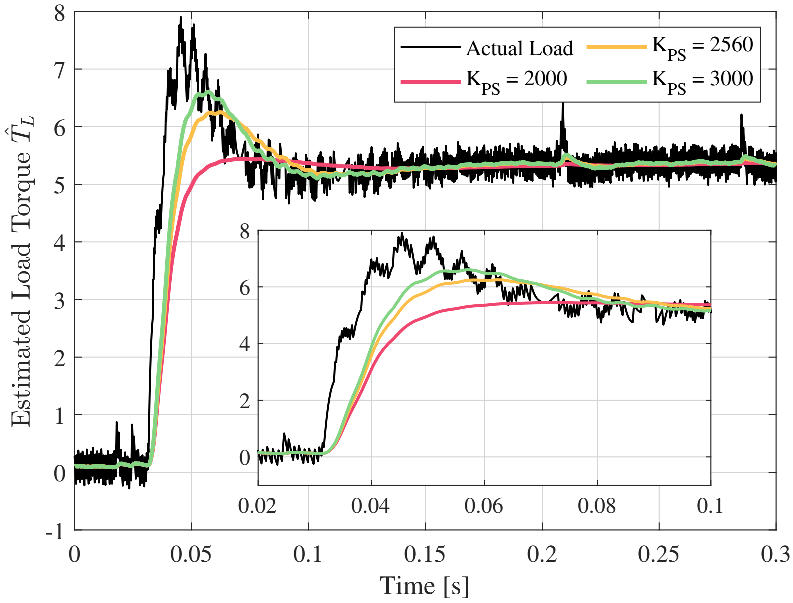

Figure 5.36. The estimated load torques for different sliding mode gains compared with the actual load torque.

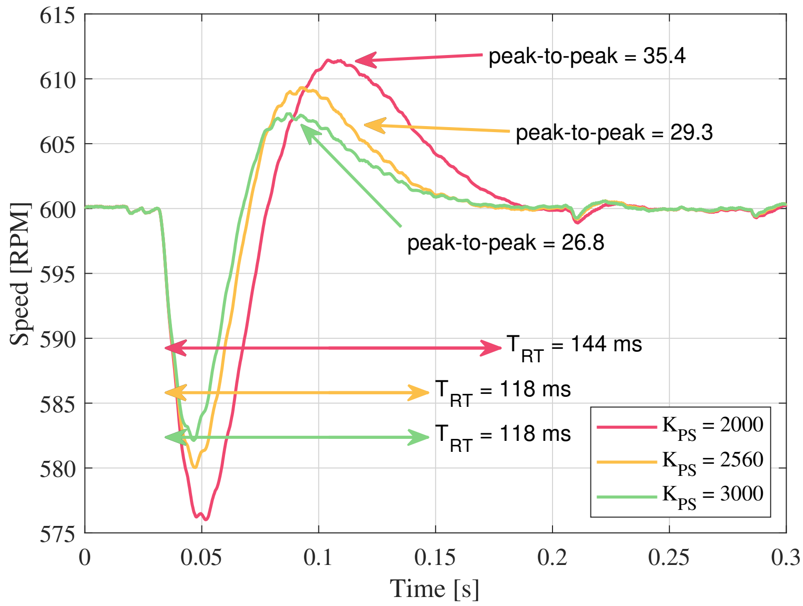

Figure 5.37. A comparison of the speed response for different sliding mode gains, where the recovery time and peak-to-peak values are shown to better compare each sweep.

From the above analysis for α, δ and K_{PS} the final parameters are given as follows:

$$\alpha = 3 \quad , \quad \delta = 1500 \quad , \quad K_{PS} = 3000 \tag{5.56}$$

5.4.3 Chatter attenuation

Throughout section 5.4.2 the designed PS-function showed good results for attenuating chatter for low σ values, occurring at no load conditions. However, when a load is applied, the σ value increases and the PS-function is no longer able to attenuate the chattering as well. This may further be seen in Figure 5.38, where the chattering increases when a load torque is applied.

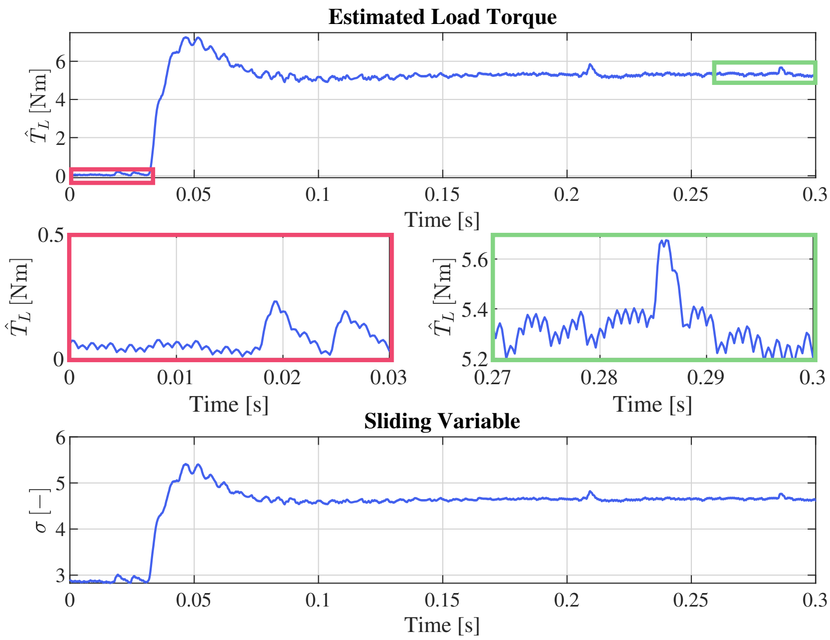

Figure 5.38. Chatter analysis for the estimated load torque, with the control parameters as: $K_{PS} = 3000\,, \delta = 1500\,, \alpha = 3$

From Figure 5.38 it is clearly seen that the sliding variable increases when the load torque increases. Further, it should be noted that the chattering is only slightly present during no load condition. After the load step is applied the chattering increases significantly. The reason for the increased chattering, should be found by inspecting the characteristic response of the PS-functions, which can be seen in Figure 5.39.

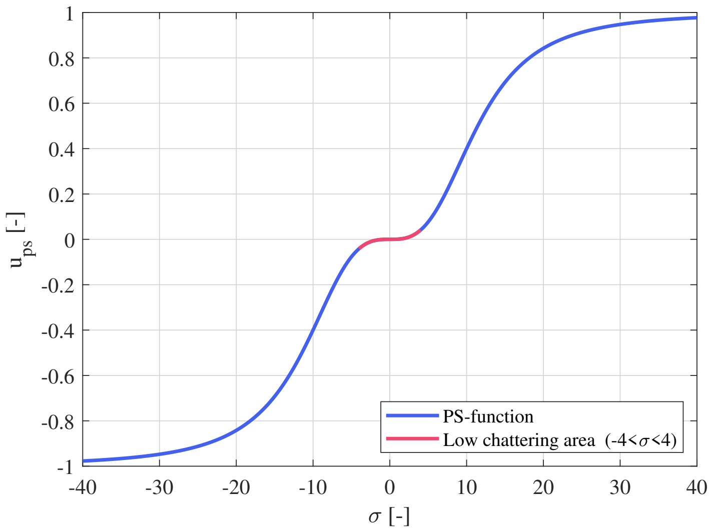

Figure 5.39. Switching surface, showing low chatter area in red and high chattering area in blue. The parameters: $\delta = 1500\,, \alpha = 3$ are used.

From Figure 5.39 the low chattering area is highlighted with red. If operating above or below the highlighted area the sliding variable is placed in the high chattering area. Therefore, to benefit from the design of the PS-function, the sliding variable should during steady-state be driven towards zero (the low chattering area). This would make the output from the switching function close to zero and thereby reducing chatter even at higher load torque.

To do this, the SMO gain K_{PS} is replaced with a PI controller to allow for fast transient response while in the process drive the sliding variable towards zero, due to the characteristic of the integrator.

LTID-SMO-PS Using a PI Controller

In Figure 5.40, the block diagram shows the principles of the observer structure using a PI controller. Here it should be noted that the only difference from the LTID-SMO-PS with K_{PS} (LTID-SMO-PS-$\mathrm{K_{PS}}$) is the replacement of K_{PS} with a PI controller. Therefore the fundamental equations for deriving the LTID-SMO-PS with a PI controller (LTID-SMO-PS-PI) remain the same as for LTID-SMO-PS-$\mathrm{K_{PS}}$. However, as the controller output has changed, a new stability analysis is made and presented in Appendix B.

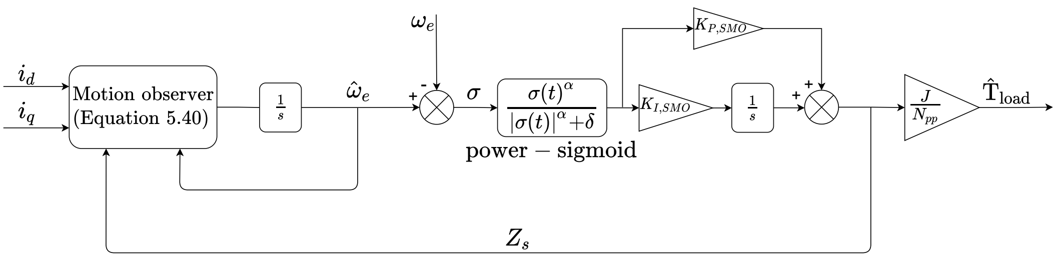

Figure 5.40. Diagram of the LTID-SMO-PS-PI

From the stability analysis in Appendix B the observer gain $K_{P,SMO}$ is determined as:

$$K_{P,smo} = \frac{N_{pp} T_{L,transient}}{J} \left(1 + \frac{\delta}{\sigma^a}\right) \approx 3000 \tag{5.57}$$

The observer gain $K_{P,SMO}$ is calculated with the parameters given by Equation 5.58 where the load torque of $T_{L,transient} = 8\,[\text{Nm}]$ is used to ensure a stable SMO during the transient response.

$$\alpha = 3 \quad , \quad \delta = 1500 \quad , \quad \sigma = 20 \tag{5.58}$$

The sliding variable is chosen to $\sigma = 20$, and relates to what the sliding variable reaches, when the load torque is at $T_{L,transient}$ and under the special condition that $K_{I,smo} \cdot t = 0$. The observer gain $K_{I,SMO}$ is a tuned value to satisfy a fast reduction of the sliding variable and is determined to be:

$$K_{I,SMO} = 15000 \tag{5.59}$$

Using the above-described observer parameters, a comparison of the sliding variable is made for the two LTID-SMO-PS methods where a load torque of $T_L = 5\,[\text{Nm}]$ is applied. The results are presented in Figure 5.41.

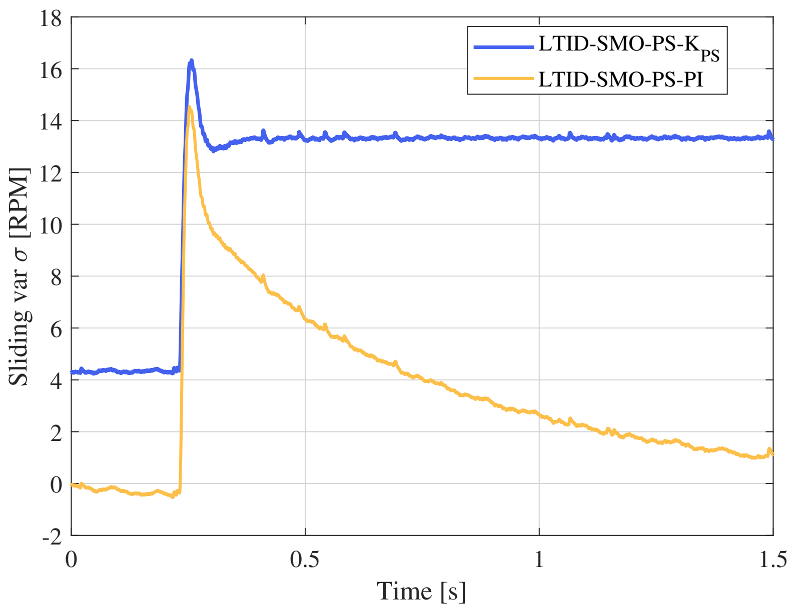

Figure 5.41. The sliding variable σ seen decreasing after a load step

From Figure 5.41, it is seen that the LTID-SMO-PS-PI drives the sliding variable, σ, towards zero. Whereas the sliding variable for LTID-SMO-PS-K_{PS} remains unchanged during steady-state. As previously described, driving the sliding variable towards zero will entail that the sliding variable eventually enters the low chattering area, which will reduce the chattering during steady-state. The effect of the PI controller is clearly seen by inspecting the estimated load torque in Figure 5.42 and the corresponding steady-state response in 5.43.

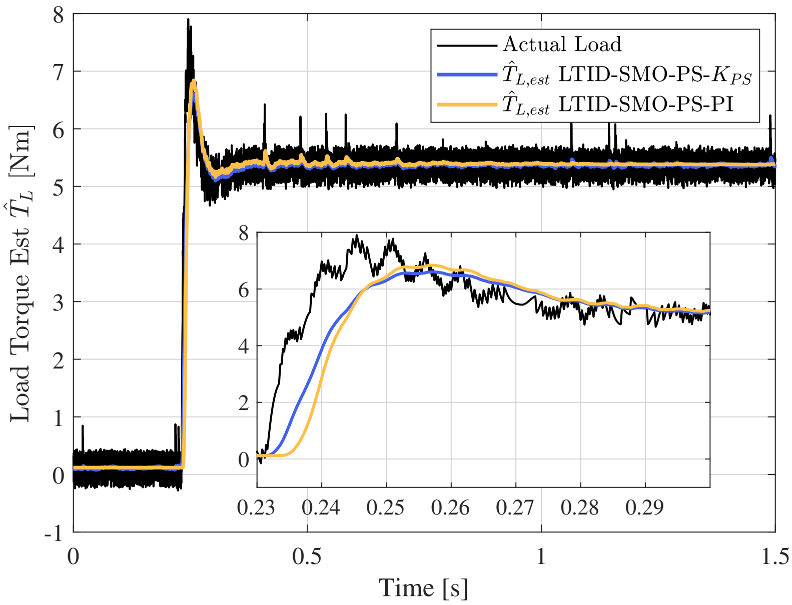

Figure 5.42. Load torque estimation at 600 RPM and 0-5 Nm load step

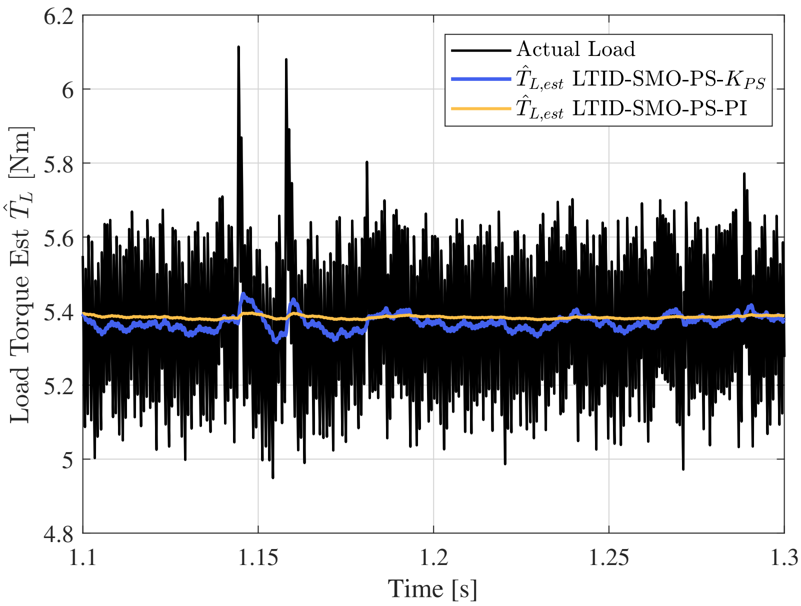

Figure 5.43. The reduced chatter for the load torque estimation 0.75s after the load step, running at 600 RPM and 0-5 Nm load step

From Figure 5.42, it is seen that the LTID-SMO-PS-PI has a similar transient response as LTID-SMO-PS-K_{PS} and can estimate the actual load torque. However, some initial delay is seen during the beginning of the load step. This delay causes the estimation accuracy to decrease and may affect the overall performance of the speed response. The initial delay can be explained by the sliding variable being approximately zero before the load step. Therefore, only the integrator contributes to estimate the load torque.

From Figure 5.43, the steady-state response of the estimated load torque is presented.

Here, it is seen that the chattering is reduced to almost nonexistent by driving the sliding variable towards zero.

To conclude on the overall performance for the LTID-SMO-PS-PI, the speed response is shown for both LTID-SMO-PS methods, showing the peak-to-peak value and recovery time. The results are presented in Figure 5.44.

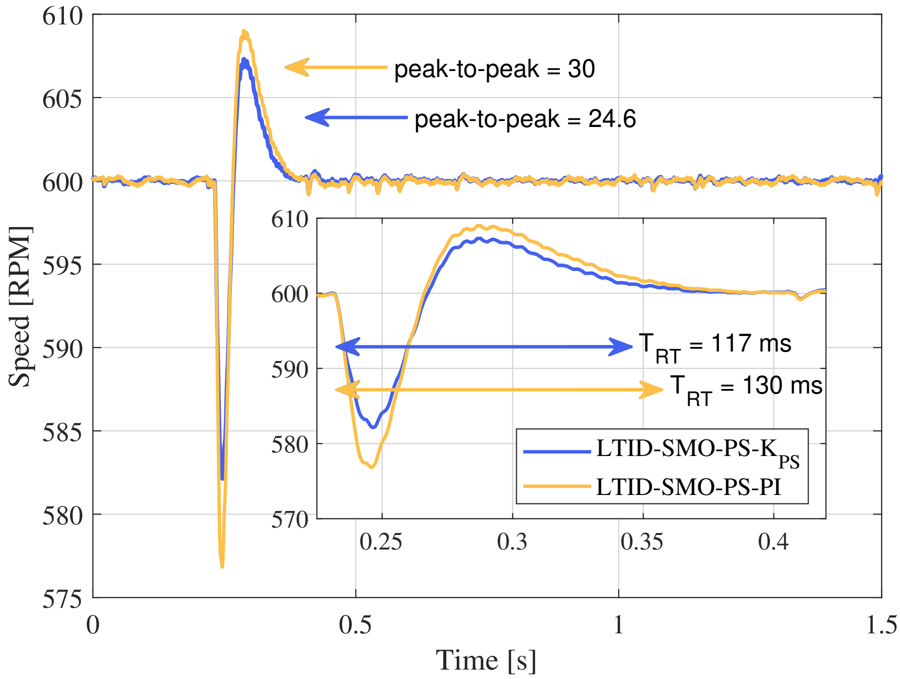

Figure 5.44. Speed response at load step using the load torque estimation as feed forward compensation

From Figure 5.44, the LTID-SMO-PS-PI shows a good ability to reduce the speed error. However, like the previous observers, an overshoot happens. For the LTID-SMO-PS-PI, the peak-to-peak value is 30 [RPM], and the total recovery time is 130 [ms], which leaves the LTID-SMO-PS-PI to perform slightly worse than the LTID-SMO-PS-K_{PS}, which the initial delay can explain at the beginning of the estimated load torque.

5.5 Improving Recovery Time

It is clear from the previous sections 5.2, 5.3 and 5.4, that the recovery time often isn't improved by much when using the LTID-SMOs. Ideally, when the SMOs are used the effect from load change should be mitigated as much as possible, reducing both speed error and recovery time.
When a load step is applied, a speed error appears. The SMO is used to remove this speed error as fast as possible. The estimated load torque from the SMO is converted to a current, $\hat{i_q}^*$, which is added to the reference i_q^* current before the current PI controller. There will always be a slight delay between the actual load step and the estimated load

step, this means perfect estimation is not possible.
Simultaneously to the load step estimation, the speed PI controller sees a speed error which it tries to correct by changing the output current i_q^*. However, with both the Speed PI controller and the feed forward compensation, an over correction of the speed occurs due to too much produced torque. This means further overshoot in the speed response, resulting in a slower recovery time. The integrator from the speed PI controller contains information of the past, and the output is therefore not only for the present but also the sum of all the previous integration's. Resetting the integrator can therefore be used to reduce the contribution the speed PI controller have during a load step and allow more of the control effort to come from the observer output. By doing this correctly, the overshoot can be removed and thereby avoid the slow decrease in speed error.

Reset Speed PI Integrator

The reset option can either be on or off. It is off, when a load change have not been detected. This ensures that the integrator is not reset accidentally if small torque ripples are occurring. It is also off during reference speed changes as to allow the controller to always work when changing the reference speed.

When a load and speed change is detected, it triggers a timer for x amount of time, after which the reset is activated. The time delay from detection to the reset is activated, is to wait for the speed response to be back around the speed reference. This can be seen in Figure 5.45 where the red line corresponds to the detection point and the yellow line is the reset point. If the timer is increased the yellow line moves further to the right and the reset occurs later. The initial condition after reset is set to the output from the integrator to be the same as before the detection point.

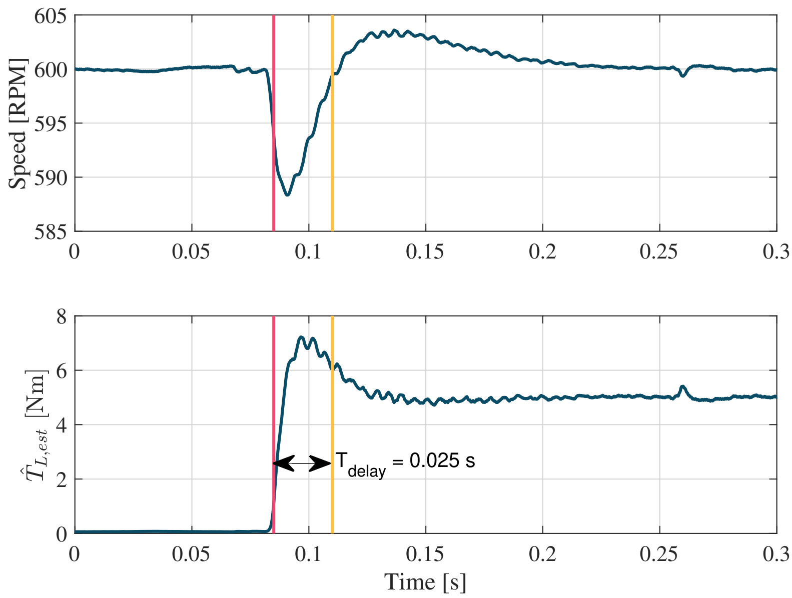

Figure 5.45. Speed and torque response with no reset of integrator in speed PI controller.

From Figure 5.46 it can seen that in this case, having the timer for the reset wait for 0.025 [s] has reduced the recovery time from 113 [ms] to 44 [ms]. The initial condition is 0.14 in this case.

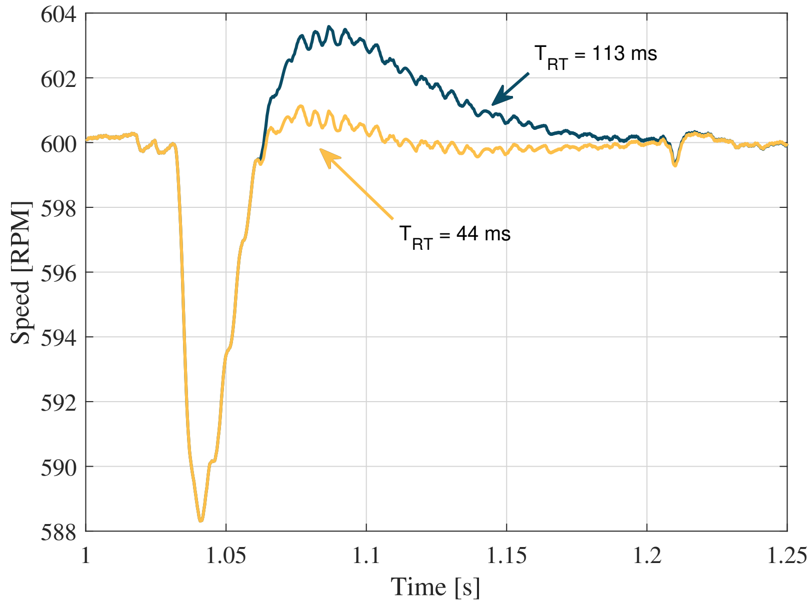

Figure 5.46. Speed response under a load with a reset period of 0.025 s for the integrator

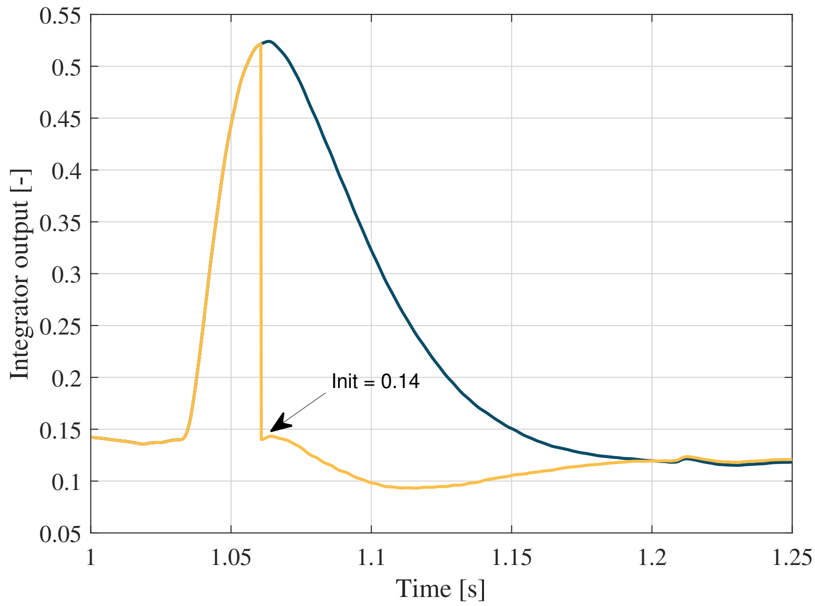

Figure 5.47. Output from the integrator in speed PI controller, with an initial condition is 0.14.

5.6 Simulation Results and Comparison

This section compares the simulation results for the different LTID-SMO methods. The observer gains obtained through Section 5.2 to 5.4 is implemented into its respectively

LTID-SMO method, where the result of these is shown. Finally, some performance criteria are used to compare each LTID-SMO method. The performance criteria are as follows:

- Overshoot in the speed response.
- Recovery time for the speed response.
- Error between the estimated and real load torque
- Chattering in estimated load torque.

The above-described criteria, compare each method more accurately and conclude pros and cons of each LTID-SMO strategy.

The speed response and the estimated load torque were investigated to compare the different SMOs. Each analysis presented, is made with a fixed load step of $T_L = 5\,[\text{Nm}]$. The reference speed will be at low and higher speed to show how each method performs when the motor is running at different reference speeds.

The structure of the analysis consists of three parts. The first part is the analysis of the resulting speed response. The second part of the analysis presents the dynamical response of the estimated load torque and explains the speed response. The last part summarizes the above-described performance criteria for each LTID-SMO method.

Analysis of the speed response:
Figure 5.48 and 5.49 is showing the comparison of the SMOs, with a reference speed of $n_{ref} = 600\,[\text{RPM}]$ and $n_{ref} = 1800\,[\text{RPM}]$. From Figure 5.48, it is clear that using LTID-SMO-Sat function, is best at reducing the speed error under a load step, achieving 18 [RPM] peak-to-peak, however, the recovery time longer than the other methods at 60 [ms]. The LTID-SMO-Sign, have the largest speed error, peak-to-peak of 23 [RPM]. Its recovery time is only 43 [ms]. The LTID-SMO-PS-K_{PS} with a proportional gain, has a recovery time of 43 [ms], same as LTID-SMO-Sign, but has a lower speed error of 18. [RPM]. The final observer is LTID-SMO-PS-PI using a PI controller also having a recovery time of 43 [ms], but its speed error is 21 [RPM] slightly worse than LTID-SMO-PS-K_{PS}. However, but still being better than the conventional LTID-SMO-Sign. From Figure 5.52, the observers are experiencing a 5 [Nm] load step at 1800 [RPM]. The results are similar what was seen when running at 600 [RPM], as LTID-SMO-Sat was having the lowest peak-to-peak error but also longest recovery time. LTID-SMO-Sign has slightly longer recovery time than LTID-SMO-PS with and without PI, and has the highest peak to peak error of 20 [RPM].

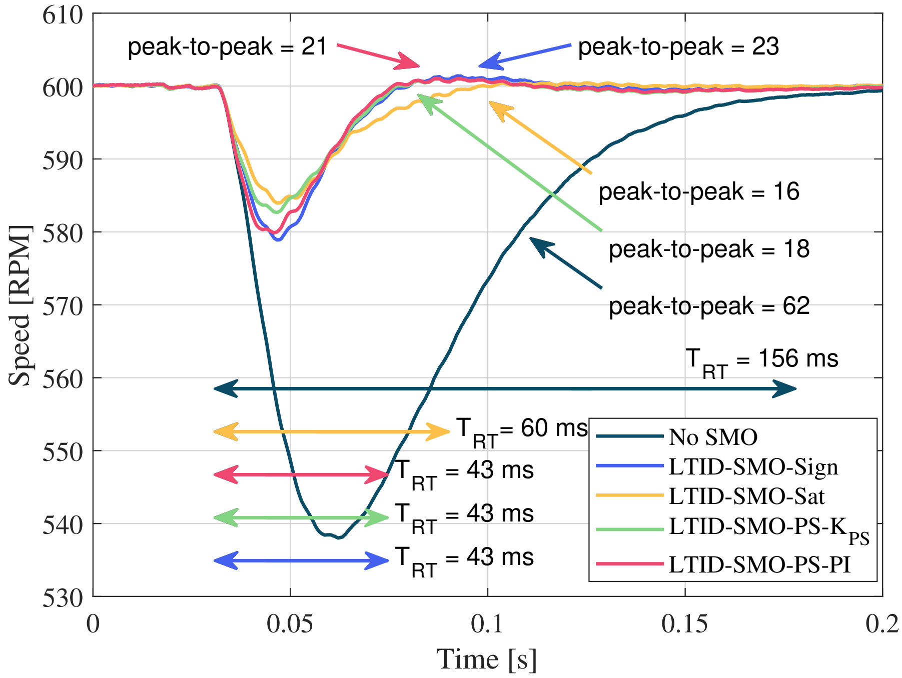

Figure 5.48. Resulting speed response with a reference speed of $n_{ref} = 600\,[\mathrm{RPM}]$.

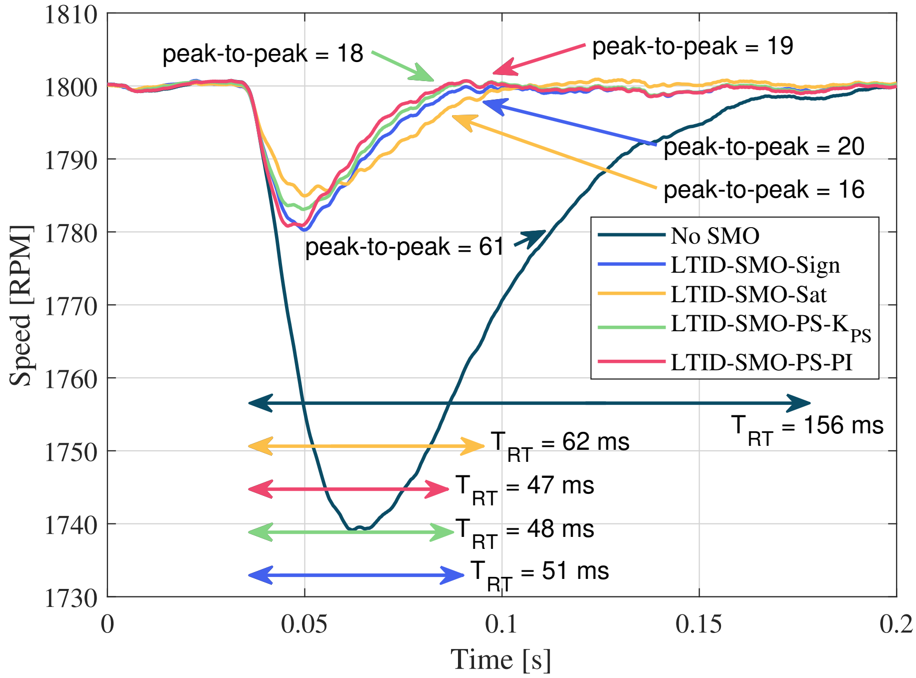

Figure 5.49. Resulting speed response with a reference speed of $n_{ref} = 1800\,[\mathrm{RPM}]$.

Analysis of the dynamical response for the estimated load torque:
Figure 5.50 and 5.51 showing the comparison of the estimated load torque at 600 RPM, with the estimation error, e_{T_L}, between the actual and estimated load torque being shown in the bottom subplot of each figure. The LTID-SMO-Sign clearly shows the most chatter

in the estimated load torque, with its error is peaking at 3.5 [Nm] in the transient part and having a RMSE of 0.18 [Nm]. During the steady-state figure 5.51, LTID-SMO-Sign estimates between 5.1 to 5.6 [Nm], with multiple peaks reaching down to 4.7 [Nm]. The LTID-SMO-Sat showing the fastest transient response during the load step, resulting in the estimation error only reaches up to 2.6 [Nm] its RMSE torque error estimation is however the highest at 0.19 [Nm]. Its chatter level is low, even lower than the ripples seen in the actual load torque. This also means the error during the steady-state area is low, only between -0.25 to 0.25 [Nm]. LTID-SMO-PS-$\mathrm{K_{PS}}$ has slightly better load torque error as the LTID-SMO-Sign, and with much less chatter in the estimation. This is especially clear in the steady-state area where the chatter level is on a par with the LTID-SMO-Sat. Lastly, LTID-SMO-PS-PI shows largest estimation error of 3.9 [Nm] but best RMSE torque estimation error of 0.1 [Nm]. The large error happens as the initial increase is slower than the other three SMOs, however, it quickly reduces the error to catch the other three SMOs. Its chatter level is during the transient part, on a similar level as LTID-SMO-Sat and LTID-SMO-PS-$\mathrm{K_{PS}}$. However, in the steady-state area, LTID-SMO-PS-PI shows its ability to reduce chatter to near zero.

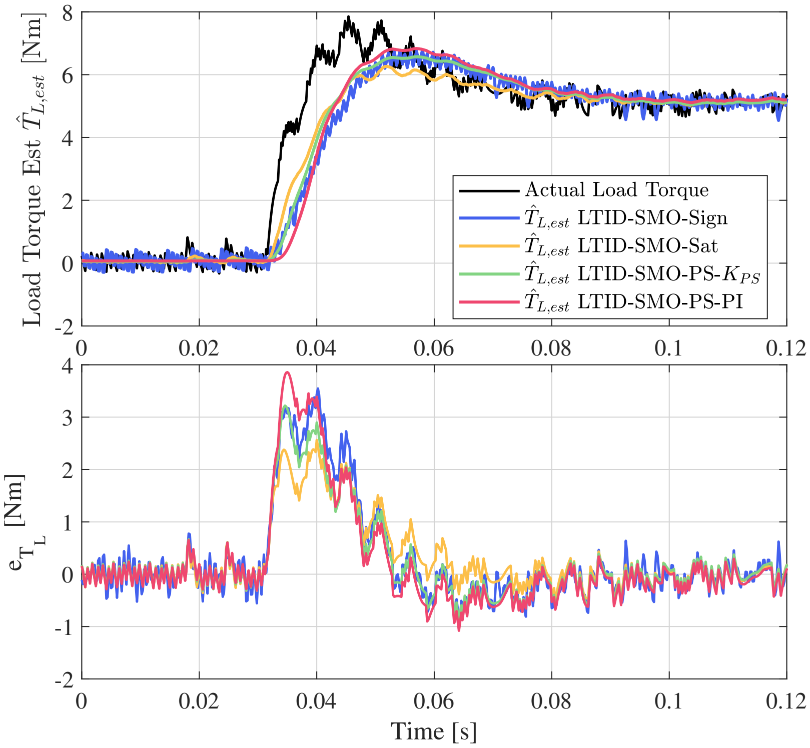

Figure 5.50. Top figure showing the actual load torque in comparison to the estimated load torque for each LTID-SMO method. Bottom figure showing the resulting error between the estimated and actual load torque. The figure is made with reference speed of $n_{ref} = 600$ [RPM].

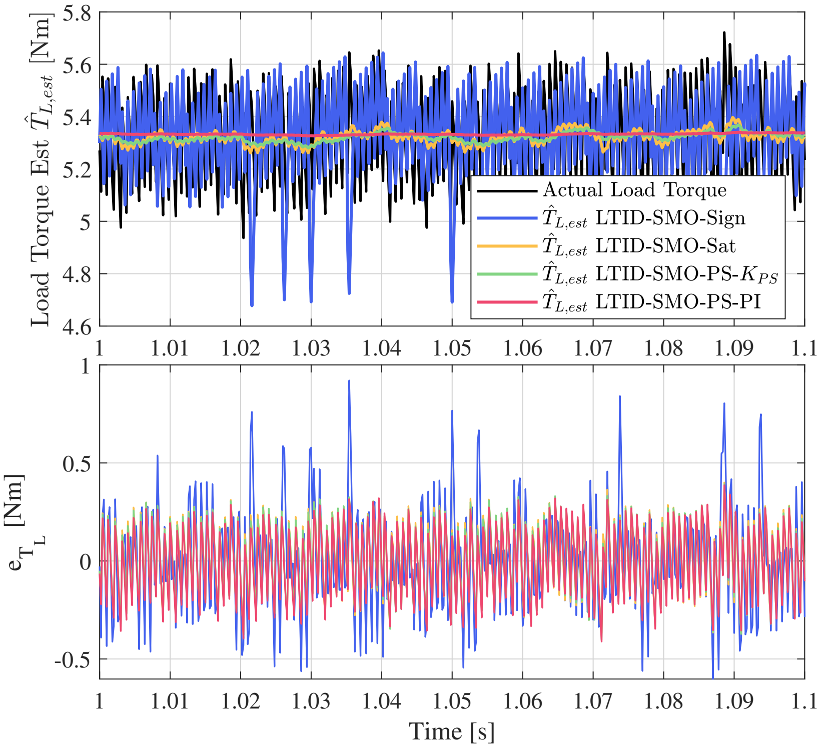

Figure 5.51. The steady state load torque estimation of 5 [Nm] and the load torque estimation error running at speed of 600 [RPM].

The Figures 5.52 and 5.53 is showing the estimated load torque at 1800 [RPM]. The SMOs performances are the showing similar performance as seen at 600 [RPM]. The most noticeable difference can be seen in the last figure showing the steady-state part, it can be seen from the actual load torque that there is a sine wave with a period of around 0.03 [s] which corresponds to about 33 [Hz]. This sine wave is related to the mechanical rotor speed at, this is further discussed in Chapter 7 Section 7.3.

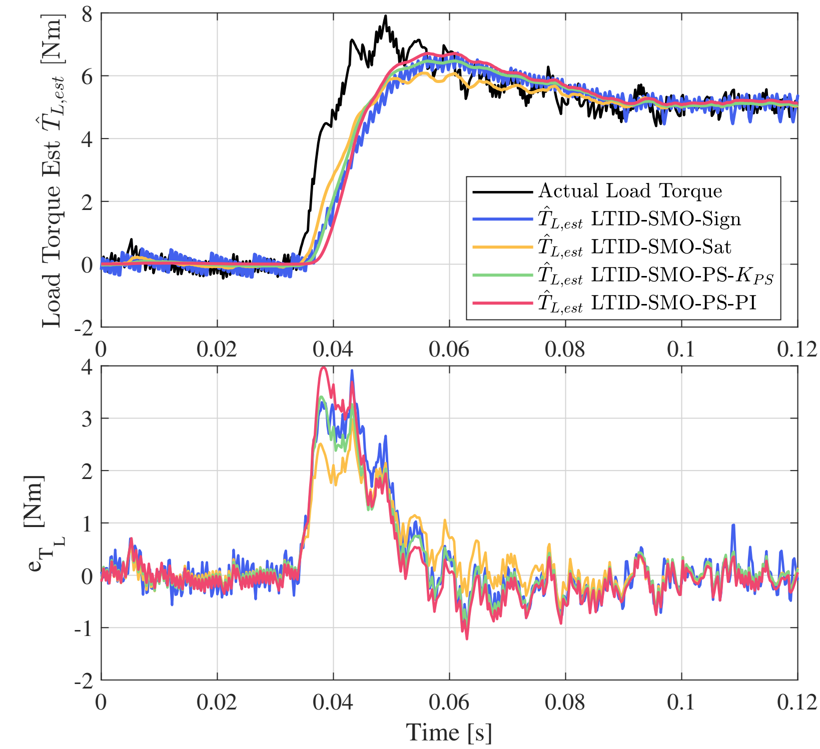

Figure 5.52. Top figure showing the actual load torque in comparison to the estimated load torque for each LTID-SMO method. Bottom figure showing the resulting error between the estimated and actual load torque. The figure is made with reference speed of $n_{ref} = 1800$ [RPM].

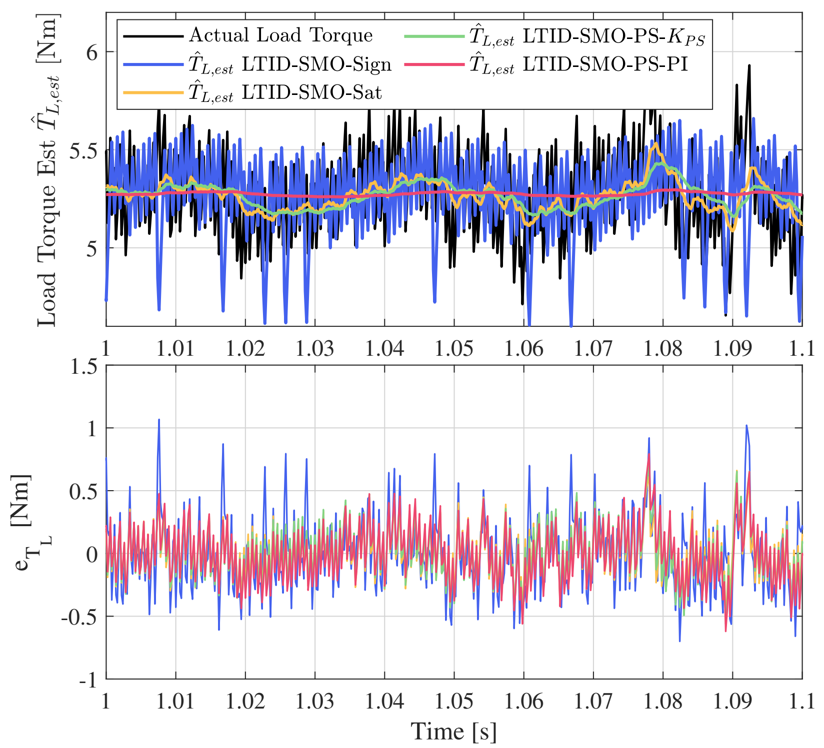

Figure 5.53. The steady state load torque estimation of 5 [Nm] and the load torque estimation error running at speed of 1800 [RPM]

Summary of the analysis:

To conclude on the simulation, the above-described performance criteria are shown for each LTID-SMO method. The final results are presented in the two tables next. The RMSE and Max e_{L_T} is calculated based on 0.2 seconds of data starting at 0 seconds on Figure 5.50 and 5.52.

LTID-SMO	RMSE Torque	Max e_{L_T}	Recovery Time	Peak-to-Peak
Sign	0.18 Nm	3.5 Nm	43 ms	23 RPM
Sat	0.19 Nm	2.6 Nm	60 ms	16 RPM
PS-K_{PS}	0.15 Nm	3.2 Nm	43 ms	18 RPM
PS-PI	0.1 Nm	3.9 Nm	43 ms	21 RPM
No SMO	-	-	156 ms	62 RPM

Table 5.2. Performance marks for 5 Nm load step at 600 RPM

LTID-SMO	RMSE Torque	Max e_{L_T}	Recovery Time	Peak-to-Peak
Sign	0.18 Nm	3.9 Nm	51 ms	20 RPM
Sat	0.19 Nm	3 Nm	62 ms	16 RPM
PS-K_{PS}	0.15 Nm	3.4 Nm	48 ms	18 RPM
PS-PI	0.1 Nm	4 Nm	47 ms	19 RPM
No SMO	-	-	156 ms	61 RPM

Table 5.3. Performance marks for 5 Nm load step at 1800 RPM

Experimental Test and Tuning 6

In the following chapter, the experimental data for the four different LTID-SMO methods, described in Chapter 5, are presented. To describe the performance for each LTID-SMO method, the recovery time, load torque estimation error, speed error, and RMS errors are used to conclude the performance during each analysis. The following chapter is structured by first showing the control parameters used in each LTID-SMO method. Then, the results from the experiments are presented in a table, describing the above-formulated performance parameters. The experimental graphs will be thoroughly described and analyzed. Finally, the comparison of the experimental test conducted for each LTID-SMO method will be presented in Chapter 7.

6.1 Experimental Test without LTID-SMO

To create benchmark values for comparing the performance of the LTID-SMO methods, two tests were conducted, one for 600 [RPM] and one for 1800 [RPM] without the LTID-SMO connected to the FOC. A load torque is applied for 1 [Nm] and 5 [Nm] during each test. The speed, n_{meas}, is measured during each test with the load torque, T_L, being calculated based on the approach described in Section 3.2. The experimental data are presented in Figures 6.1 and 6.2. The results of the two tests are given in Tables 6.2 and 6.3. These performance parameters will be used as benchmark values for the drive system when utilizing the LTID-SMO methods connected to the FOC. The RMSE is calculated by averaging the errors caused by the load step at 1 [Nm] and 5 [Nm]:

$$RMSE = \frac{RMSE_{1[\text{Nm}]} + RMSE_{5[\text{Nm}]}}{2} \tag{6.1}$$

Where the $RMSE_{1[\text{Nm}]}$ and $RMSE_{5[\text{Nm}]}$ is calculated using data for 0.5 [s] before and after the load step.

To determine the recovery time, error bands are used as described in Section 2.3.

Parameter	Value	Unit
RMSE Speed	7	[RPM]
Max Speed Error	62	[RPM]
T_{RT} for 1 [Nm]	113	[ms]
T_{RT} for 5 [Nm]	161	[ms]

Table 6.2. Final results for 600 [RPM]

Parameter	Value	Unit
RMSE Speed	7	[RPM]
Max Speed Error	60	[RPM]
T_{RT} for 1 [Nm]	90	[ms]
T_{RT} for 5 [Nm]	127	[ms]

Table 6.3. Final results for 1800 [RPM]

From Figure 6.1, the left graphs displays the speed change under a 1 Nm load step. The speed decreases with approximately 12 RPM, with a recovery time of 113 [ms]. For the right graphs a 5 Nm load step is added and the speed decreases with 62 RPM while taking 161 [ms] to recover. It is expected that a high load torque causes a high speed change as torque can be related to acceleration, meaning higher torque can cause a higher acceleration. The PI speed controller will need to increase its output by more to counter act the deceleration seen when 5 Nm is applied compared to 1 Nm load step.

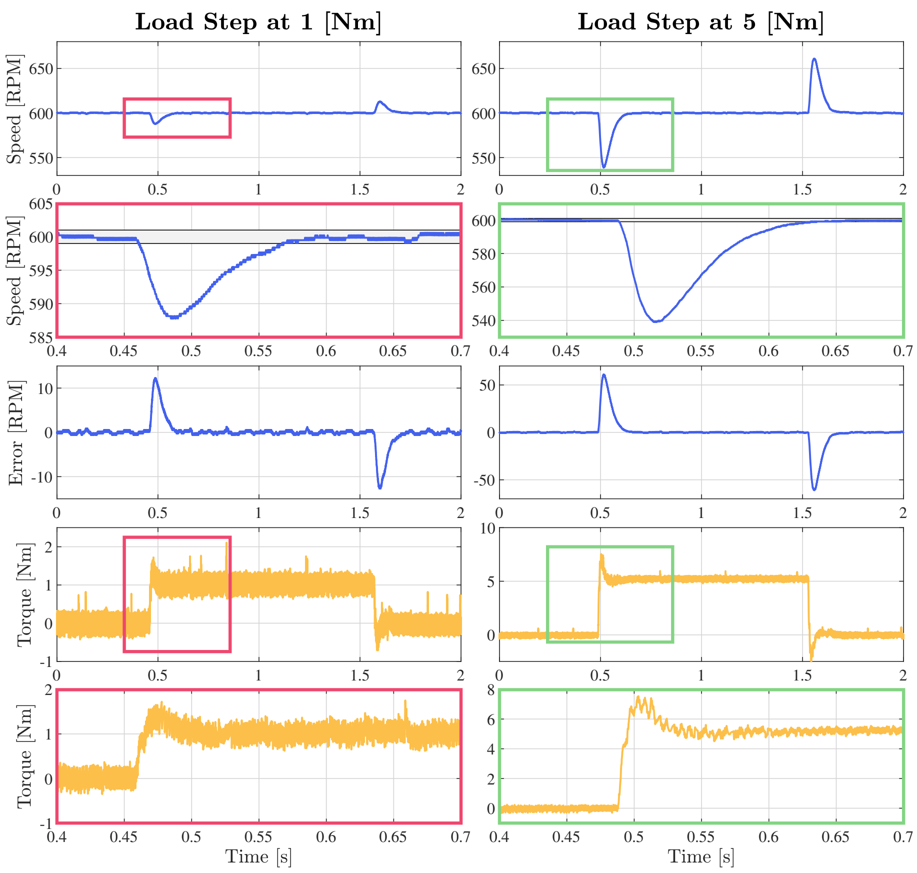

Figure 6.1. Experimental test conducted for 600 [RPM], where the speed and load torques are shown with a zoomed view of the transient response and error graphs for the speed and estimated load torque.

From Figure 6.2, it is seen that the speed error and recovery time do not change by much when increasing the rotor speed to 1800 [RPM]. However, the speed ripples have slightly increased, which indicate that the amplitude of the ripples is influenced by the speed of the rotor.

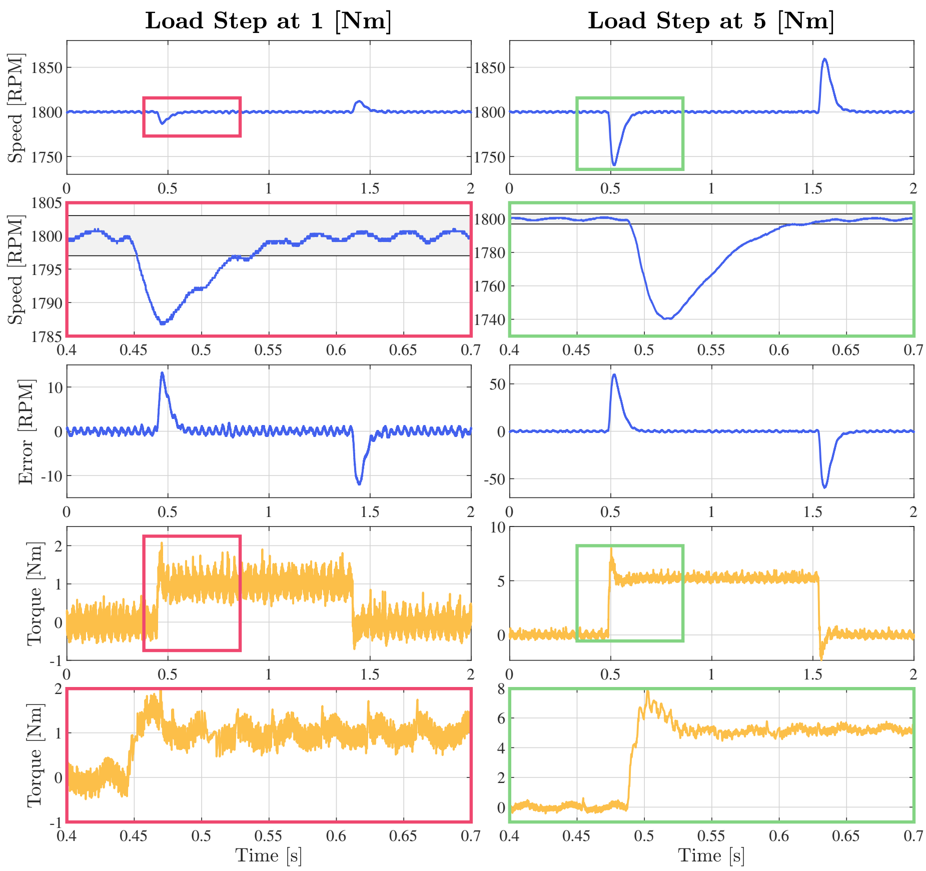

Figure 6.2. Experimental test conducted for 1800 [RPM], where the speed and load torques are shown with a zoomed view of the transient response and error graphs for the speed and estimated load torque.

6.2 Experimental Test of LTID-SMO-Sign

The LTID-SMO-Sign described in Section 5.2 is implemented and tested on the experimental setup. It is analyzed for different speeds and load torque changes. During the analysis, the final parameters determined in Section 5.2.2 are used as initial guess. However, during each test conducted, it was noted that the chattering was too high, resulting in the PMSM being auditory noisy. Therefore, further reducing of the cutoff frequency ω_c was required. The final parameters used for each test are presented with Table 6.4.

Parameter	Simulation	Laboratory	Unit
K_{sign}	3840	3840	[-]
ω_c	35	25	[Hz]

Table 6.4. Control parameters used in the physical lab setup for LTID-SMO-sign.

The results from the test can be seen in Figure 6.3 and 6.4 where a zoomed view of the transient dynamics for the speed and load torque is displayed as well during each test.

The performance parameters of the LTID-SMO-Sign for each test are presented in Table 6.5 and 6.6. The performance parameters includes the speed error ($n_{ref} - n_{meas}$), the estimated load torque error ($T_L - \hat{T}_L$), recovery time, and lastly speed and torque RMSE. Where the recovery time and RMSE are determined with the same approach described in Section 6.1.

Parameter	Value	Unit
RMSE Speed	1.7	[RPM]
RMSE Torque	0.4	[Nm]
Max Speed Error	33	[RPM]
Max Torque Error	5.4	[Nm]
T_{RT} for 1 [Nm]	164	[ms]
T_{RT} for 5 [Nm]	111	[ms]

Table 6.5. Performance for 600 [RPM]

Parameter	Value	Unit
RMSE Speed	1.85	[RPM]
RMSE Torque	0.43	[Nm]
Max Speed Error	32	[RPM]
Max Torque Error	4.3	[Nm]
T_{RT} for 1 [Nm]	70	[ms]
T_{RT} for 5 [Nm]	76	[ms]

Table 6.6. Performance for 1800 [RPM]

From Figure 6.3 it can be seen that the recovery time for low and high torque load is respectively 164 [ms] and 111 [ms], which is a reduction compared to the response without SMO. There is a slight overshoot in the speed response as it tries to recover from the 1 [Nm] load step, which can be seen in the speed error slightly decreasing shortly below 0 [RPM] error. In the case of the larger load step, the overshoot is less noticeable; however, small oscillations occur during the speed recovery. These oscillations are coming from the actual load torque and estimated load torque influencing each other from when feeding forward the current $\hat{i}_q^*$ to the FOC. Therefore, when calculating the actual load torque, described in Section 3.2, the i_q current will now include the extra added dynamics from the LTID-SMO, which causes the actual load torque dynamic to change.

The maximum speed error under a 5 [Nm] load step is 33 [RPM], with a load torque estimations error of 5.4 [Nm]. This means the reduction in speed error is also improved compared to the result without SMO.

The maximum load estimation error happens as the load torque increases initially while the estimated load torque tries to catch up to the actual load torque. In this attempt, during settling, the estimated load torque is higher than the actual load torque at short instances. This can be seen in the right torque error plot for 5 [Nm] when the error is negative. During this time, the speed will be increased too much, causing the oscillating effect in the speed and load torque, which will propagate back to the estimated load torque due to measured speed and current being used in the observer. For the LTID-SMO-Sign, the issue is caused by chattering, which is very prominent in the 1 [Nm] load torque step, almost covering up the actual load torque. Too much chatter can cause issues as this is fed into the FOC as current, which will cause minor rippling in the speed response.

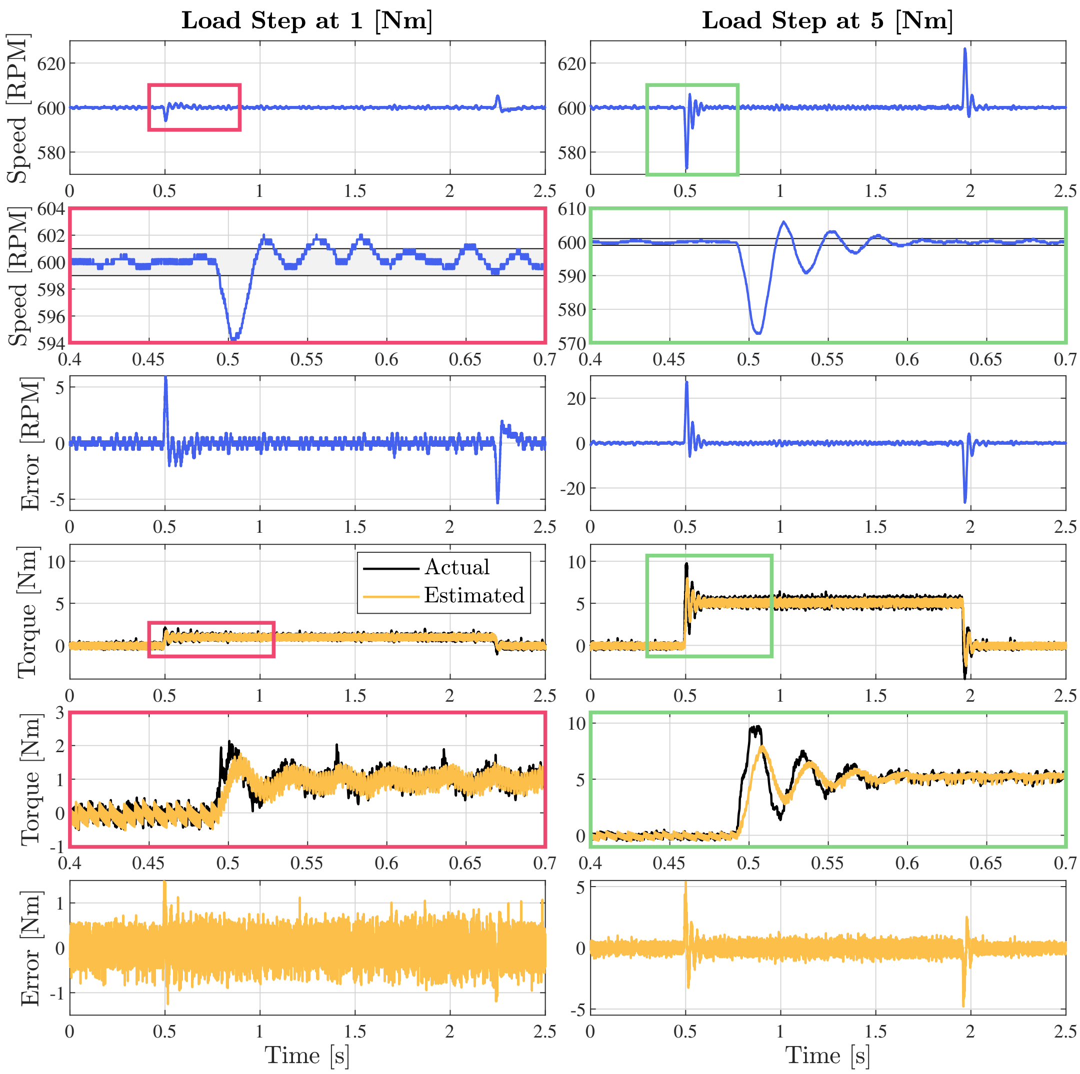

Figure 6.3. Result using LTID-SMO-Sign in lab, running at 600 [RPM]. Left column is for 0 to 1 [Nm] load step and right column is 0 to 5 [Nm] load step.

From Figure 6.4 a similar trend is seen, as for 600 [RPM] test in terms of maximum load torque error and maximum speed error. The actual load torque in left plots for 1 [Nm], actually reaches around 3 [Nm], whereas the estimated load torque tops at just above 2 [Nm]. At the 5 [Nm] load step, the estimated load torque lags slightly behind the actual load torque, primarily due to the low pass filter having a low cutoff frequency.

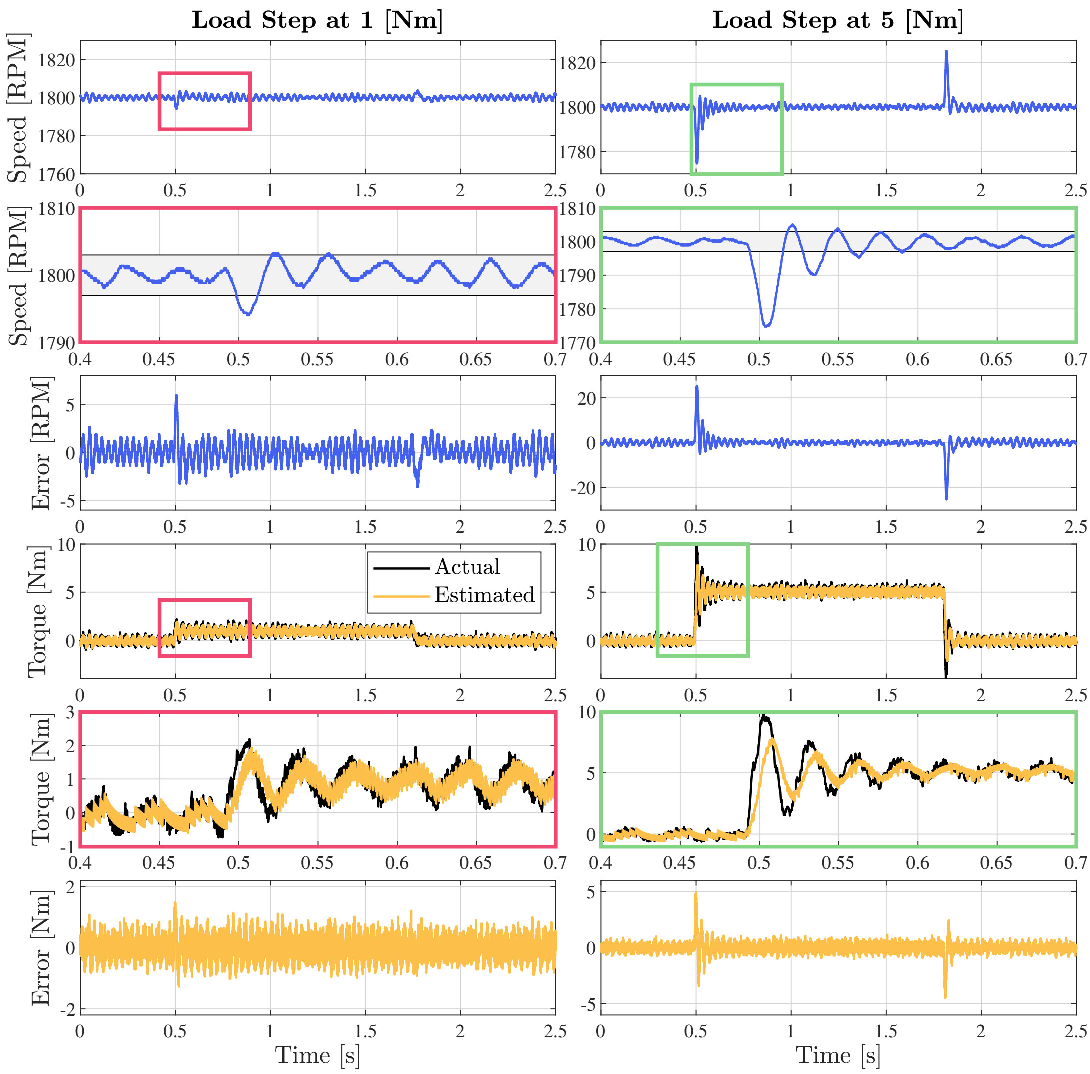

Figure 6.4. Result using LTID-SMO-Sign in lab, running at 1800 [RPM]. Left column is for 0 to 1 [Nm] load step and right column is 0 to 5 [Nm] load step.

6.3 Experimental Test of LTID-SMO with Satuation Function

The LTID-SMO-Sat described in Section 5.3 is implemented into the experimental setup and analyzed for the same speed and load torque changes as described in Section 6.2. The determined simulation parameters are again used as benchmark values when implementing the LTID-SMO to the drive system. During the test, it was noticed that the simulation parameters were too aggressive for the experimental setup, and some retuning was made to obtain satisfactory results. The final parameters used for each test are presented with Table 6.7.

Parameter	Simulation Value	Laboratory Value	Unit
K_{sat}	11000	6000	[-]
Δ	25	25	[-]
k_f	2	2	[-]
ω_c	40	40	[Hz]

Table 6.7. Control parameters used in the physical lab setup for LTID-SMO-Sat.

The results from the test can be seen in Figure 6.5 and 6.6, showing the measured speed and load torques. In addition, the final performance parameters are given by Table 6.8 and 6.9.

Parameter	Value	Unit
RMSE Speed	1.5	[RPM]
RMSE Torque	0.3	[Nm]
Max Speed Error	24	[RPM]
Max Torque Error	4.3	[Nm]
T_{RT} for 1 [Nm]	88	[ms]
T_{RT} for 5 [Nm]	103	[ms]

Table 6.8. Performance for 600 [RPM]

Parameter	Value	Unit
RMSE Speed	1.6	[RPM]
RMSE Torque	0.35	[Nm]
Max Speed Error	28	[RPM]
Max Torque Error	4.6	[Nm]
T_{RT} for 1 [Nm]	16	[ms]
T_{RT} for 5 [Nm]	90	[ms]

Table 6.9. Performance for 1800 [RPM]

From Figure 6.5 it can be seen that the LTID-SMO-Sat can effectively reduce the speed error while in the process have lower chattering in the load torque estimation and speed response compared to the conventional method. The improvement is expected since the LTID-SMO-Sat was designed to attenuate chattering and increase the accuracy of the estimated load torque by adding the additional feedback term $Z_{es} \cdot L$, which mainly contains the low-frequency component of the estimated torque and replacing the *sign* function with a *saturation* function. As a result, a faster convergence time and increased bandwidth of the LTID-SMO-Sat can be obtained. The chatter is small without considerable phase lag between estimated and actual load. This is beneficial for the speed response, which results in minor errors and quick recovery.

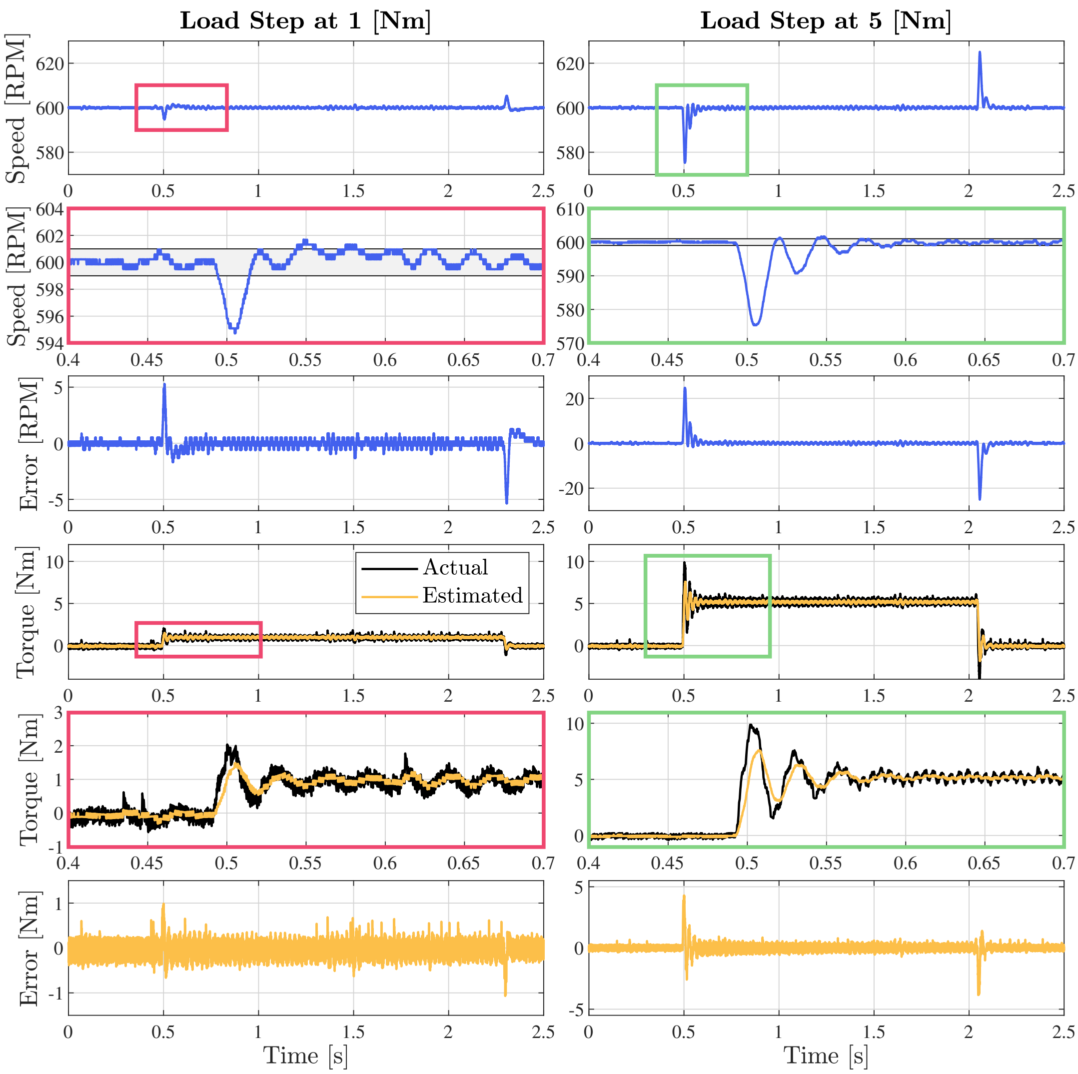

Figure 6.5. Result using LTID-SMO-Sat in lab, running at 600 [RPM]. Left column is for 0 to 1 [Nm] load step and right column is 0 to 5 [Nm] load step.

Figure 6.6 is the LTID-SMO-Sat running at 1800 RPM. Similar to lower speed the estimated load torque is good, resulting in low speed error through the transient part. Besides this, the chatter in the load torque is low both during transient and steady state. The recovery time is for 1 and 5 Nm is 16 [ms] and 90 [ms] respectively, with the RMSE for torque and speed being only 0.35 [Nm] and 1.6 [RPM] respectively. The oscillations with a frequency of 30 Hz which was also seen when running without the LTID-SMO, is still present. The amplitude is slightly increased compared to without the observer but still within a acceptable range.

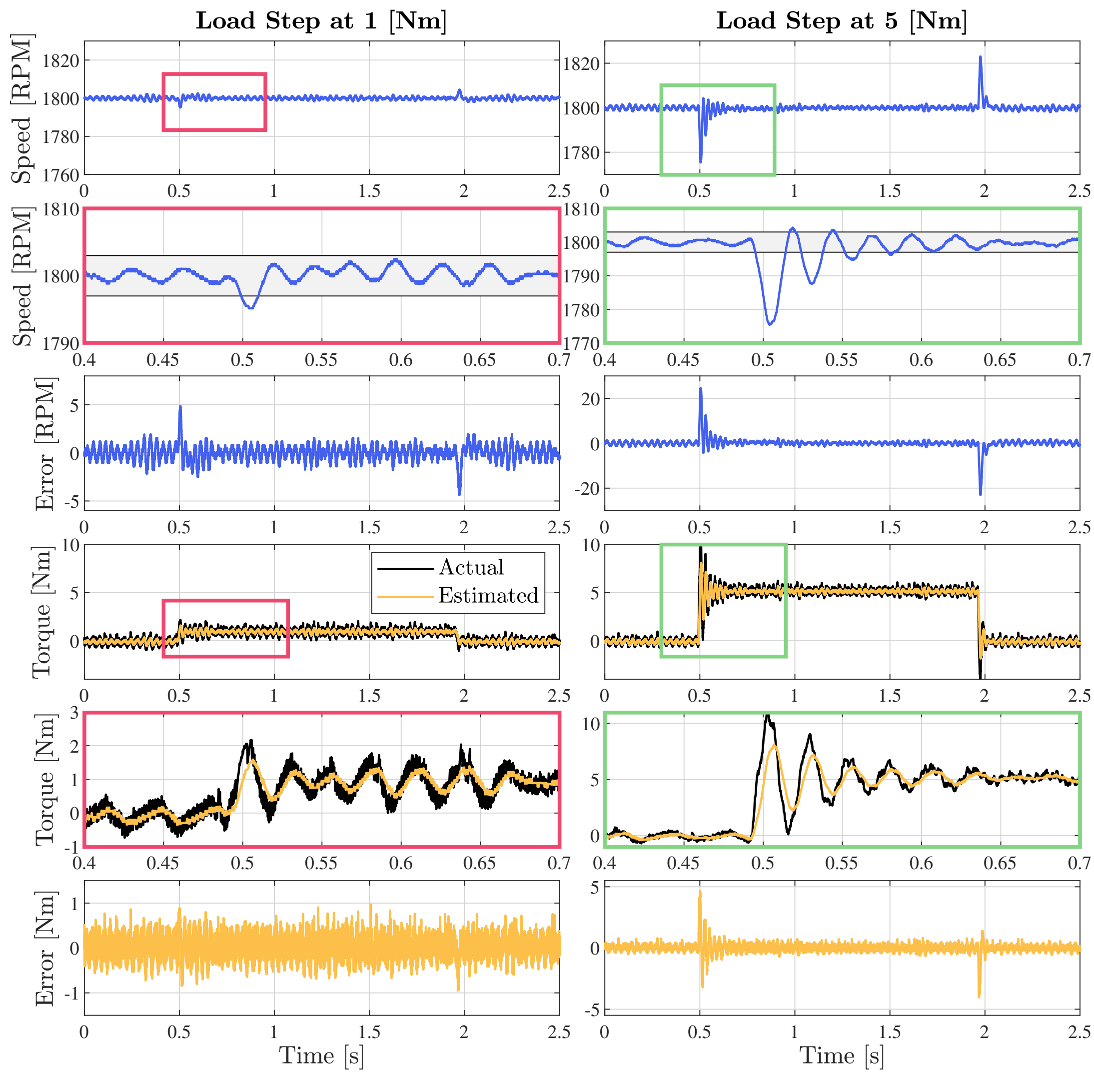

Figure 6.6. Result using LTID-SMO-Sat in lab, running at 1800 [RPM]. Left column is for 0 to 1 [Nm] load step and right column is 0 to 5 [Nm] load step.

6.4 Experimental Test of LTID-SMO with Power-Sigmoid Function

The LTID-SMO-PS described in Section 5.4 was implemented into the experimental setup and analyzed for the same speed and load torque changes as preciously described for LTID-SMO-Sat- and Sign. Furthermore, the following section is divided into two parts. The first part 6.4.1, describes the experimental data for the LTID-SMO with a regular sliding mode gain K_{PS}. In the second part 6.4.2, the experimental data for the LTID-SMO with the PI controller implemented is displayed.

6.4.1 LTID-SMO-PS-$\mathrm{K_{PS}}$

The simulation parameters are used in the experimental setup, where only the sliding mode gain K_{PS} has been marginally retuned to obtain a satisfactory result. The final parameters are given by Table 6.10.

Parameter	Simulation Value	Laboratory Value
K_{PS}	3000	2800
α	3	3
δ	1500	1500

Table 6.10. Control parameters used in the physical lab setup for LTID-SMO-PS-$\mathrm{K_{PS}}$.

The results from the experimental tests can be seen in Figure 6.7 and 6.8 with the final performance parameters are given by Table 6.11 and 6.12.

Parameter	Value	Unit
RMSE Speed	1.7	[RPM]
RMSE Torque	0.3	[Nm]
Max Speed Error	32	[RPM]
Max Torque Error	4.5	[Nm]
T_{RT} for 1 [Nm]	96	[ms]
T_{RT} for 5 [Nm]	106	[ms]

Table 6.11. Performance for 600 [RPM]

Parameter	Value	Unit
RMSE Speed	2	[RPM]
RMSE Torque	0.37	[Nm]
Max Speed Error	32	[RPM]
Max Torque Error	4.8	[Nm]
T_{RT} for 1 [Nm]	21	[ms]
T_{RT} for 5 [Nm]	76	[ms]

Table 6.12. Performance for 1800 [RPM]

From Figure 6.7, it is seen on the right subplots, that the estimated load torque for 5 [Nm] does not manage to closely follow the actual load torque during the initial part of the transient response. Therefore, indicating the sliding mode gain should be increased to obtain better estimation accuracy. However, increasing K_{PS} will also result in more chatter in the estimation. Therefore no further tuning of the sliding mode gain is made. The speed response for 1 [Nm] shows a minor overshoot above the reference at 600 [RPM], which is due to to the torque error being shortly negative during the transient part of the load step. Negative torque error means the estimated load torque is higher than the actual load torque. High estimated load torque will result in increased acceleration, hence the overshoot is seen.

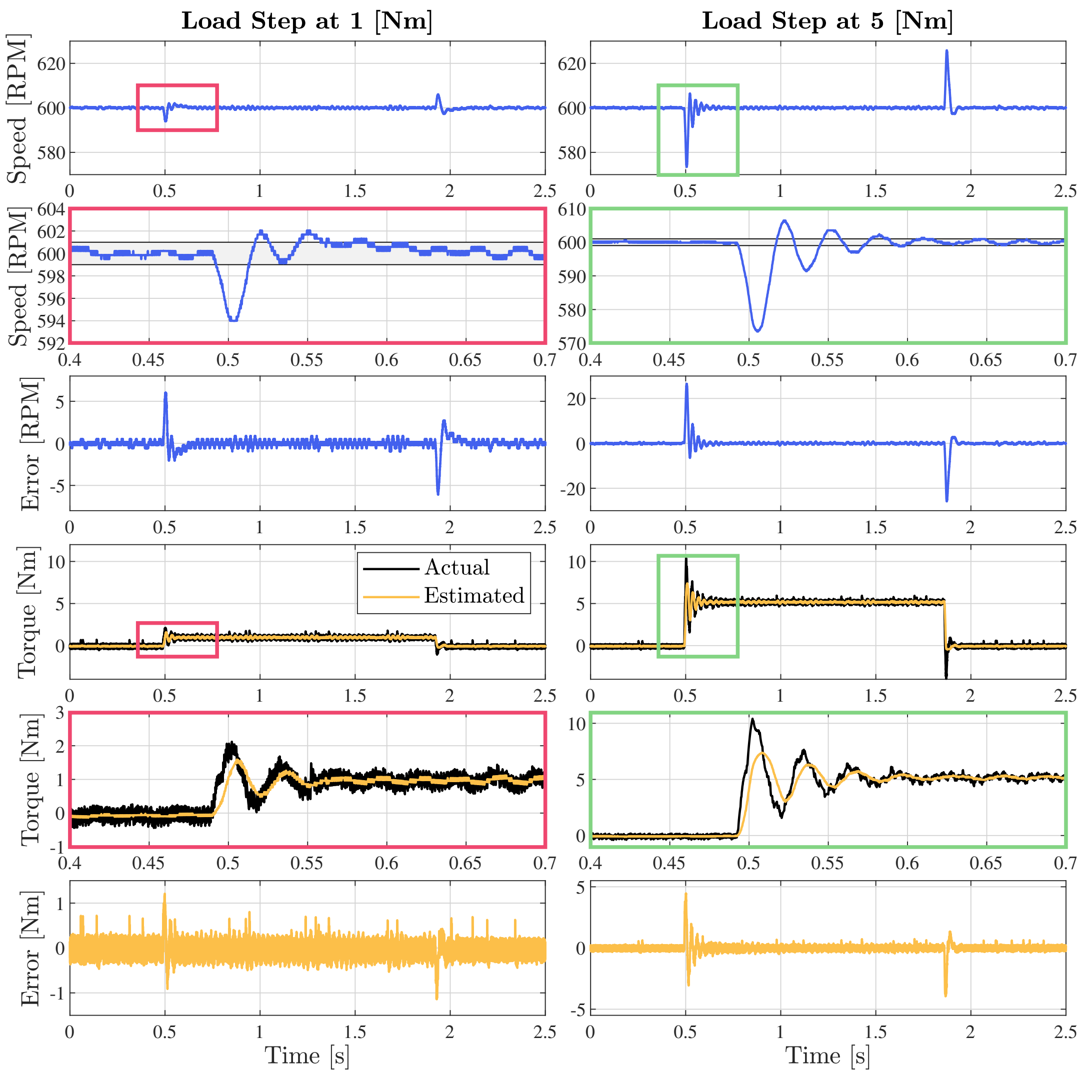

Figure 6.7. Result using LTID-SMO-PS-K_{PS} in lab, running at 600 [RPM]. Left column is for 0 to 1 [Nm] load step and right column is 0 to 5 [Nm] load step.

From Figure 6.8, it is seen that the LTID-SMO-PS-K_{PS} for 1800 [RPM] shows similar results as the test conducted for 600 [RPM], where the estimated load torque for 5 [Nm] does not manage to reach all the actual load torque dynamic fully. If looking at the estimation accuracy for 1 [Nm], the estimated load torque manages to capture most of the actual load torque dynamic. The most noticeable difference between the two tests is the recovery time, which has been significantly reduced for 1800 [RPM]. Due to the design of the PS-function, the chattering is effectively reduced. Thereby, the oscillation in the speed response remains smaller than the error band of ± 3 [RPM] which in return results in a fine recovery time. To final conclude the above analysis, the overall performance for both tests conducted shows the LTID-SMO-PS-K_{PS} managed to reduce the errors for the speed response and improve the chattering and the recovery time in the drive system.

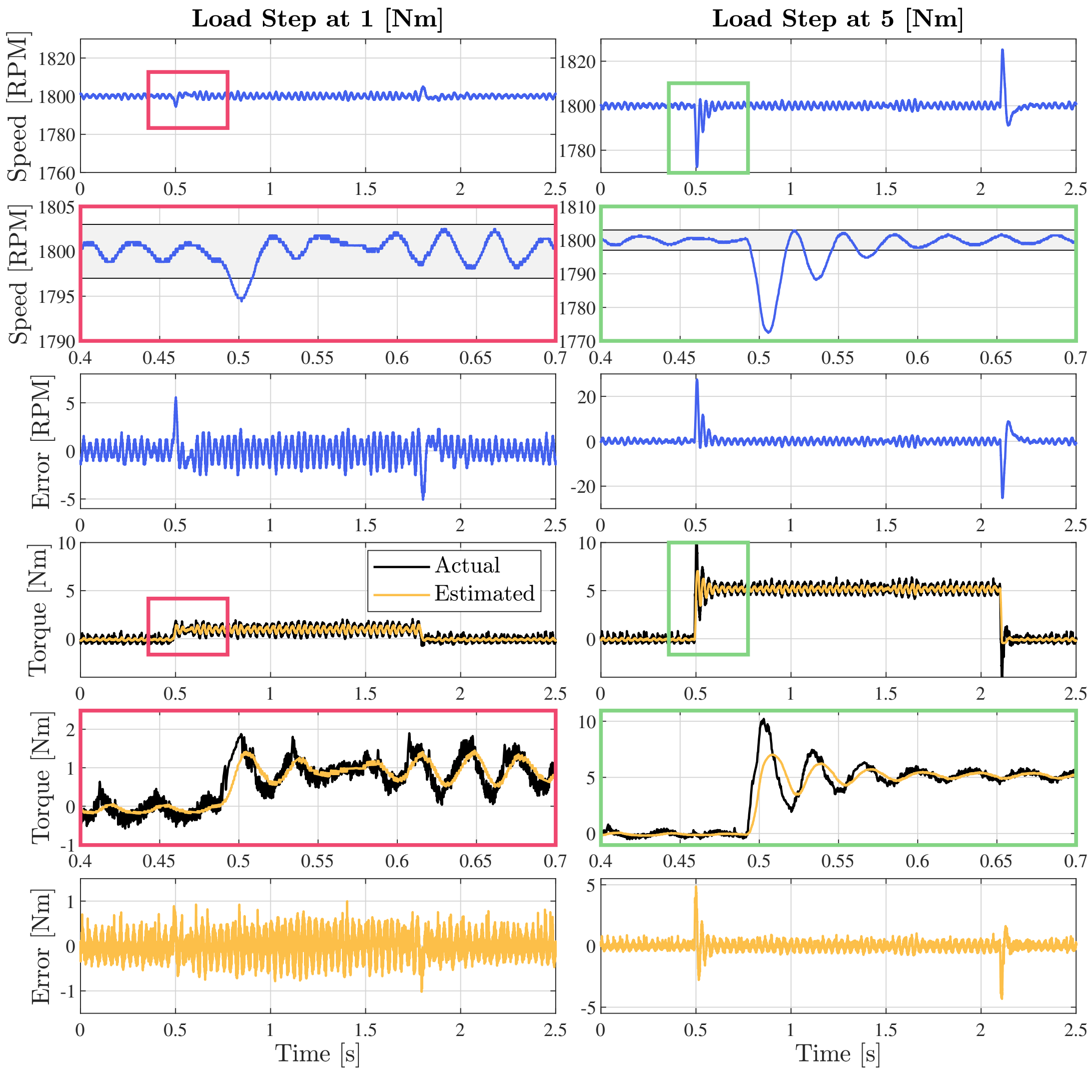

Figure 6.8. Result using LTID-SMO-PS-K$_{PS}$ in lab, running at 1800 [RPM]. Left column is for 0 to 1 [Nm] load step and right column is 0 to 5 [Nm] load step.

6.4.2 LTID-SMO-PS with PI controller

The simulation parameters are used in the experimental setup, where no additionally retuning was made for the following two tests. The final parameters are given by Table 6.13.

Parameter	Simulation Value	Laboratory Value
$K_{P,SMO}$	3000	3000
$K_{I,SMO}$	15000	15000
α	3	3
δ	1500	1500

Table 6.13. Control parameters used in the physical lab setup for LTID-SMO-PS with PI.

The results from the experimental tests can be seen in Figure 6.9 and 6.10 with the final performance parameters are given by Table 6.14 and 6.15.

Parameter	Value	Unit
RMSE Speed	2.5	[RPM]
RMSE Torque	0.4	[Nm]
Max Speed Error	41	[RPM]
Max Torque Error	5.7	[Nm]
T_{RT} for 1 [Nm]	144	[ms]
T_{RT} for 5 [Nm]	125	[ms]

Table 6.14. Performance for 600 [RPM]

Parameter	Value	Unit
RMSE Speed	2.4	[RPM]
RMSE Torque	0.4	[Nm]
Max Speed Error	43	[RPM]
Max Torque Error	6	[Nm]
T_{RT} for 1 [Nm]	72	[ms]
T_{RT} for 5 [Nm]	97	[ms]

Table 6.15. Performance for 1800 [RPM]

Figure 6.9 present the test conducted at 600 [RPM]. From the load step at 1 [Nm] and 5 [Nm] the recovery time is respectively 144 [ms] and 125 [ms]. The recovery time at 5 [Nm], could be faster if oscillations was reduced more quickly or complete eliminated. The speed quickly rises back to the reference speed but oscillates around it for approximately 75 [ms] before settling within the error band. The larger overshoot for 1 [Nm] is due to the estimated load torque not being able to follow the actual load torque during the first part of the transient response. Whereas the estimated load torque for 5 [Nm] is better at quickly estimating the actual load torque throughout the transient part. If inspecting the chattering in the load torque estimation, it is seen that the chattering is small before and after the load step is applied. This is also expected, as the LTID-SMO-PS-PI method was designed to better attenuate chatter after an applied load step due to the integrator driving the sliding variable towards zero.

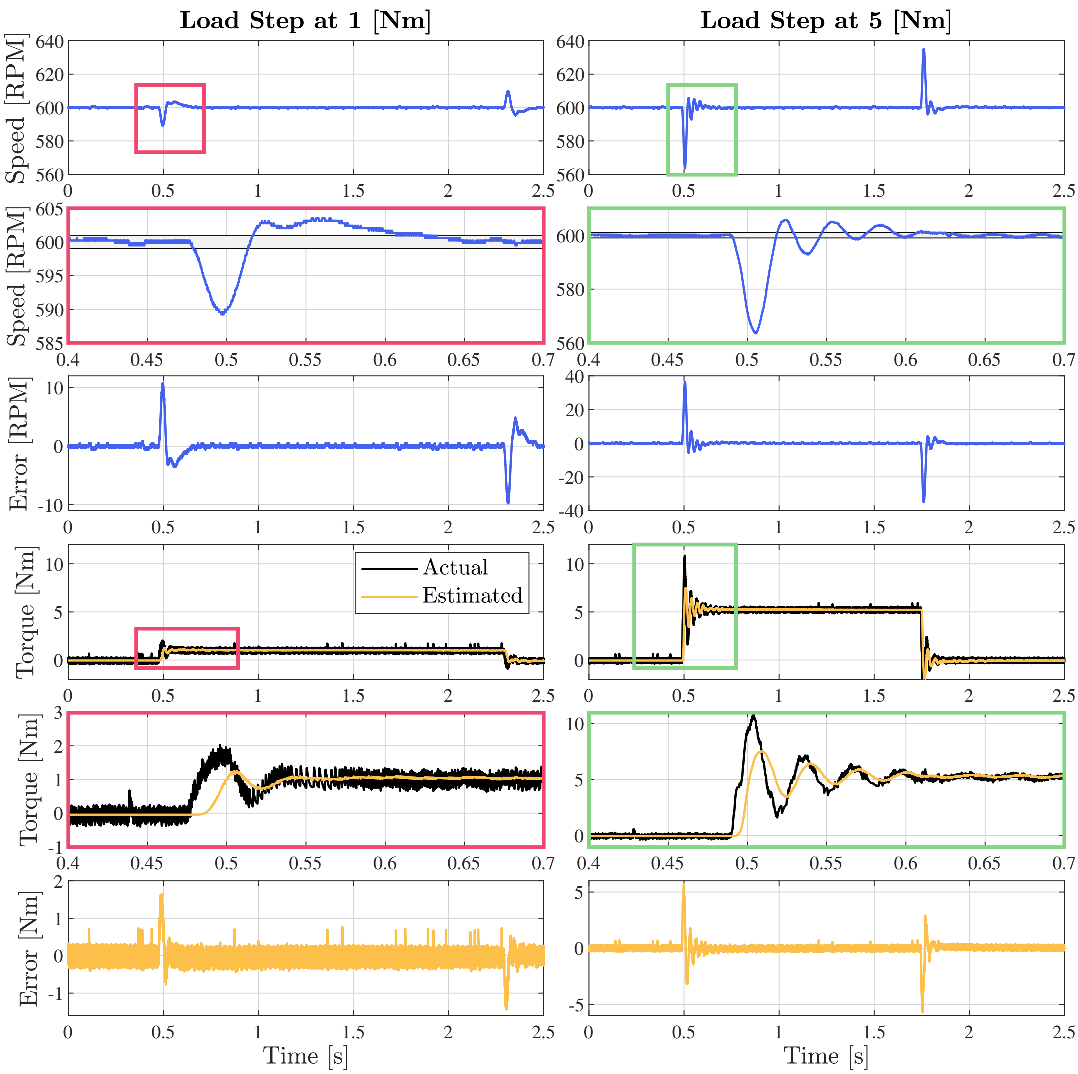

Figure 6.9. Result using LTID-SMO-PS-PI, running at 600 [RPM]. Left column is for 0 to 1 [Nm] load step and right column is 0 to 5 [Nm] load step.

From Figure 6.10, it is seen that the LTID-SMO-PS-PI, under 1800 [RPM] test shows similar results as the test conducted for 600 [RPM], with only minor deviation in the speed and estimated load torque errors. From the load step at 1 [Nm] and 5 [Nm] the recovery time is respectively 72 [ms] and 97 [ms]. The fastest recovery time occurs at 1 [Nm]. Here it is seen that the estimated load torque error at 1 [Nm] does not have large negative values, which will cause the overshoot above the reference to be smaller, thereby settling quicker than the speed response at 5 [Nm].

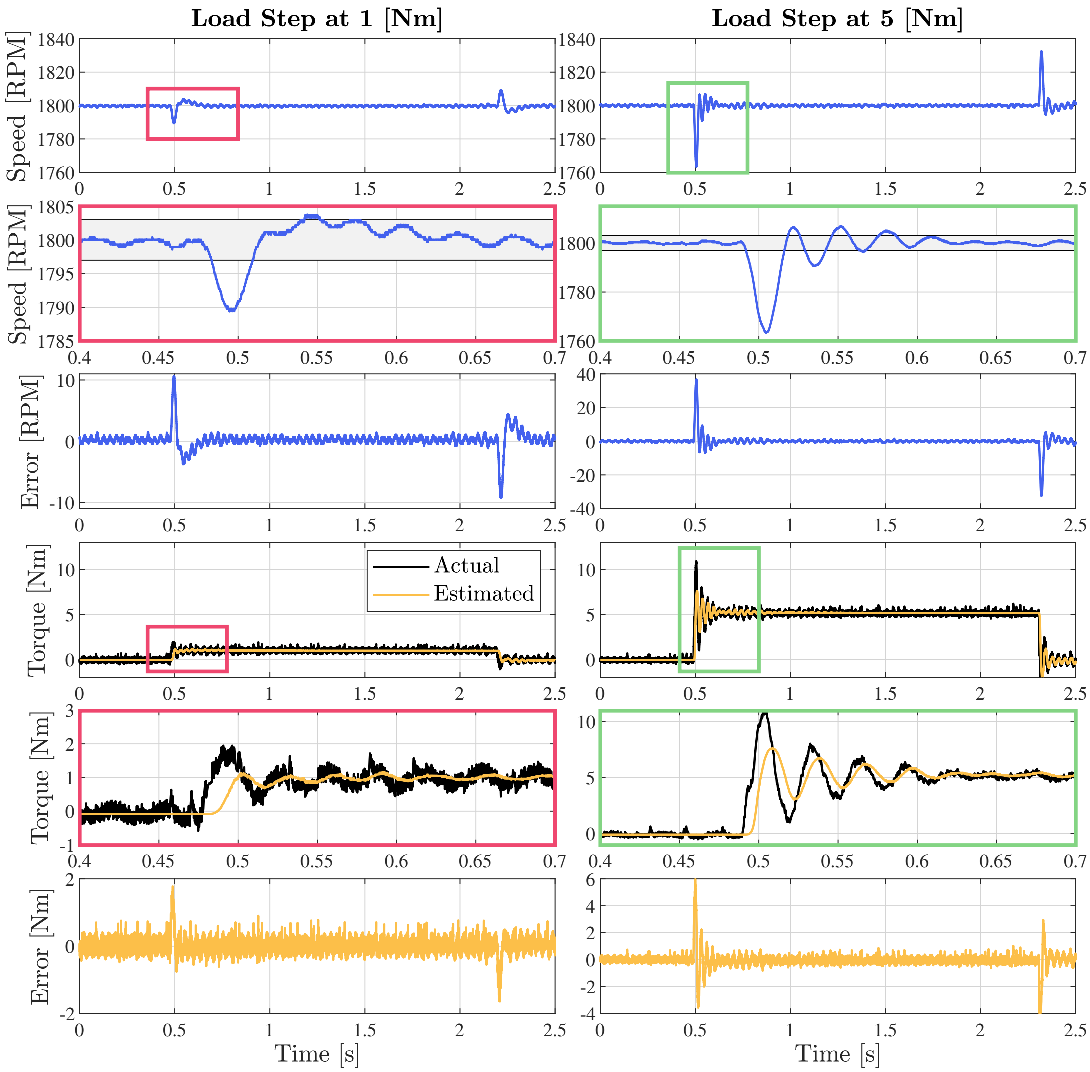

Figure 6.10. Result using LTID-SMO-PS-PI in lab, running at 1800 [RPM]. Left column is for 0 to 1 [Nm] load step and right column is 0 to 5 [Nm] load step.

7 Discussion

In this chapter, a comparison between the simulation and experimental results are made. Afterward, a comparison is made for the experimental results of the four different LTID-SMO methods, described in Chapter 6. Finally, a short FFT analysis is presented, investigating the mechanical frequency occurring in the drive system.

7.1 Comparison of Simulation and Experiment results

The LTID-SMOs in lab and in simulation is compared and discussed in this section. It is shown if there is a good fit between them and if they have similar trend, so it can be confirmed if the simulated SMO is valid. The simulated system in this section is using the load torque which is calculated based on the lab result running with the observer. That is, for simulating the observer with a sign function, the load torque comes from lab test using the sign function with the same parameters.

Figure 7.1 shows the lab test and simulation using the sign function. Both the speed response and the load torque estimation is similar when getting same load torque profile, which can be seen as the blue line hides under the yellow line. The chatter has similar magnitude and the load estimation lag compared to the actual load torque is the same.

Figure 7.2 is the comparison when using saturation switchign function. As before, the response is similar and between simulation and lab test. The lab test have slightly larger torque oscillation amplitude than the simulation, but only by a small amount, so that the recovery time is still the same. The chatter level is smaller than the actual load torque for both the lab and the simulation showing the benefit of the saturation function in reducing chatter while still having fast estimation.

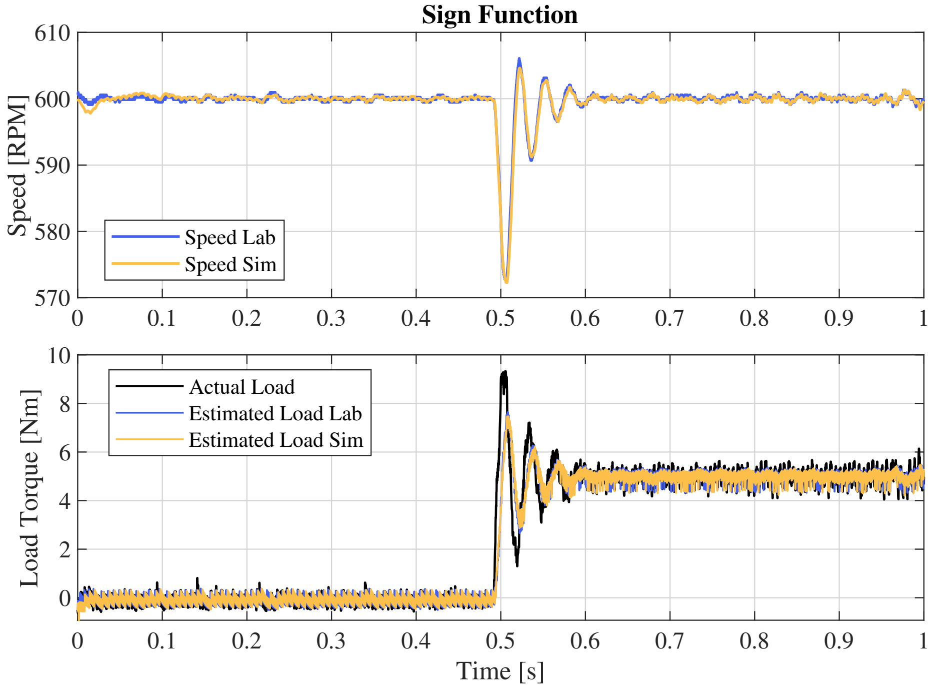

Figure 7.1. Comparison of the experimental and simulated results for the LTID-SMO-Sign.

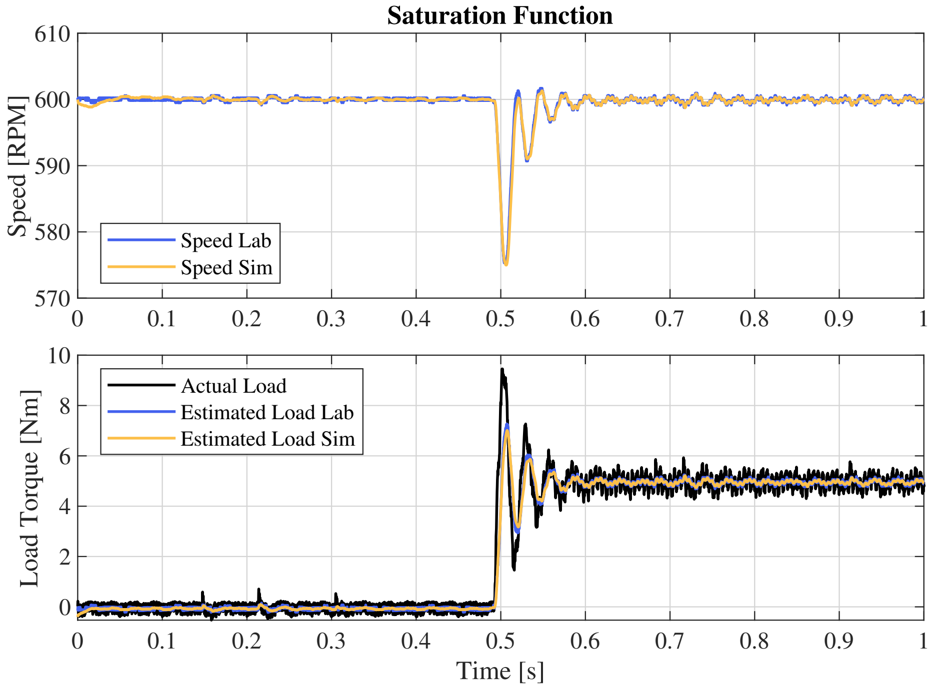

Figure 7.2. Comparison of the experimental and simulated results for the LTID-SMO-Sat.

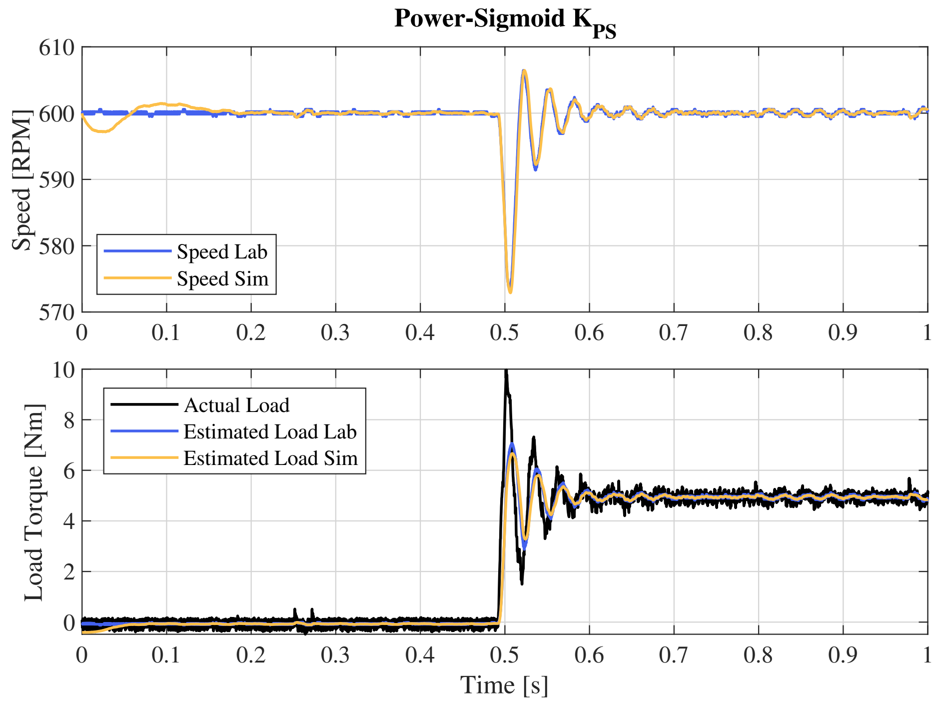

Figure 7.3. Comparison of the experimental and simulated results for the LTID-SMO-PS-K_{PS}.

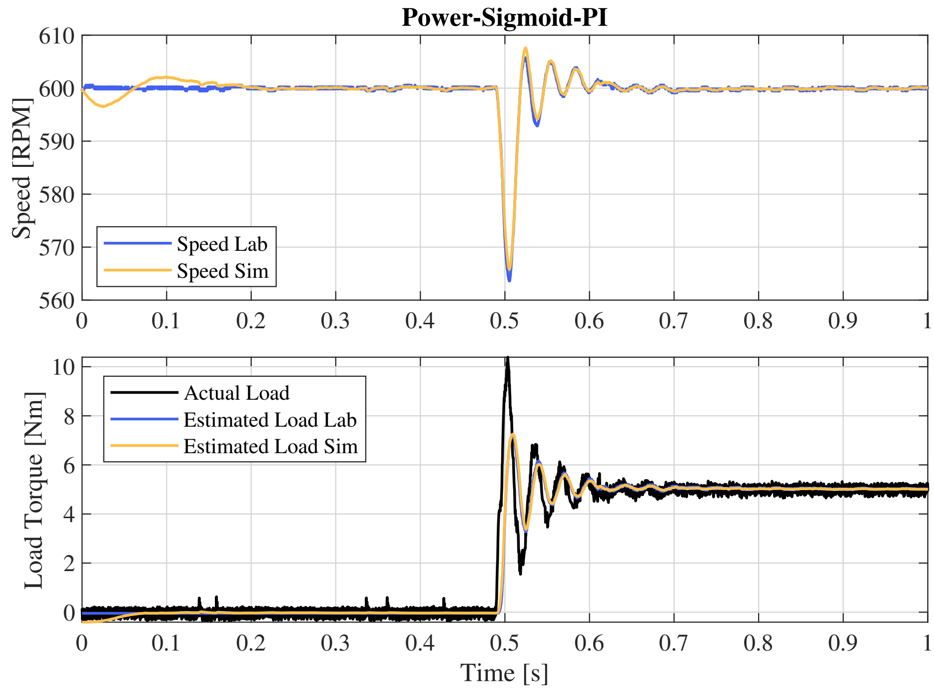

Figure 7.4. Comparison of the experimental and simulated results for the LTID-SMO-PS-PI.

Figure 7.3 is the third LTID-SMO-PS-K_{PS}. The speed and torque response has a similar trend between the two when using the exact same SMO parameters, both having the oscillating behavior due to the load torque. The first 0.2 [s] of the response is a little different between each other, however, this can be explained by the initial conditions. As the simulation is started different initial conditions can be given. Both for the initial speed which is running at 600 [RPM], the current i_q may not be zero, etc. This explains why it is seen that the simulation after some time stabilizes around the lab measurement.

The forth Figure 7.4 shows the Power-Sigmoid using a a PI after the switching function, LTID-SMO-PS-PI. Both simulation and experiment is able to reduce the ripples seen, some time after the load step appears, as is expected due to the PI controller in the LITD-SMO. The estimation is the same for both lab and simulation. As the previous Figure 7.3, the start is due to some mismatch in initial conditions, but otherwise no major differences is to be seen.

For all SMO used, the simulation matches the lab test well. The trends are the same and chatter level is about the same as well, proving the simulation as a good tool to develop the LTID-SMOs.

7.2 Comparison of LTID-SMO Methods

In this section, the performance of the LTID-SMO methods is analyzed and compared against each other. The speed response and estimated load torque are used to compare each method. Furthermore, the steady-state response is used to compare the methods. The comparison is only made for a load step of 5 [Nm], running at 600 and at 1800 [RPM].

7.2.1 Test at 600 [RPM] for 5 [Nm] load step

The speed and load torque RMSE, the maximum speed error(peak to peak) and torque errors obtained though Chapter 6 are presented again in Table 7.2.

	Speed Error [RPM]		Torque Error [Nm]	
	RMSE	Max	RMSE	Max
Without LTID-SMO	7	62	-	-
LTID-SMO-Sign	1.7	33	0.4	5.4
LTID-SMO-Sat	1.5	24	0.3	4.3
LTID-SMO-PS-K_{PS}	1.7	27	0.3	4.5
LTID-SMO-PS-PI	2.5	41	0.4	5.7

Table 7.2. Error summary at 600 [RPM].

Figure 7.5 presents the speed response. To analyse and compare the LTID-SMO methods the *peak-to-peak* value and *recovery time* will be analysed separately, where Table 7.2 will be used to further understand each speed response.

In Figure 7.6 and 7.9 shows peak-to-peak error and RMSE. These values in the figures are based on the data seen in the respective graphs.

Peak-to-peak error: From the Figure 7.5, it is seen that all the LTID-SMO methods have similar behavior, where all overshoots above the reference of 600 [RPM] before settling, explained by the SMO adding extra dynamic to the drive system. The LTID-SMO-Sat is showing the best result regarding the peak-to-peak value. This is also expected, as the same may be concluded from Table 7.2 where the LTID-SMO-Sat is showing the best results for the RMSE and lowest maximum errors. The LTID-SMO-PS-K_{PS} have similar results as LTID-SMO-Sat with only minor deviation.

The LTID-SMO-Sign and LTID-SMO-PS-PI have the worst peak-to-peak values, where the LTID-SMO-PS-PI has the slowest response and by far largest peak-to-peak value of 36.4 [RPM] during the transient part. Logically, this can be explained if considering what happens to the sliding variable. Due to the PI, as mentioned in previous chapter 5.4.2, the sliding variable is driven to zero. When a load step then happens, the sliding variable increases, thereby increasing its output to estimate a load torque. Initially, with a sliding variable between -4 to 4, the output changes very little, since a σ in this area almost outputs zero. Therefor, the sliding variable needs to be above $\sigma = 4$, for the switching function output to have a real impact. The LTID-SMO-PS-PI will therefor always suffer in the start of the transient estimation of a load torque, compared to the other methods. This is further explained later in this subsection when analysing the load torque and sliding variable in Figures 7.7 and 7.8.

Recovery time: In Figure 7.5, it can be seen the LTID-SMO-Sat shows the best recovery time, which its peak-to-peak value can explain. Having a low peak-to-peak value will contribute to a lower recovery time. This is seen around the error band, where the SMOs with high peak-to-peak values also have the highest recovery time due to their oscillations. The estimated load torque is analyzed next in Figure 7.7 and 7.9 to explain the speed response further.

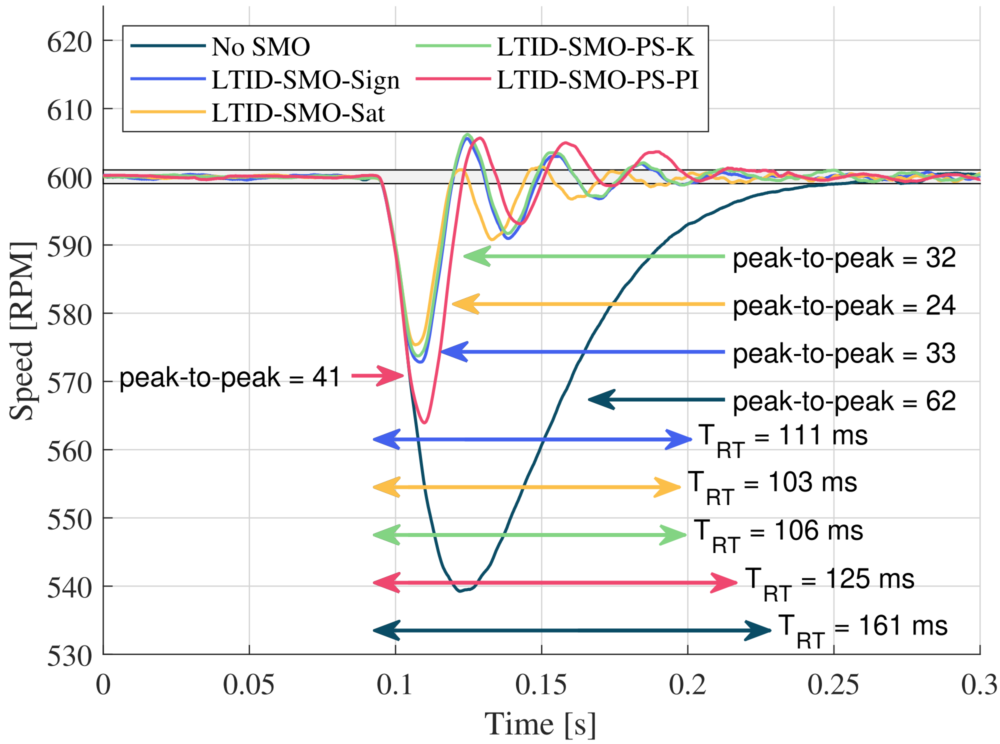

Figure 7.5. Experimental comparison of the LTID-SMO methods for the speed response.

Speed in steady state: If investigating the steady-state part of the speed response seen in Figure 7.6, the LTID-SMO-PS-PI shows the best improvement for reducing chatter between the previous described LTID-SMO methods. The LTID-SMO-PS-PI was designed to reduce chattering in steady-state due to the integrator driving the sliding variable towards zero, which is proved by the low chatter in steady state. Suppose, comparing the LTID-SMO-PS-PI to the system without any LTID-SMO during the steady state part in Figure 7.6, the highest absolute RPM value and RMSE are almost identical. The LTID-SMO-PS-PI has an peak to peak RPM value of 0.73 and an RMSE of 0.15. Thereby only deviating from the system without the LTID-SMO by 0.09 RPM which is negligible. The LTID-SMO-Sign shows the highest RMSE, and peak to peak value, which is also expected as the sign function contributes to larger chattering due to its nature, as it has a discontinuity jump at $\sigma = 0$, leading to greater chattering.

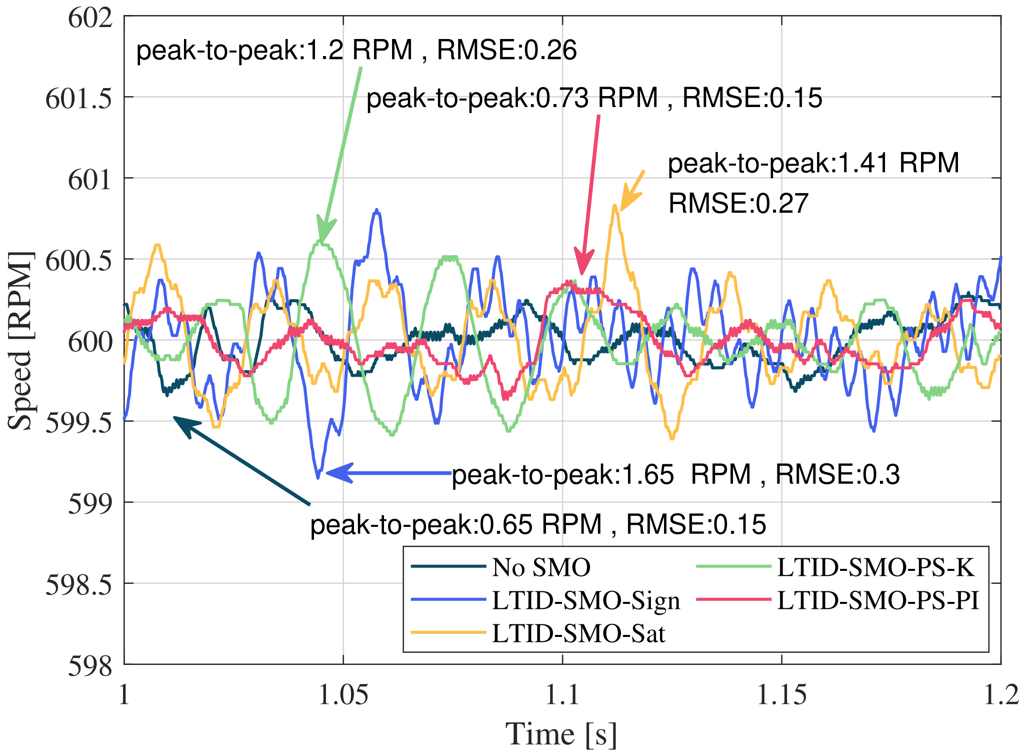

Figure 7.6. Experimental comparison of the LTID-SMO methods for the speed response in steady-state.

In Figure 7.7 the estimated load torque is presented for each LTID-SMO method. A direct comparison of the LTID-SMO regarding the estimation accuracy is not possible in this case, as each LTID-SMO methods contribute to different i_q measurements, leading to the actual load torque being different for each method. However, it is possible to analyze the chattering and transient performance for each LTID-SMO method. Figure 7.9 displays the load torque estimation in steady state and Figure 7.8 shows the sliding variable.

Transient response: Figure 7.7 is the transient load torque estimation. From the response, it is clear that the LTID-SMO-Sat is showing the best performance, as it has fast torque estimation over the other methods, which can be seen by it leading the others. This can be explained by the feedback, Z_s, in the observer structure of the LTID-SMO-Sat method. The feedback Z_s is directly fed back without filtering through the LPF, giving fast dynamics. This results in a fast transient response for the estimated load torque and low chatter. On the other hand, the LTID-SMO-PS-PI has the slowest transient response as it has some initial delay at the start of the load step resulting in the LTID-SMO-PS-PI lagging behind the other methods throughout the transient part. This can be furhter understood by investigating the sliding variable next.
The sliding variable is displayed in Figure 7.8. It is seen that the sliding variable starts at $\sigma \approx 0$ for LTID-SMO-PS-PI, resulting in the output of the PS-function being close to zero ($u_{ps} \approx 0$). Leaving that, for the first part of the transient response, only the integral term $\frac{K_I}{s}$ are contributing to the estimated load torque, resulting in slow initial response, thereby,

an delay is occurring at the beginning of the estimated load torque with this method. The saturation can also be seen having a low sliding variable under no load, but its switching output increases linearly with the sliding variable, thereby having greater output at same sliding variable value. For example, the output from the switching function for saturation and PS-PI is calculated as: $\frac{\sigma}{25}$ and $\frac{\sigma^3}{|\sigma|^3+1500}$. This means for example when $\sigma = 1$ the Saturation switching function outputs 0.04 while the PS-PI switching function outputs only 0.0007. The saturation therefor allow for the fast transient dynamics which is not seen in the PS-PI.

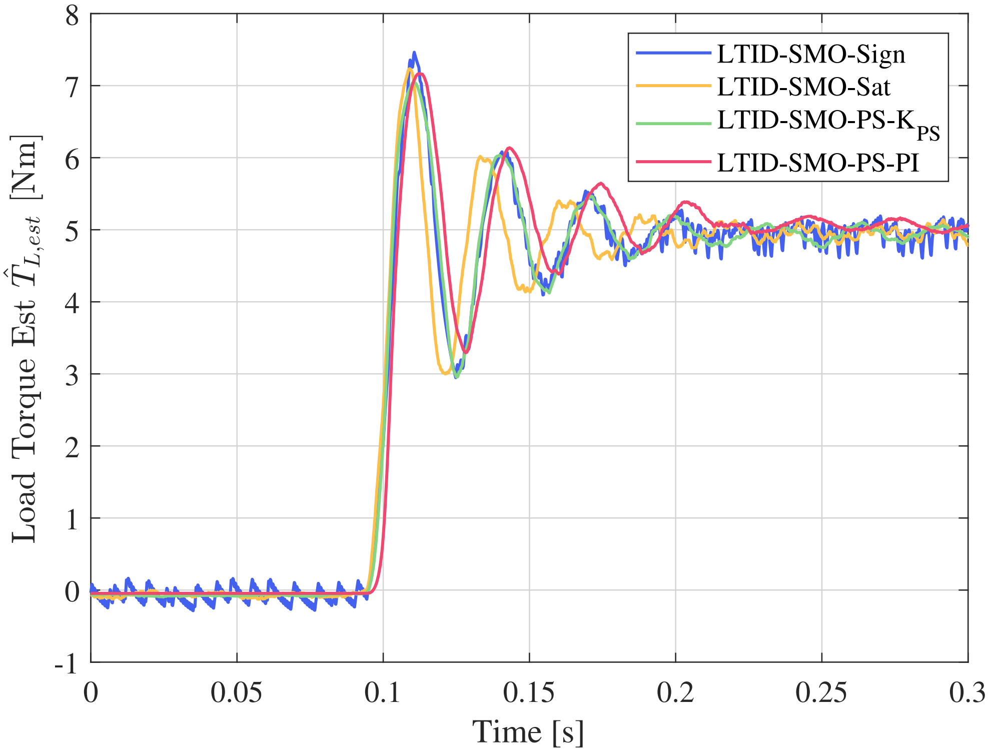

Figure 7.7. Experimental comparison of the LTID-SMO methods for the estimated load torque.

Chattering: In Figure 7.9 is the torque estimation during steady state. The LTID-SMO-Sign clearly shows the highest chattering level. In contrast, as before the LTID-SMO-PS-PI shows the best results by the smoothness of the estimated load torque. The LTID-SMO-Sat and -PS-K_{PS} show a similar chattering level.

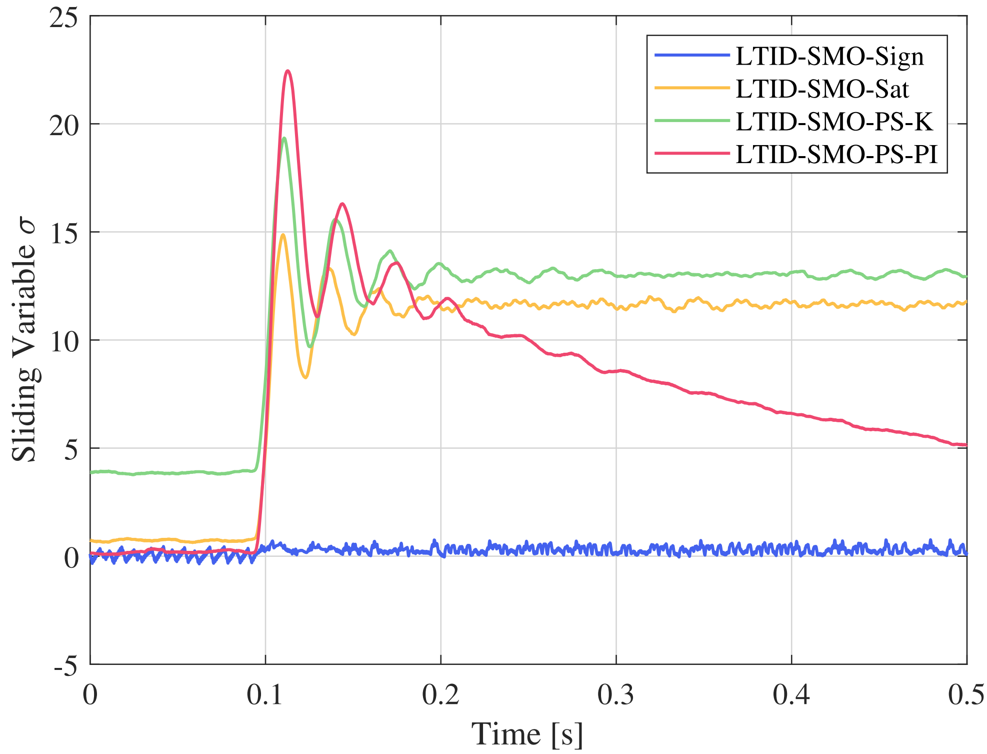

Figure 7.8. Experimental comparison of the LTID-SMO methods for the sliding variable.

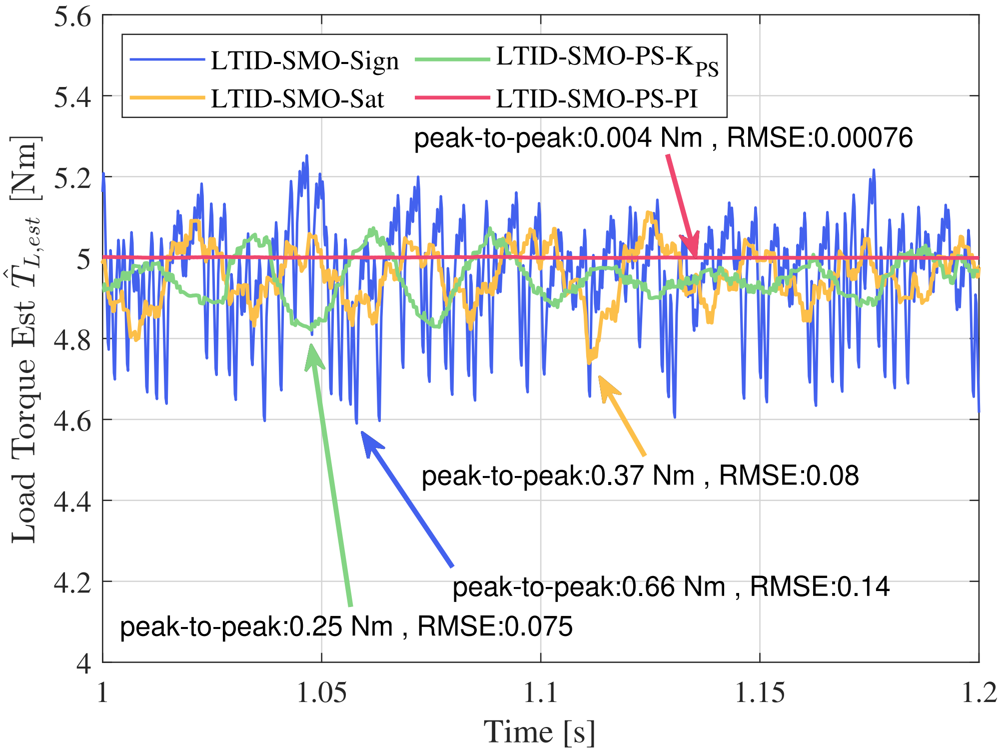

Figure 7.9. Experimental comparison of the LTID-SMO methods for the estimated load torque in steady-state.

Summary for the test at 600 [RPM]

To summarize the above analysis for the test at 600 [RPM], each LTID-SMO method will shortly be described based on their overall performance to improve the speed response.

LTID-SMO-Sign:

- This method showed an overall good result in the estimation of the actual load torque resulting in a peak-to-peak of 33 [RPM] with a corresponding recovery time at $T_{RT} = 111\,[\text{ms}]$. The main drawback of this method is the chattering, which is heavily present in both the speed response and estimated load torque.

LTID-SMO-Sat:

- This method is considered the better option for LTID-SMO method by having the lowest recovery time at $T_{RT} = 103\,[\text{ms}]$ and the lowest peak-to-peak value of 24 [RPM]. This also corresponds to having the best estimation accuracy, as it obtained a fast transient response during the load step.

LTID-SMO-PS-K_{PS}:

- This method showed similar results as LTID-SMO-Sat with slightly slower recovery time at $T_{RT} = 106\,[\text{ms}]$ and a peak-to-peak value of 32 [RPM]. However, this method showed minor improvement in reducing the chattering compared to LTID-SMO-Sat.

LTID-SMO-PS-PI:

- This method showed good results in reducing the chattering in steady-state. However, it could not perform well under the transient response, resulting in a lower estimation accuracy than the above LTID-SMO methods. Its overall performance for the recovery time and peak-to-peak value was $T_{RT} = 125\,[\text{ms}]$ and 41 [RPM] respectively.

7.2.2 Test at 1800 [RPM] for 5 [Nm] load step

The summary of the speed and load torque RMSE and maximum errors obtained though Chapter 6 are presented in Table 7.3.

	Speed Error [RPM]		Torque Error [Nm]	
	RMSE	Max	RMSE	Max
Without LTID-SMO	7	60	-	-
LTID-SMO-Sign	1.85	32	0.43	4.3
LTID-SMO-Sat	1.6	28	0.35	4.6
LTID-SMO-PS-K_{PS}	2	32	0.37	4.8
LTID-SMO-PS-PI	2.4	43	0.4	6

Table 7.3. Summary of the errors at 1800 [RPM].

From Figure 7.10 the speed response is shown for each of the LTID-SMO methods. To analyze and compare the LTID-SMO methods, the *peak-to-peak* value and recovery time will be analyzed separately, where Table 7.3 will be used to understand each speed response further. In Figure 7.11 and 7.14 shows peak-to-peak and RMSE. These values are based on the data seen in the respective graphs.

Peak-to-peak: The Figure 7.10 shows that the LTID-SMO-Sat shows the best performance regarding the peak-to-peak value just as what was seen at lower speed. Again it is expected as the LTID-SMO-Sat also shows the lowest RMSE and max errors from Table 7.3. Similar to lower speed, the LTID-SMO-PS-PI has the highest peak-to-peak value during the transient part of the speed response, which corresponds to the RMSE and max errors in the summary table. If analyzing the peak-to-peak value for LTID-SMO-PS-K_{PS} and-Sign, it is seen that both methods have the same peak-to-peak value at 32 [RPM].

Recovery time: The recovery time for LTID-SMO-PS-K_{PS} and -Sign are showing the best performance with a recovery time of $T_{RT} = 76\,[\text{ms}]$. This can be explained by having the same peak-to-peak values and similar oscillating tendencies during the steady-state response. The LTID-SMO-PS-PI has the highest recovery time at $T_{TR} = 97\,[\text{ms}]$, on top of having the highest peak-to-peak value of the SMOs.

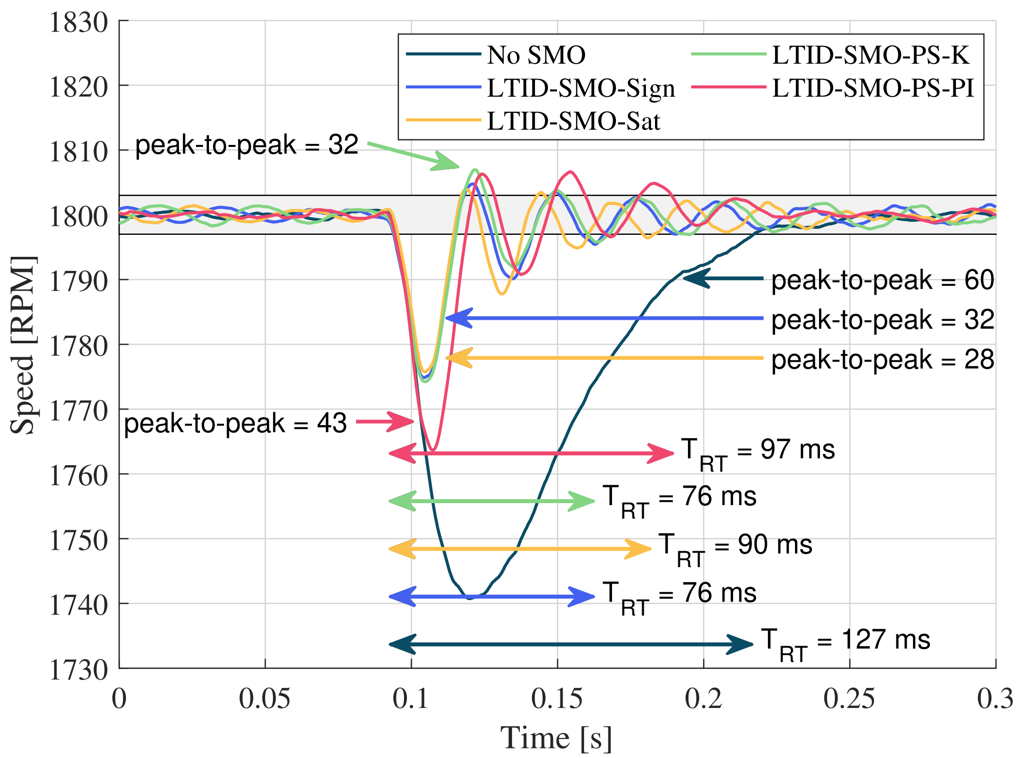

Figure 7.10. Experimental comparison of the LTID-SMO methods for the speed response at 1800 [RPM].

Speed during steady state: If analyzing the steady-state response in Figure 7.11, it can be seen that the LTID-SMO-PS-K_{PS} has the highest RPM error and RMSE during the steady-state part, with the highest speed RMSE of 1.25 [RPM] when all other methods are far below 1. The peak to peak error is also highest compared to the other methods when looking at the steady state. Suppose, comparing the steady-state response for LTID-SMO-PS-K_{PS} at 600 [RPM], the steady-state response is significantly increased. This indicates some oscillations which seems to be speed dependent. An additional frequency analysis is made to describe the sudden increase in amplitude when running the drive system at 1800 [RPM]. The frequency analysis is presented with an FFT analysis described in Section 7.3.

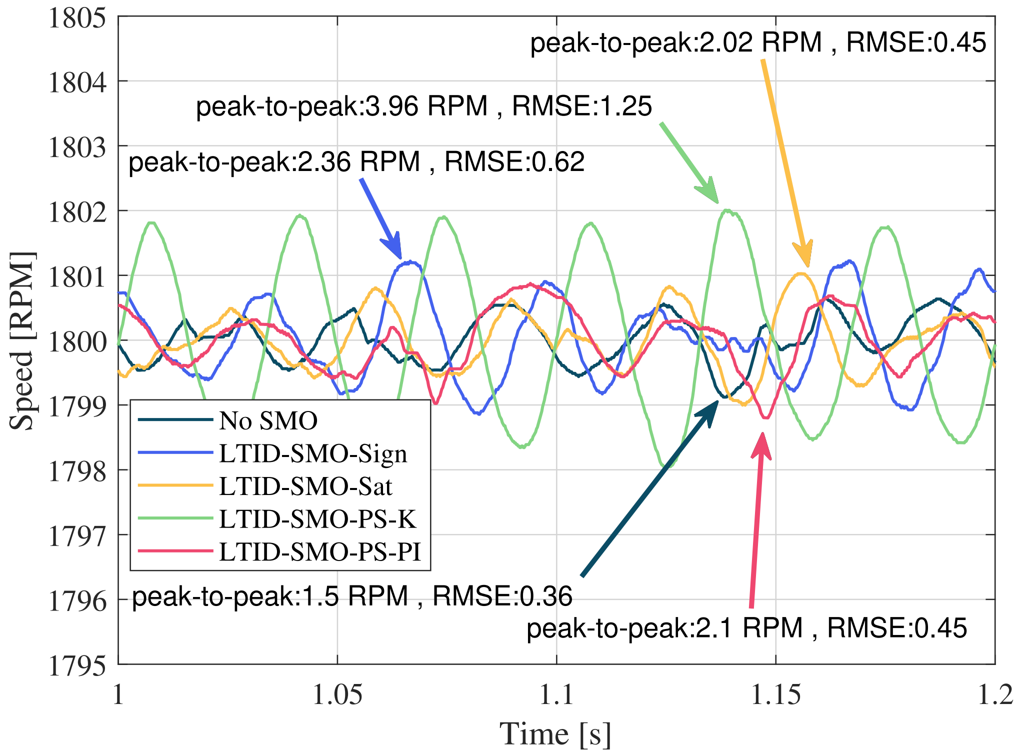

Figure 7.11. Experimental comparison of the LTID-SMO methods for the speed response at 1800 [RPM] in steady-state.

From Figure 7.12 the estimated load torque is presented for each LTID-SMO method, where the chattering and transient performance for each LTID-SMO method will be analyzed and compared. Figure 7.13 is the sliding variable and Figure 7.14 is the torque estimation in steady state.

Transient response: From the transient response of the estimated load torque, similar results are seen, as for the test at 600 [RPM], where the LTID-SMO-Sat is showing the best performance, as it leads the other methods. On the other hand, again the LTID-SMO-PS-PI has the slowest dynamical response. The behavior of the sliding variable is as seen earlier for 600 [RPM]. No further explanation is made, as the explanation from the test at 600 [RPM] may also be valid for the test at 1800 [RPM].

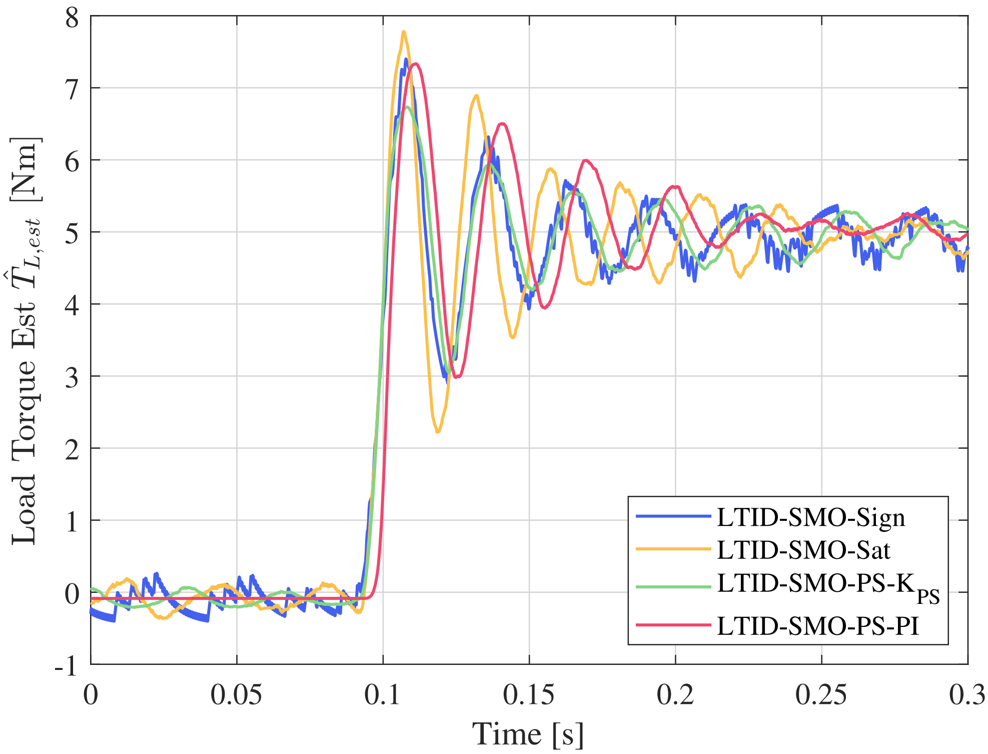

Figure 7.12. Experimental comparison of the LTID-SMO methods for the estimated load torque at 1800 [RPM].

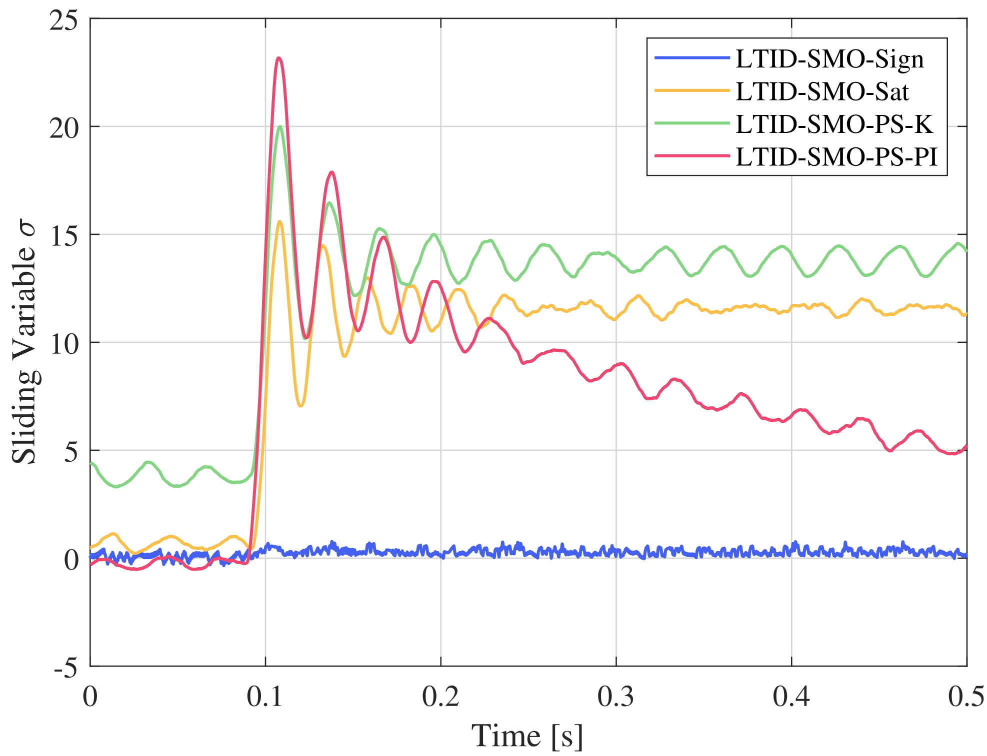

Figure 7.13. Experimental comparison of the LTID-SMO methods for the sliding variable at 1800 [RPM].

Chattering: By inspecting the chattering in the estimated load torque in Figure 7.14, it is seen that chattering tendencies are similar to the test at 600 [RPM]. However, from the steady-state response, the noticeable difference between the two tests is again the increased chattering for LTID-SMO-PS-K_{PS}. Here the torque RMSE is now at 0.23, which is larger than what was seen for sign at 600 [RPM] and 1800 [RPM]. Its chatter level is lower than for sign, but seemingly more susceptible to the mechanical oscillation. The LTID-SMO-PS-PI is again almost zero in both peak to peak and RMSE error. The LTID-Sat is still proving to be good by only being slightly worse at higer speed compared to its performance at lower speed, and now clearly beating the LTID-SMO-PS-K_{PS} in steady state load torque estimation. The increased amplitude for the observers of the oscillation is being fed into the speed response, which is partly why the larger oscillations is seen in the steady-state speed response in Figure 7.11.

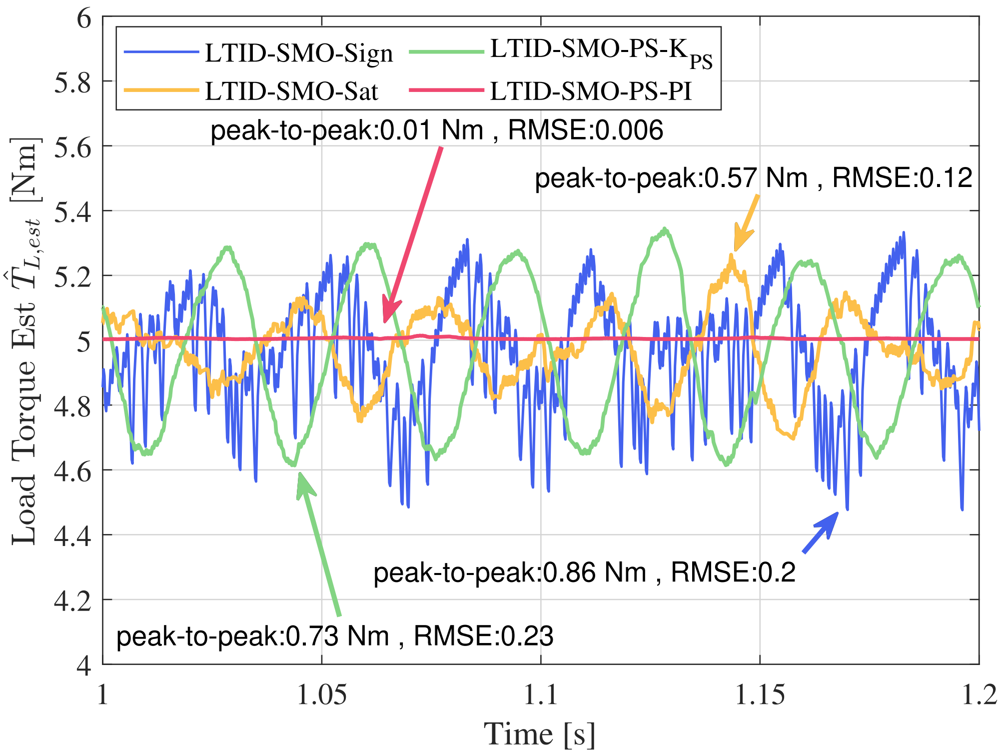

Figure 7.14. Experimental comparison of the LTID-SMO methods for the estimated load torque in steady-state at 1800 [RPM].

Summary for the test at 1800 [RPM]

To summarize the above analysis for the test at 1800 [RPM], each LTID-SMO method will shortly be described based on their overall performance to improve the speed response.

LTID-SMO-Sign:

- This method showed overall good results in the estimation of the actual load torque resulting in a peak-to-peak of 32 [RPM], with a corresponding recovery time at $T_{RT} = 76$ [ms]. Thereby a slight reduction in both the recovery time and peak-to-peak value compared to the speed response at 600 [RPM].

LTID-SMO-Sat:

- For the test at 1800 [RPM], this method remains the superior LTID-SMO method by having the lowest peak-to-peak value of 28 [RPM] and a recovery time at $T_{RT} = 90\,$[ms]. In addition, the recovery time showed minor improvements for this test, compared to the test at 600 [RPM]. However, the peak-to-peak value has increased slightly.

LTID-SMO-PS-K_{PS}:

- This method showed similar results as LTID-SMO-Sign with a peak-to-peak value of 32 [RPM] and a recovery time of $T_{RT} = 76\,$[ms]. Thereby having the same behavior as LTID-SMO-Sign during the transient response. However, this method showed higher oscillation than the other LTID-SMO methods in steady-state.

LTID-SMO-PS-PI:

- This method showed good results in reducing the chattering in steady-state. However, it could not perform well under the transient response, resulting in a lower estimation accuracy than the above LTID-SMO methods. Its overall performance for the recovery time and peak-to-peak value was $T_{RT} = 97\,$[ms] and 43 [RPM] respectively.

7.3 FFT Analysis of Speed at 1800 [RPM] Under 5 [Nm] Load

Specific oscillations with a constant time period indicate something in the motor are causing these. The appearance of these oscillations will be discussed in the following analysis.

Figure 7.15 shows the FFT result of the speed measurement, running at 1800 [RPM] under a constant load torque of 5 [Nm]. The FFT is made with the data from Figure 7.11. From the FFT analysis, it is clear that a sine wave with a frequency of 30 [Hz] is present through all measurements. The frequency of 30 [Hz] is also present during the observations without any LTID-SMO (the top graph). Therefore, it is not the LTID-SMOs that causes this frequency but likely something mechanical from the structure of the motor.

In Appendix C, an FFT is shown with no load torque applied. This shows that the mechanical frequency is also present without the load torque. Entailing that the load machine probably does not cause this frequency either. Besides this, 30 [Hz] corresponds with 1800 [RPM], as $30 \cdot 60 = 1800$[RPM]. Further suggesting that this frequency is due to a mechanical issue. In the Appendix C, it is also shown for the motor running at 600 [RPM], where a similar result is shown. However, with a significantly reduced mechanical frequency amplitude compared to 1800 [RPM]. It indicates that higher RPM amplifies this mechanical frequency more. However, as the issue lies in the mechanical parts that make up the motor, no compensation can be made to reduce the mechanical frequency.

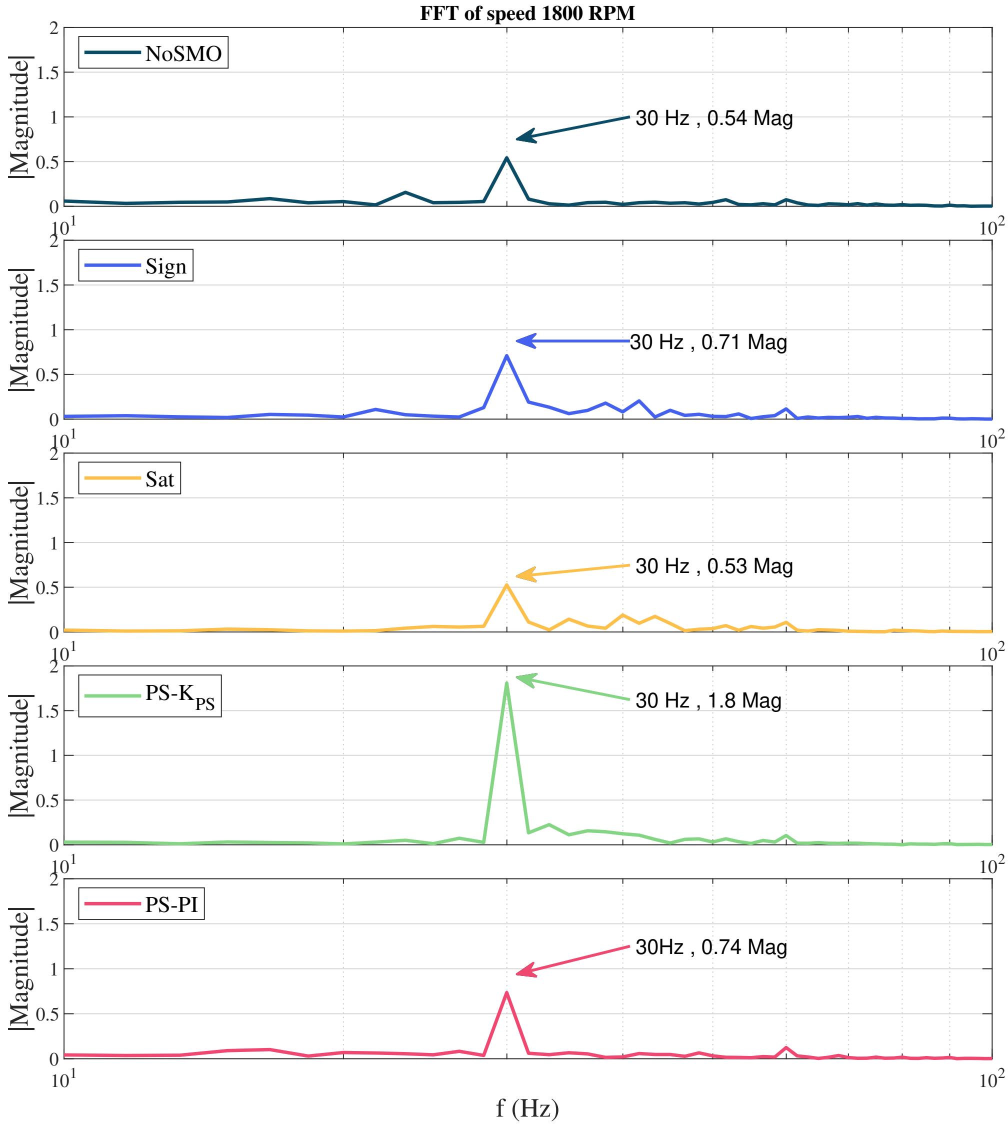

Figure 7.15. FFT of speed at 1800 [RPM] at constant 5 [Nm] load torque

Conclusion 8

Four different LTID-SMO to identify the Load torque have been successfully made and tested against each other, both through simulation and experimental tests. The conventional LTID-SMO-Sign using a sign function worked as expected, had a reasonably good estimation, recovery time and decreased the speed error, however with high chatter due to the discontinues Sign function. It did though improve the over all response both at lower and higher speed at different torque levels compared to system running without LTID-SMO.

The second method is the improved LTID-SMO-Sat, where the switching function was changed to the continues saturation function combined with an extra feedback term with a LPF. This method showed much improved load torque estimation accuracy, faster recovery, lower speed error and low chatter in the estimation compared to conventional LTID-SMO-Sign method and the system running without an LTID-SMO. It had quick transient response, and good steady state performance as was intended. It worked well both at low and high speed with different load torque levels.

Two methods was proposed methods based on using a Power Sigmoid as the switching function. The intention for the first proposed method LTID-SMO-PS-K_{PS} was for low chatter during no load, which it succeeded with. Its load torque estimation accuracy was similar to the LTID-SMO-Sat using Saturation. It successfully reduced the recovery time, reduced speed error compared to running without an LTID-SMO. Its chatter level was low, especially at lower speeds, however suffered slightly at higher speeds due to the mechanical frequency.

The second proposed method LTID-SMO-PS-PI used a PI controller to reduce the sliding variable during steady state, to reduce chatter in steady state performance. This method did reduce the chatter level substantially during the steady state compared to the other three methods. It is shown that its recovery time and speed error was reduced well compared to the system without an LTID-SMO. However, during the transient response, its estimation was not on par with the previous three methods, showing slower descent in load torque estimation, and a slower speed error rejection.

Bibliography

[1] Wenqi Lu, Zhenyi Zhang, Dong Wang, Kaiyuan Lu, Di Wu, Kehui Ji, and Liang Guo. A new load torque identification sliding mode observer for permanent magnet synchronous machine drive system. https://ieeexplore.ieee.org/document/8534417, 2017.

[2] Fran Hanejko. Permanent magnet vs. induction motor efficiency: Design materials. https://www.horizontechnology.biz/blog/induction-vs-permanent-magnet-motor-efficiency-auto-electrification, 2022.

[3] Vasilios C. Ilioudis and Nikolaos I. Margarisu. Sensorless speed and position estimation of pmsm using sliding mode observers in - reference frame. https://ieeexplore.ieee.org/document/4602190, 2016.

[4] Jinhua She, Lulu Wu, Chuan-Ke Zhang, Zhen-Tao Liu, and Yonghua Xiong. Identification of moment of inertia for pmsm using improved modelreference adaptive system. https://link.springer.com/article/10.1007/s12555-020-0549-8, 2022.

[5] Li Niu, Dianguo Xu, Ming Yang, Xianguo Gui, and Zijian Liu. On-line inertia identification algorithm for pi parameters optimization in speed loop. *IEEE Transactions on Power Electronics*, 30(2):849–859, 2015.

[6] Hui Wang, Yunkuan Wang, and Xinbo Wang. Speed and load torque estimation of spmsm based on kalman filter. In *2015 IEEE International Conference on Mechatronics and Automation (ICMA)*, pages 808–813, 2015.

[7] Song Chi, Zheng Zhang, and Longya Xu. Sliding-mode sensorless control of direct-drive pm synchronous motors for washing machine applications. *IEEE Transactions on Industry Applications*, 45(2):582–590, 2009.

[8] Hongryel Kim, Jubum Son, and Jangmyung Lee. A high-speed sliding-mode observer for the sensorless speed control of a pmsm. https://ieeexplore.ieee.org/stamp/stamp.jsp?tp=&arnumber=5661838, 2011.

[9] Fitzgerald and Kingsley. *Electric Machinery*. MCGraw-Hill Education, 2014.

[10] Kaiyuan Lu. Control of Electrical Drive Systems and Converters, Lecture 1. *Moodle.aau.dk*, 2021.

[11] Kaiyuan Lu. Modern Electrical Drives, Topic 7. *Moodle AAU*, 2020.

[12] MathWorks. System identification app. https://se.mathworks.com/help/ident/ug/working-with-the-system-identification-tool-gui.htmll.

[13] Hao Zhu, Xi Xiao, and Yongdong Li. Pi type dynamic decoupling control scheme for pmsm high speed operation. In *2010 Twenty-Fifth Annual IEEE Applied Power Electronics Conference and Exposition (APEC)*, pages 1736–1739, 2010.

[14] Charles L. Phillips. *Feedback Control Systems*. Pearson Education (Us), 2011.

[15] Muhammad Asad, Muhammad Ashraf, Sohail Iqbal, and Aamer Bhatti. Chattering and stability analysis of the sliding mode control using inverse hyperbolic function. https://link.springer.com/article/10.1007/s12555-016-0654-x, 2017.

[16] LibreTexts libraries. Power functions and polynomial functions. https://math.libretexts.org/Bookshelves/Precalculus/Precalculus_(OpenStax)/03%3A_Polynomial_and_Rational_Functions/3.03%3A_Power_Functions_and_Polynomial_Functions, 2022.

[17] Xiaoguang Zhang and Benshuai Hou. Novel reaching law-based sliding-mode load torque observer for pmsm. https://ieeexplore.ieee.org/abstract/document/7837245, 2016.

[18] Yuri Shtessel, Christopher Edwards, Leonid Fridman, and Arie Levant. *Sliding Mode Control and Observation*. Birkhäuser, 2013.

[19] Wenqi Lu, Bo Tang, Kehui Ji, Kaiyuan Lu, Dong Wang, and Zhijun Yu. A new load adaptive identification method based on an improved sliding mode observer for pmsm position servo system. *IEEE Transactions on Power Electronics*, 36(3):3211–3223, 2021.

[20] Sigurd Skogestad and Ian Postlethwaite. *Multivariable Feedback Control*. John Wiley Sons, Ltd, 2010.

[21] Jun Lu, Jianguo Yang, Yinchen Ma, and Ruirong Ren. Compensation for harmonic flux and current of permanent magnet synchronous motor by harmonic voltage. *2015 International Conference on Informatics, Electronics Vision (ICIEV)*, pages 1–5, 2015.

Relative Gain Array Analysis A

To analyze the coupling effect of the two states $[i_q \; i_d]^T$, a relative gain array (RGA) analysis is made, taking basis in [20]. The RGA analysis is a steady-state measure of the interaction between the input/output paring. The coupling effect is analyzed with Equation 3.10 and 3.11 and repeated here:

$$v_d(t) = R_s i_d + \frac{d}{dt}(L_d i_d + \lambda_{mpm}) - \omega_e L_q i_q \tag{A.1}$$

$$v_q(t) = R_s i_q + \frac{d}{dt} L_q i_q + \omega_e (L_d i_d + \lambda_{mpm}) \tag{A.2}$$

where $\frac{d}{dt}(\lambda_{mpm}) = 0$ as the pm flux is assumed to be constant. From Equation A.1 and A.2 the coupling items are shown in the back-EMF terms defined as:

$$e_d = -\omega_e L_q i_q \tag{A.3}$$

$$e_q = \omega_e (L_d i_d + \lambda_{mpm}) \tag{A.4}$$

By converting the above-voltage equations, A.1 and A.2, from the time domain to the Laplace domain the following can be obtained:

$$V_d(s) = (R_s + sL_d) i_d - \omega_e L_q i_q \tag{A.5}$$

$$V_q(s) = (R_s + sL_q) i_q + \omega_e L_d i_d + \omega_e \lambda_{mpm} \tag{A.6}$$

If representing the Laplace transformed voltage equations by state-space notification, the following transfer function matrix is obtained:

$$\begin{bmatrix} V_d \\ V_q' \end{bmatrix} = \begin{bmatrix} V_d \\ V_q - \omega_e \lambda_{mpm} \end{bmatrix} = \begin{bmatrix} R_s + sL_d & -\omega_e L_q \\ \omega_e L_d & R_s + sL_q \end{bmatrix} \cdot \begin{bmatrix} i_d \\ i_q \end{bmatrix} \tag{A.7}$$

If defining the transfer function matrix as in [20], Equation A.7 can be written in terms of static gains, if evaluated at $s = 0$, leaving that:

$$\begin{bmatrix} y_1 \\ y_2 \end{bmatrix} = \begin{bmatrix} h_{11} & h_{12} \\ h_{21} & h_{22} \end{bmatrix} \cdot \begin{bmatrix} u_1 \\ u_2 \end{bmatrix} \tag{A.8}$$

$$\textit{where} \quad h_{11} = R_s \quad , \quad h_{12} = -\omega_e L_q \quad , \quad h_{21} = \omega_e L_d \quad \textit{and} \quad h_{22} = R_s \tag{A.9}$$

The RGA of a non-singular square matrix (determinant is not zero) are defined as:

$$RGA = \begin{bmatrix} \lambda_{11} & \lambda_{12} \\ \lambda_{21} & \lambda_{22} \end{bmatrix} = \begin{bmatrix} \lambda_{11} & 1-\lambda_{11} \\ 1-\lambda_{11} & \lambda_{11} \end{bmatrix} \quad where \quad \lambda_{11} = \frac{1}{1-\frac{h_{12}h_{21}}{h_{11}h_{22}}} \tag{A.10}$$

The RGA consists only of the λ_{11} element, where a fully decoupled system would entail that $\lambda_{11} = 1$. This would further mean that y_1 only depends on u_1 and y_2 only depends on u_2. Furthermore, the RGA evaluates the coupling between the outputs and inputs in steady-state, leaving λ_{11} to be calculated as:

$$\lambda_{11} = \frac{1}{1-\frac{-\omega_e L_q \cdot \omega_e L_d}{R_s \cdot R_s}} = \frac{R_s^2}{R_s^2 + \omega_e^2 L_s^2} \tag{A.11}$$

where $L_s = L_d = L_q$ as the d and q axis inductance is equal for a SPMSM.

From Figure A.1 the input/output paring are shown with a sweep for ω_e. The system is fully decoupled at $\omega_e = 0$. As the speed increases, a stronger coupling is seen. Therefore, the back-EMF is decoupled to compensate for the coupling between the d and q axis voltage equations.

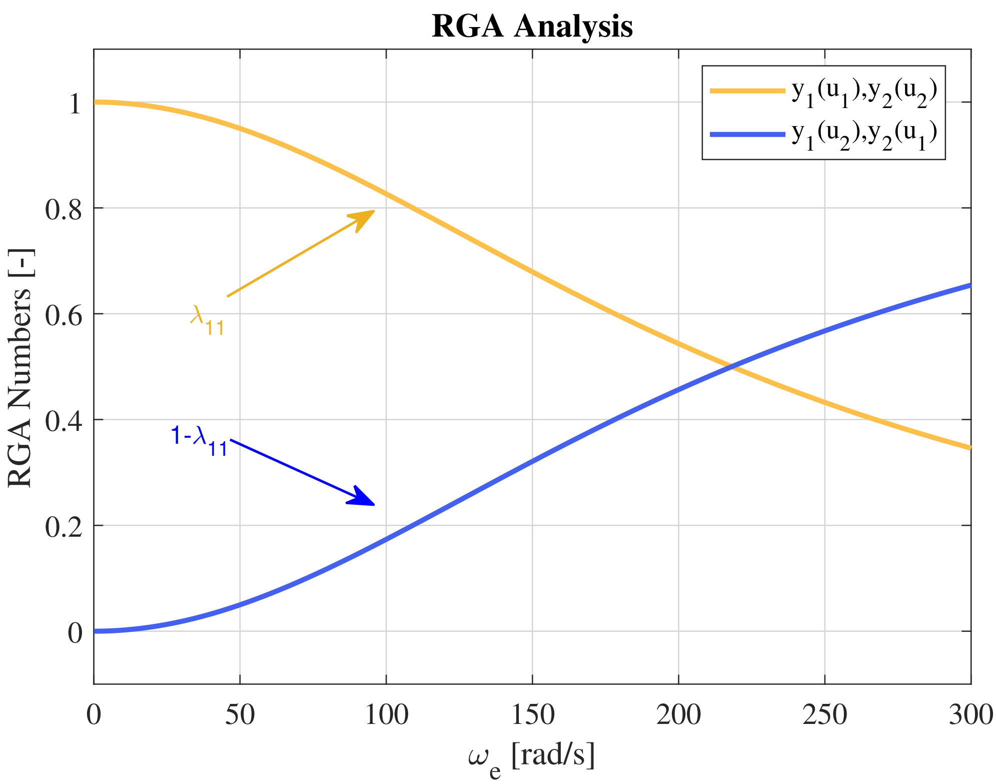

Figure A.1. RGA Analysis, where the input/output paring are shown for an increase in ω_e.

Power Sigmoid with PI - Stability Proof B

B.1 PI stability

The stability proof for LTID-SMO-PS-PI is made here:

$$\sigma = \frac{N_{pp}}{J}T_{L,max} - \frac{B}{J}\sigma - Z_s \quad where \quad Z_s = \frac{\sigma^{\alpha}}{|\sigma|^{\alpha} + \delta} \cdot \left(K_{P,smo} + \frac{K_{I,smo}}{s}\right) \tag{B.1}$$

$$V = \frac{1}{2}\sigma^2 \tag{B.2}$$

$$\dot{V} = \dot{\sigma}\sigma = \left[\frac{N_{pp}}{J}T_L - \frac{B}{J}\sigma - \frac{\sigma^{\alpha}\left(K_{P,smo} + \frac{K_{I,smo}}{s}\right)}{|\sigma|^{\alpha} + \delta}\right] \cdot \sigma \tag{B.3}$$

The observer is stable if $\dot{V} < 0$. From Equation B.3 it is seen that $-\frac{B}{J}\sigma^2$ is always negative. Therefor if

$$0 > \left[\frac{N_{pp}}{J}T_L - \frac{\sigma^{\alpha}\left(K_{P,smo} + \frac{K_{I,smo}}{s}\right)}{|\sigma|^{\alpha} + \delta}\right] \cdot \sigma \tag{B.4}$$

is fulfilled the observer is able to do sliding mode action.

$$\dot{V} = \begin{cases} \frac{N_{pp}T_L}{J} - \frac{\sigma^{\alpha}\left(K_{P,smo} + \frac{K_{I,smo}}{s}\right)}{|\sigma|^{\alpha}+\delta} & , \quad \sigma \geq 0 \\ \frac{N_{pp}T_L}{J} + \frac{\sigma^{\alpha}\left(K_{P,smo} + \frac{K_{I,smo}}{s}\right)}{|\sigma|^{\alpha}+\delta} & , \quad \sigma < 0 \end{cases} \tag{B.5}$$

Isolating for $K_{P,smo}$

$$K_{P,smo} = \frac{N_{pp}T_L}{J} + \frac{N_{pp}T_L\delta}{J\sigma^a} - \frac{K_{I,smo}}{s} \tag{B.6}$$

$$K_{P,smo} = \frac{N_{pp}T_L}{J} + \frac{N_{pp}T_L\delta}{J\sigma^a} - \int_0^t K_{I,smo}\,dt \tag{B.7}$$

If the variables are defined as $N_{pp} = 4; T_{L,max} = 5.8; J = 0.0125; \delta = 1500; \sigma = 20; a = 3; K_{I,smo} = 15000$. σ is chosen as where the sliding variable will increase to when a max load step is provided. It is however important to note that during the transient part, the load torque will reach as high as 8 [Nm]. Therefor to ensure stability in this scenario, $T_{L,transient} = 8$[Nm].

$$K_{P,smo} = \frac{N_{pp}T_{L,transient}}{J}\left(1 + \frac{\delta}{\sigma^a}\right) - K_{I,smo}t \tag{B.8}$$

$$K_{P,smo} = 3040 - 15000 \cdot t \tag{B.9}$$

where t is the time. At time $t = 0$ seconds, $K_{P,smo} = 3040$.
To check if $K_{P,smo}$ fulfills the criteria at t=0 it can be calculated that

$$\frac{N_{pp}T_{L,max}}{J} = 2560 \tag{B.10}$$

and

$$\frac{\sigma^\alpha\left(K_{P,smo} + \int_0^t K_{I,smo}\,dt\ \right)}{|\sigma|^\alpha + \delta} = \frac{20^3\left(3040 - 15000\,t + 15000\,t\right)}{|20|^3 + 1500} = 2560 \tag{B.11}$$

meaning the Lyapunov stability criteria in Equation B.5 is fulfilled.

FFT Analysis C

Figure C.1 is the FFT analysis based on data from Figure 7.6. The Top graph is the system when running without an LTID-SMO at 600 RPM under 5Nm of load. At first, it can be noticed that a frequency of 10Hz is appearing. Likely this is due some mechanical issue, happening for every physical rotation as this corresponds with 600 RPM. Besides this, a higher frequency of 40 Hz is also noticed. This may come from the electrical part, as there is 4 pole pairs and the electrical frequency of 600 RPM corresponds to 40 Hz. For the LTID-SMO using Sign and Saturation functions the 40 Hz frequency has increased where as the 10 Hz has been reduced. The reason for the reduction at 10 Hz, could be due to the load torque estimation. It is clear that the mechanical frequency seen is present even during no added load torque and therefor not due to the load torque production from the load machine. This claim can be found in next Figure C.2. Therefor, as the LTID-SMO for Sign and Saturation gets the measured speed as an input, it sees the change in speed as a load torque. It therefor estimates a small load torque which is fed back to the FOC to counteract the ripples. The reason for increased 40 Hz amplitude has not definitively been found, but likely also stems from the estimation of load torque due to the current i_q and measured speed being used in the calculation. Using the LTID-SMO-PS-K_{PS} the 10 Hz frequency has also been mitigated well, and the 40 Hz frequency has doubled in amplitude. However a sub harmonic with almost same magnitude is also seen at 35 Hz. The bottom graph is LTID-SMO-PS-PI is having a seeing a small reduction of the 10 Hz harmonic, however an even 2 nd harmonic at 20 Hz is also present. This could be due to nonlinear inverter characteristics [21].

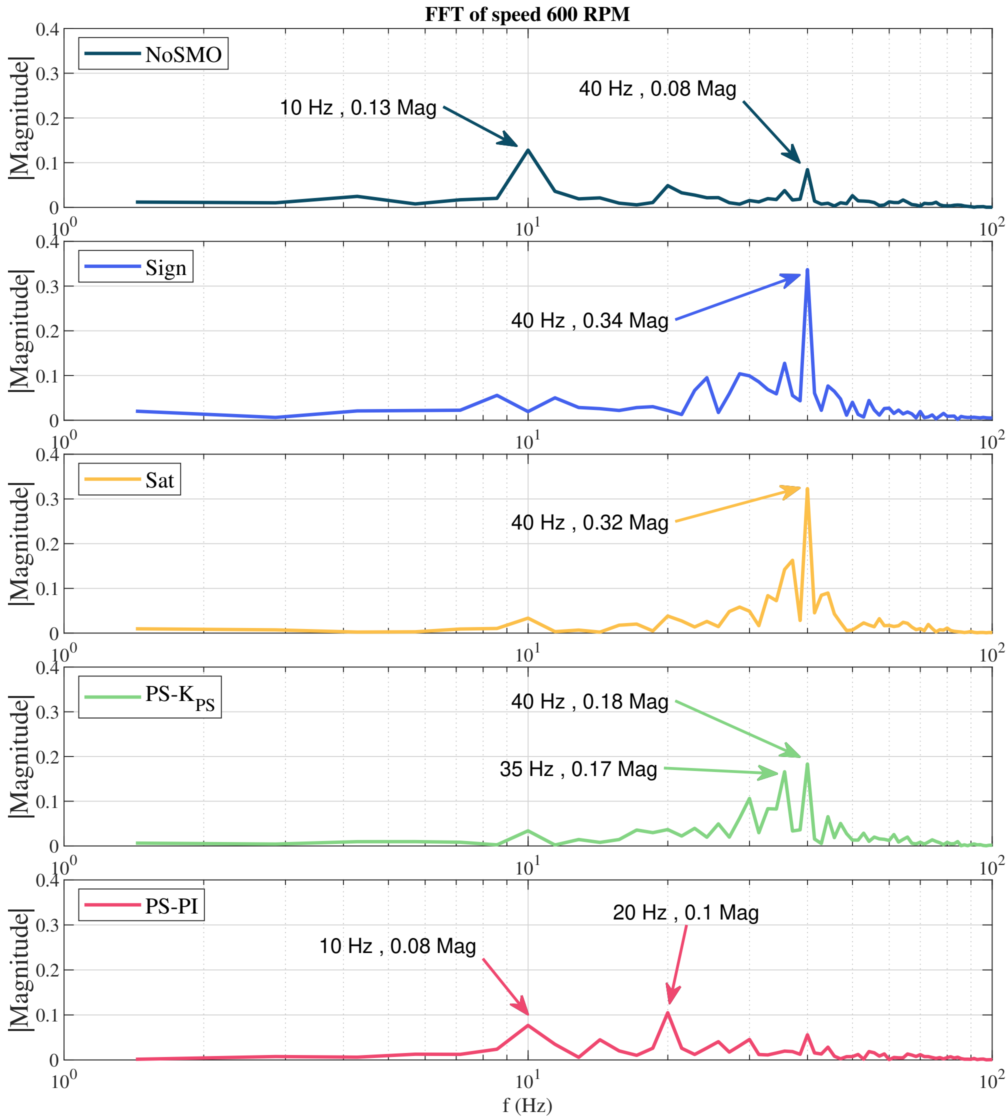

Figure C.1. FFT for 5 Nm running at 600 RPM

Figure C.2 shows the FFT during no load. It can be seen from this that the mechanical frequency is still present when no load is added from the load machine.

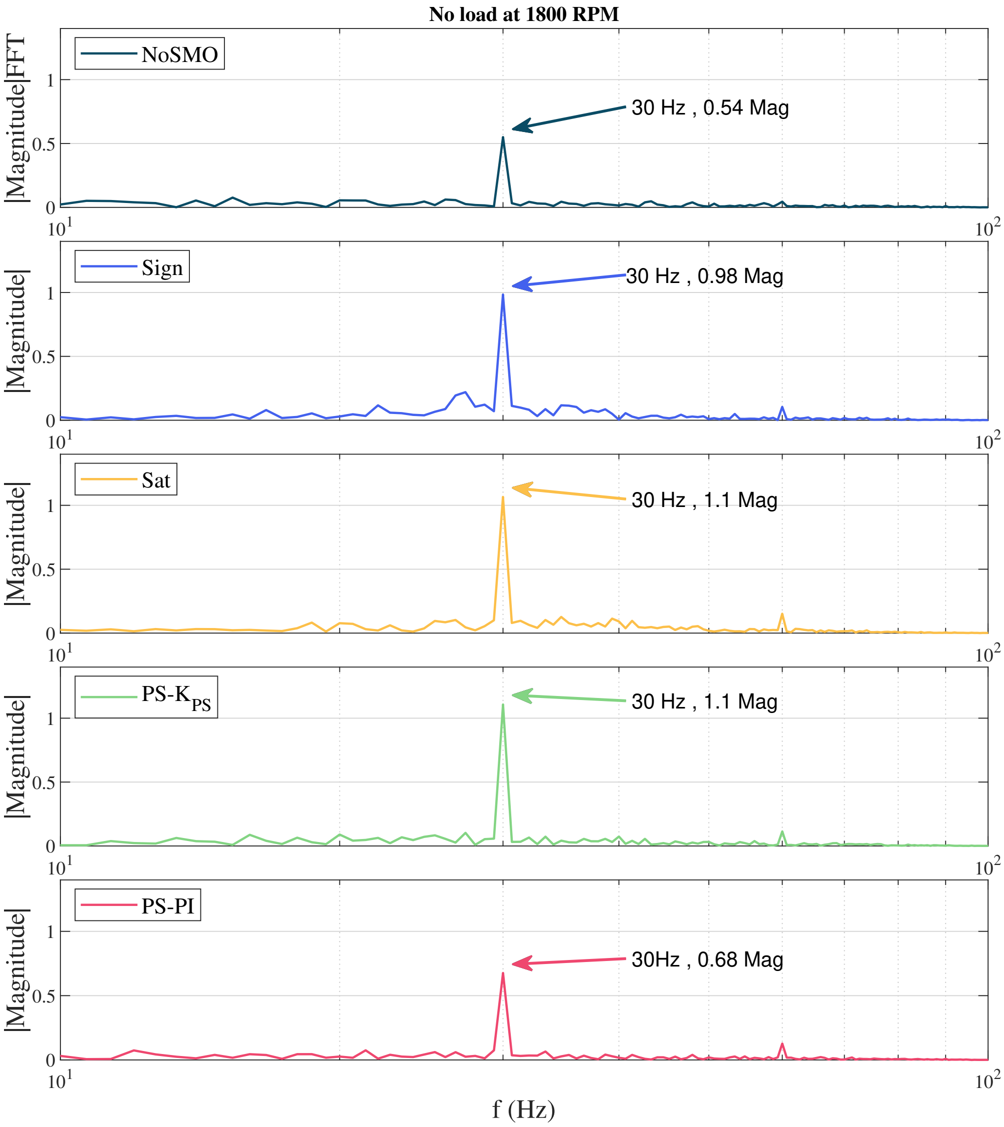

Figure C.2. FFt at speed 1800 RPM with no load on.